Apprentissage statistique de modèles réduits non-linéaires par approche expérimentale et design de contrôleurs robustes: le cas de la cavité ouverte

Claudio Ottonelli

▶ **To cite this version:**

Claudio Ottonelli. Apprentissage statistique de modèles réduits non-linéaires par approche expérimentale et design de contrôleurs robustes: le cas de la cavité ouverte. Fluid mechanics [physics.class-ph]. Ecole Polytechnique X, 2014. English. NNT : . pastel-01065782

HAL Id: pastel-01065782
https://pastel.hal.science/pastel-01065782

Submitted on 18 Sep 2014

HAL is a multi-disciplinary open access archive for the deposit and dissemination of scientific research documents, whether they are published or not. The documents may come from teaching and research institutions in France or abroad, or from public or private research centers.

L'archive ouverte pluridisciplinaire **HAL**, est destinée au dépôt et à la diffusion de documents scientifiques de niveau recherche, publiés ou non, émanant des établissements d'enseignement et de recherche français ou étrangers, des laboratoires publics ou privés.

École Polytechnique

Thèse présentée en vue de l'obtention du titre de

Docteur de École Polytechnique

par

Claudio Ottonelli

Apprentissage statistique de modèles réduits non-linéaires par approche expérimentale et design de contrôleurs robustes: le cas de la cavité ouverte

---

Soutenue en 20 juin devant un jury composé de

F. Lusseyran	Directeur de Recherche au CNRS, LIMSI Saclay	*Rapporteur*
D. Fabre	Maître de Conférence, IMFT Toulouse	*Rapporteur*
L. Cordier	Chargé de Recherche au CNRS, PPRIME Poitiers	*Examinateur*
L. Pastur	Maître de Conférence Université Paris Sud 11	*Examinateur*
P. Schmid	Professeur, LadHyX Palaiseau	*Directeur de Thèse*
D. Sipp	Maître de recherche, ONERA, Meudon	*Directeur de Thèse*

ONERA

THE FRENCH AEROSPACE LAB

Résumé: Cette thèse est consacrée à la conception d'un contrôle en boucle fermée d'un écoulement de cavité subsonique. L'objectif est de réaliser un contrôleur qui dépend seulement de grandeurs observables expérimentalement et qui gère des situations où les écoulements sont excités par des perturbations aléatoires extérieures. Pour faire face à ces deux aspects essentiels, deux stratégies ont été définies: l'identification d'un modèle non-linéaire reproduisant la dynamique de l'écoulement à partir seulement d'informations mesurables et la conception d'un compensateur linéaire robuste, basée sur la théorie du contrôle $\mathcal{H}_\infty$, qui incorpore des propriété de robustesse dans la définition de la fonction objectif.

La première partie de la thèse est consacrée à l'identification d'un modèle non-linéaire grâce à des données obtenues à partir d'une expérience menée dans la soufflerie subsonique ($M = 0.1$) S19 sur le site Chalais-Meudon de l'ONERA. Afin de décrire la dynamique de cet écoulement, et en particulier son contenu fréquentiel, l'écoulement sans contrôle a été caractérisé par des mesures par fil chaud et de pression instationnaire et par des clichés de vélocimétrie par images des particules (PIV) résolue en temps. Un filtrage temporel a été appliqué avec succès aux clichés PIV afin d'extraire la dynamique basse fréquence de l'écoulement. Cette étape est indispensable pour pouvoir gérer des écoulements turbulents caractérisés par un spectre fréquentiel très étendu. Les modes POD obtenus ont été utilisés comme base de projection pour le champ de vitesse et les trajectoires associées ont été interpolées (apprentissage statistique) sur une structure de modèle non-linéaire autorégressif exogène (NLARX). Il s'avère que les modèles obtenus ne sont pas robustes, dans le sens où ils ne parviennent pas à reproduire la dynamique d'un ensemble de données de validation, une fois adaptés à un ensemble de données d'apprentissage. Il a été démontré que cet échec est dû aux fortes non-linéarités observées dans l'écoulement de cavité, qui rendent impraticables les méthodes d'identification.

La deuxième partie de la thèse est consacrée à la conception d'un contrôleur robuste à partir de simulations numériques d'un écoulement de cavité carrée, incompressible et en régime transitionnel, pour différents nombres de Reynolds. Diverses méthodes de synthèse de contrôleur ont été testées et évaluées en utilisant plusieurs mesures de robustesse. On a constaté que la technique traditionnelle de contrôle linéaire quadratique gaussien (LQG) présente une faible robustesse aux perturbations extérieures, tandis que d'autres, comme la technique LTR (Loop Transfer Recovery) et les contrôleurs basés sur les perturbations "les pires" (worst-case), améliorent la robustesse, mais pas suffisamment pour faire face à la forte non-linéarité de l'écoulement. Dans ce but, on met en place un contrôleur qui optimise les propriétés de robustesse par rapport à des incertitudes de type "entrée-multiplicative" et de type "entrée vers sortie". Celui-ci présente des marges de robustesse fortement augmentées par rapport à l'introduction de perturbations de la partie stable de la dynamique entré-sortie, même si le prix à payer en terme de performance est significatif. Une stratégie pour prendre en compte également des perturbations de la partie instable de la dynamique entrée-sortie, comme celles obtenues par un changement du nombre de Reynolds, a été présentée.

Mots clés: cavité, contrôle d'écoulement, boucle fermée, réduction de modèle, modes POD, projection Galerkin, identification de système, robustesse, incertitudes non structurées.

Summary: This thesis deals with the design of a closed-loop controller of a subsonic cavity flow. The objective is to build a controller that only relies on observable dynamics and that handles situations where the flow field is excited by unknown external random disturbances. For this, two strategies have been defined: the identification of a non-linear model representing flow dynamics from only measurable information and the design of a robust linear compensator, based on the $\mathcal{H}_\infty$ control theory, that incorporates robustness properties in the objective function definition.

The first part has been devoted to the identification of a non-linear model with data obtained from an experiment conducted at the ONERA S19 subsonic ($M = 0.1$) wind tunnel on the Chalais-Meudon site. In order to provide a full description of the fluid motion, in particular its frequency content, the natural (without control) flow has been characterized by hot-wire and unsteady pressure measurements and time-resolved Particle Image Velocimetry (PIV) snapshots. Time-filtering has been successfully applied to the PIV snapshots in order to focus on the large-scale low-frequency dynamics of the flow. This step has been shown critical to deal with turbulent flows characterized by high-frequency noise. The obtained POD modes have been used as a projection basis of the velocity field and the associated trajectories fitted to a Non-Linear Auto-Regressive eXogeneous (NLARX) model structure by an identification process. It turns out that the obtained models are not robust, in the sense that they do not manage to reproduce the dynamics of a validation data-set once fitted to a given learning data-set. It has been shown that this failure is due to the strong non-linearities observed in the cavity flow and that render identification methods impracticable.

The second part has been devoted to the design of a robust controller from numerical simulations of an incompressible square cavity flow at different Reynolds numbers in transitional regime. Various control design methods have been tested and assessed with respect to several robustness measures. It was found that the traditional Linear Quadratic Gaussian (LQG) controller exhibits poor robustness to external perturbations and that loop-transfer recovery (LTR) techniques and "worst-case" controllers improve robustness but not sufficiently to cope with the strong non-linearities in the flow. To this aim, a compensator design that optimizes the robustness properties with respect to unstructured input-multiplicative and input-to-output uncertainties is presented. The latter shows an important increase in robustness with respect to the introduction of perturbations of the stable part of the input-output relation even though a cost is payed in terms of performances. A strategy to deal also with perturbations of the unstable part of the dynamics, as obtained for example by change in Reynolds numbers, has been introduced.

Key words: cavity, flow-control, feedback, model reduction, POD modes, Galerkin projection, system identification, robustness, unstructured uncertainties.

Contents

Chapter 1

Introduction

Active flow control played in the very last decades a key role in the suppression of flow-field unsteadiness that are the main cause of noise, structural vibrations, drag increase and a number of issues in a large range of industrial applications. The interest in this area led to a development of technological devices, actuators and sensors, and control methodologies focused to manipulate the greatest range of flows as reviewed by Cattafesta and Sheplak (2011).

Among different types of control strategies — active, passive, open-loop, closed-loop, etc — active closed-loop control in fluid flows has received a lot of attention in recent years, in particular from the aerospace industry. The advantage of this kind of control is the small amount of energy input, compared to open-loop control, with the possibility to strongly alter the flow dynamics.

However, closed-loop control implies different approaches among control theorists and experimentalists, since the first often ignore the practical limitations imposed by the the existing technology and, on the other hand, the latter often do not appreciate dynamic requirements imposed by feedback control.

The study and analysis presented in this thesis are part of the closed-loop control of unsteady flows. In particular, they focus on the establishment of theoretical control methods applicable under experimental conditions.

1.1 Subsonic cavity flow

Flows over open cavities have been deeply studied by control theorists, fluid dynamicists and aeroacousticians, because of the variety of characteristics of such flows. The need to model different scales of aero-acoustic disturbances, to control competing modes in a large range of different conditions represent a challenge not always accomplished. For these and a number of other reasons, the flow over an open cavity is considered as a canonical problem in flow control.

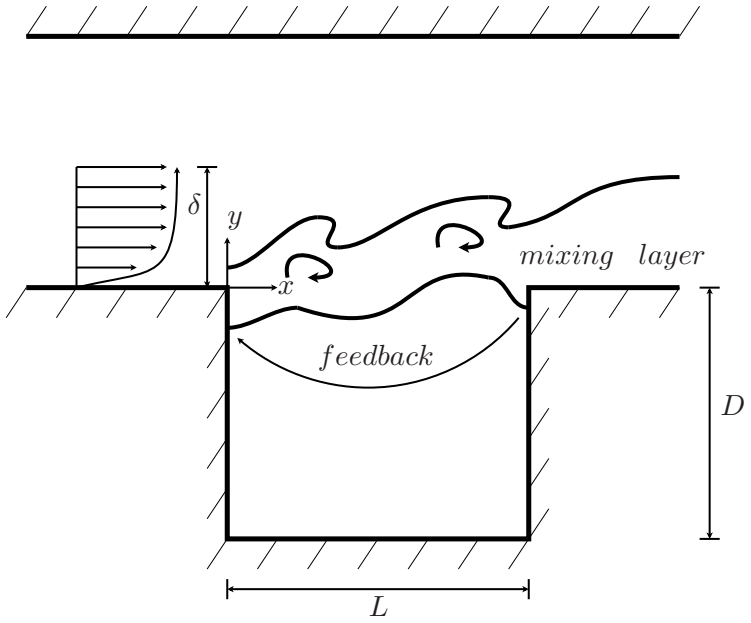

Figure 1.1: Schematic description of the cavity resonance.

The dynamics of separated flows are of fundamental interest in a number of realistic configurations. Kelvin-Helmholtz instabilities are commonly present in this type of flows causing an unsteady behavior in the shear-layer of the separation bubble. It is then of a great interest to suppress or weaken its unsteadiness. The open-cavity flow is a prototypical example of sustained instability. This type of flow exhibits a recirculating component (confined geometrically to the cavity) as well as a strong shear layer that forms at the top of the cavity and, for sufficiently high Reynolds numbers, becomes unstable and settles into a characteristic periodic motion (Sipp and Lebedev, 2007).

The control framework depends on the nature of the flow to be controlled. Globally unstable flows are more easily controlled, because of the limited number of structures at well-defined frequencies. The techniques applied in these situations have greatly relied on a mathematical framework established in control theory as described in standard references (Burl, 1998; Zhou et al., 1996), but additional complications had to be overcome when adapting them to fluid flows.

Cavity flows are characterized by a self-induced beating at a particular frequency. This behavior is typical for oscillating flows (Huerre and Rossi, 1998) and it consists in an exponential amplification of a given perturbation of the flow field followed by its saturation due to non-linear effects. The flow-induced cavity resonance mechanism is schematized in Fig. 1.1. A boundary layer of thickness δ separates at the upstream corner of a cavity of length L and depth D. The mixing layer develops over the cavity and eventually reattaches near the downstream edge. The downstream wall acts as an acoustic source, and the generated waves travel upstream. The acoustic waves force the shear layer at the

upstream edge as a feedback process producing resonant frequencies.

The mechanism has been described by Rossiter (1964) and is influenced by geometric parameters (L and D) and flow conditions (M and Re). Each flow is then characterized by specific cavity tones and the following harmonics. For this reason, cavity flows have been the subject of a huge quantity of studies since the late '50s. An exhaustive review of simulations, modeling and active control of flow/acoustic resonance in flows over open cavities can be found in Colonius (2001).

1.2 Closed-loop control

Flow control is necessary in a number of engineering applications and consists in the alteration of the original state towards a desired condition. Two strategies can be distinguished, *passive control* and *active control*. In this study we focus on the latter and, in particular, to closed-loop active control. However, an overview of flow control is given.

In aeronautic industry, passive control has played, and still plays, an important role, since it does not require any energy input. It consists in the alteration of the flow through geometric modifications or by placing artifacts in specific regions. Relevant examples of these devices and solutions are: vortex generators used to enhance turbulence in boundary layers (Godard and Stanislas, 2006) and therefore to delay separation (for drag reduction purposes) (Aider et al., 2010; Pujals et al., 2010), surface riblets used to reduce skin friction in channel flows (Walsh, 1983; Baron et al., 1993; El-Samni et al., 2007) and cylinders or rods placed near the leading edge of a cavity to suppress resonances (McGrath and Shaw, 1996; Illy et al., 2008; Yamouni et al., 2013).

Although good results have been shown by passive control techniques in particular conditions, a lack of adaptability and robustness to changes in flow conditions has been also remarked and represents a huge limitation. Technology evolution allowed the development of active control strategies capable to deal with these situations in a wider range of applications.

The peculiarity of active control is the need of energy and a more complex system in order to adapt to flow changes. The amount of energy requested has to be compared with a global advantage in terms of energy saving or power gain, as explained by Kasagi et al. (2009). In practical aeronautical applications, an example can be represented by control techniques designed for skin-friction drag reduction, that has the consequence of a diminished fuel consumption. Active control can be performed with two different strategies: closed-loop control, where the control law is defined from feedback given by real-time measurements, and open-loop control, that relies on no feedback.

Open-loop control lived its golden era in particular during the 90s and the first years of the 2000s. Many applications have been the objective of this technique, as the suppression

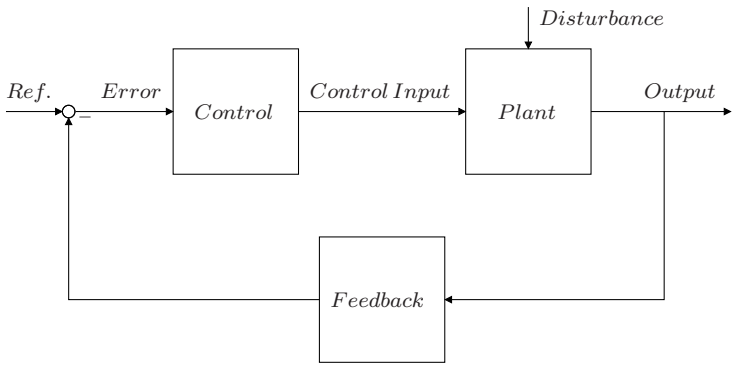

Figure 1.2: Closed-loop control scheme. Each block represents a transfer function, while the arrows are related to time-domain quantities.

of cavity resonances or the reduction of viscous drag. To these aims, a wide set of actuation devices has been employed: oscillating electromechanical and piezoelectric flaps and plates, fluidic oscillating jets, voice-coil drivers, steady and pulsed blowing and resonance tubes, as reviewed in Cattafesta et al. (2003). Successful results in active open-loop flow control have been obtained by Zhuang et al. (2006) and Ukeiley et al. (2007) on cavity tones suppression and by Quadrio and Ricco (2004) on drag reduction from span-wise wall oscillations.

Closed-loop control became more important with the development of real-time technologies. The key feature of the closed-loop control is that some flow quantities, measured or estimated, are fed back to an algorithm that modifies the optimal control signal that minimizes a prescribed objective (Di Stefano et al., 1990). A simple representation of the feedback system is schematized in Fig. 1.2, where sensors and actuators are included in the plant, without specification of the frequency contribution.

A huge importance in feedback control is then assumed by actuators and sensors. Their performances and efficacy are evaluated in terms of static and dynamic responses, energy requirement, size, weight, bandwidth, gain (for actuators) and sensitivity (for sensors). These characteristics have the same importance than the fluid interaction. Typically, in feedback flow control, actuation devices are: piezoelectric moving flaps, zero-net mass flows and plasma actuators. Sensors used more frequently in this type of applications are generally unsteady pressure transducers, hot wires and hot films and thermocouples. These devices present good features in terms of frequency bandwidth and time response. The main characteristics and design issues for actuators and sensors are summarized in a number of reviews as Cattafesta and Sheplak (2011).

The information given by sensors can be used with two different approaches: quasi-static and dynamic controllers. The first closed-loop strategies were modifications of open-loop control techniques. For instance, feedback has been used in several works to slowly tune the frequency of an open-loop forcing to improve the suppression of unsteady

pressure oscillations or the reduction of velocity fluctuations. These kind of controllers are called by Cattafesta et al. (2003) "quasi-static" since the feedback dynamic is much slower than flow dynamics. Notable examples in cavity flows are represented by Shaw and Northcraft (1999), that modulated a sinusoidal forcing function to reduce the sound pressure level of cavity resonance, and by Debiasi and Samimy (2004), that used an adaptive algorithm to adjust the frequency forcing. More recently, and more interesting for our purpose, are the "dynamic" controllers, where the feedback dynamics have the same time-scale of the flow dynamics.

Real-time controllers are designed from the application of the control theory and applied to systems representing flow dynamics. This process can represent a huge difficulty due to the variety of features of each discipline, control theory and fluid mechanics. Bewley (2001) pointed out the importance of having a deep knowledge of both areas and capitalize technological and theoretical development in order to deal with problems arising in the research field. With this spirit, different control techniques have been developed and successfully applied to both numerical and experimental flows.

In this study, active closed-loop control has been attempted to suppress cavity oscillations. Closed-loop control methodologies applied to cavity problems need a model that represents the most important dynamics. The quality of the model depends on the number of sensor measurements, their location in the cavity and their capacity to capture flow information. Many different modeling techniques have been used in recent years, either based on flow physics or empirically identified directly from an experiment. The most used techniques are system identification and projection methods, but also physics-based models as in Rowley (2005).

1.3 Model reduction

The substitution of the high dimensional problem with a reduced model leads to an easy optimization of the control law. Thus, the latter depends on how flow dynamics are represented in the model. One of the most important objective of flow control is then to obtain a reduced model that, in spite of low dimension, is capable to accurately reproduce the input-output dynamics.

In the majority of studies on transitional flow control, linear models have been considered to represent the dynamics of the linearized Navier-Stokes equations, as reviewed in Kim and Bewley (2007). The hypothesis of applicability is that linearized models faithfully reproduce input-output dynamics and in the last decade this hypothesis has been widely supported, at least at sufficiently low Reynolds number. Clearly, the limit of such models is the inability to capture turbulent dynamics related to different length and time scales, typically non linear. On the other hand, a non-linear approach can be effective

even in super-critical conditions (Bergmann and Cordier, 2008). Independently from the approach, a reduced model musts rely on a discretization of the high-dimensional problem. In this thesis, we consider reduced basis approaches, that consist in the projection of the flow equations onto a low-dimensional basis reproducing some important features of the input-output dynamics. In particular, we focus on Global Modes (GM), Proper Orthogonal Decomposition (POD) and balanced POD (BPOD).

Model reduction can be obtained by projection of the high-dimensional problem onto global modes. These modes are computed in the stability analysis and represent the eigenvectors of the linearized Navier-Stokes operator (Sipp et al., 2010). Due to their non-orthogonality, an adjoint basis, obtained through the solution of the adjoint Navier-Stokes operator, is also required. Through a linear combination of global modes, full system's linear dynamics can be accurately expressed. A reduced model from projection onto global modes has been used in boundary-layer flows to model optimal perturbations and linear growth in the works of Åkervik et al. (2008), Ehrenstein and Gallaire (2005) and Alizard and Robinet (2011). Since global modes are related only to system dynamics, Lauga and Bewley (2004) observed that with the introduction of measurements and forcing, global modes expansion is no longer appropriate to capture the modified dynamics. However, closed-loop control using reduce-order models obtained with this method have been studied in Åkervik et al. (2008) and Ehrenstein et al. (2012). Barbagallo et al. (2009) used the least stable modes as basis for the reduced-order model.

Control approaches in recent years have been developed on reduced-order models mostly based on Proper Orthogonal Decomposition (POD) method. This technique has the objective of obtaining a low-dimensional orthonormal basis, so that the velocity field can be expressed as a linear combination. This technique is well suited for fluid mechanics problems (Lumley, 1967), since it does not require any information of the flow, but relies only on snapshots of the velocity field, that can be easily obtained from numerical simulations as well as experimental PIV acquisitions. This method turns into solving an eigenvalue problem, whose size is equal to the number of snapshots (Sirovich, 1987), from a correlation term computed as a scalar product of the velocity field. Resulting eigenmodes (POD modes) represent the most energetic structures that can be controlled and their dynamics are modulated by time projection of the velocity field onto the POD basis. Model reduction with POD has been applied to numerous works to describe the energy-based dynamics as in Noack et al. (2003) and Rowley et al. (2004). This spatial decomposition technique is usually coupled with Galerkin projection, leading to the class of methods called Galerkin-POD methods, widely used in flow control. Successful results in this domain can be found in the works of Bergmann and Cordier (2008) on a cylinder wake, Barbagallo et al. (2009) on a cavity flow and in the experimental work of Samimy et al. (2007).

A further step in POD-based model reduction consists in balanced truncation. It is recognized that to reduce the order of the problem, both controllabilty, i.e. the ability of the applied forcing to reach flow states, and observability, i.e. the ability of flow states to register at the sensor locations, are equally important. Moore (1981) first introduced a model reduction where the basis balances these two characteristics and he applied it to systems linearized about stable steady states. In flow control a similar basis is well suited to represent the information from the actuator to the sensor providing a reduced model subjected to optimal control design. These balanced models were also consequently applied to unstable systems (Zhou et al., 1999) and non-linear control problems (Scherpen, 1993; Lall et al., 2002). More recently, Rowley (2005) combined the balancing procedure and Proper Orthogonal Decomposition (POD) modes. Since then, this technique has been applied to channel flows (Ilak and Rowley, 2006; Ahuja and Rowley, 2008; Ilak and Rowley, 2008) and boundary layer problems (Bagheri et al., 2009; Ahuja and Rowley, 2010). For the cavity flow problem we refer in this study to the balancing procedure and detailed results provided by Barbagallo et al. (2009).

1.4 System identification

In flow control, the process of going to observed data to a mathematical model is called System Identification (Ljung, 1999). This technique covers the problem of building a model when previous history is barely known and only dynamics features are available. The resulting model can be then considered as a black box between the actuator and sensor that, accordingly to Kim and Bewley (2007), are the only dynamics required for compensator design. For this reason, system identification provides models that are well suited for control in experimental applications. Some successful examples in this domain are the work of Kegerise et al. (2004) on the suppression of flow-induced cavity tones, the adaptive control of a separated boundary layer made by Tian et al. (2006), the closed-loop control of the reattachment length downstream of a backward-facing step by Henning and King (2007), the suppression of the gust effect on an airfoil studied by Kerstens et al. (2011) or the approximation of linearized Navier-Stokes equations through system identification obtained by Hervé et al. (2012).

The range of different techniques to obtain an identified model is wide and new solutions have been continuously proposed in recent years. In this research we focus on those techniques where the model describing input-output behavior is obtained from projection onto Navier-Stokes equations. Commonly, this procedure is applied to flow equations linearized around a steady base flow. The techniques of this type most used recently are Auto-Regressive eXogenous (ARX) models (Huang and Kim, 2008), in which the error is modeled as a white noise, and Auto-Regressive Moving-Average eXogenous (ARMAX)

models (Hervé et al., 2012), where a colored noise is considered in the algorithm without an *a priori* knowledge of the color. Despite the technique used, the system identification procedure can be summarized as follows. From the available measurements and inputs, a set of candidate models is analyzed. A model is a predictor of the next output from the process, given past observations and a set of parameters. The structure of the model thus depends on the dynamics of the flow to be represented and results as a combination of constant coefficients, to be determined, and time regressors, i.e. combination of past measurements and inputs. Because of unpredictable dynamics, the next output is approximated with an unknown error. Constant coefficients can be computed through a least-square method that minimizes this error. The model obtained is then tested on a different set of data.

An alternative is represented by the identification of linear system matrices, known as subspace identification and first introduced by Kalman (1960). This technique is widely used in control problems based on Linear Quadratic Gaussian (LQG) regulators, since it provides an approximation of the noise covariance as required in control design. On this matter, Juillet et al. (2013) proposed a technique for evaluating a combined approach involving subspace identification and optimal control design. Among other closed-loop subspace identification methods, we can cite the work of Chiuso and Picci (2005) on the consistency of two different subspace identification methods based on a whitening filter approach and the error estimation approach from a high-order ARX model proposed by Qin and Ljung (2003). A more detailed review of methods based on subspace identification technique can be found in Qin (2006).

1.5 Robust control

Linear-quadratic optimal regulators have impressive robustness properties, including guaranteed classical gain margins. This result is only valid, however, for the full-state case. If observers or Kalman filters are used in the implementation, no guaranteed robustness properties hold. In light of these observations, the robustness properties of control systems with observers need to be separately evaluated for each design.

The present study provides procedures to directly target robustness. Loop Transfer Recovery (LTR) technique already improves robustness in the Linear Quadratic Gaussian (LQG) regulator by adding a fictitious control noise. Cortelezzi and Speyer (1998) introduced the Multi-Input-Multi-Output (MIMO) LQG/LTR synthesis, combined with model reduction techniques, for designing an optimal linear feedback controller. Among robust regulators, the $\mathcal{H}_\infty$ control has been introduced by Doyle et al. (1989). It consists in a worst-case disturbance (min-max) problem where the objective is to find the particular disturbance to which the compensator is most sensitive and nonetheless the amounts of

feedback are kept as small as possible. A worst-case disturbance ($\mathcal{H}_\infty$) controller has been developed by Bewley and Liu (1998) to stabilize unstable disturbances in transitional flow. Such reduced feedback improves robustness in the system model and results in a smaller demand on the actuator. The problem of finding a robust control is intimately coupled with the problem of finding the worst-case disturbance in the spirit of a non-cooperative game. The cost functional is simultaneously maximized by the disturbance and minimized by the control. The principle behind the robust control theory could be intuitively seen as a compromise seeking the "best" control that stabilize the flow, between the smallest control effort and the worst effect done by disturbances. A control which is effective even in presence of a worst-case disturbance will be robust to a wide range of other possible disturbances.

In the present study a $\mathcal{H}_\infty$ controller is developed considering unstructured uncertainties as disturbances, as described by Burl (1998). This type of perturbation can be related to the internal stability robustness through the Small Gain Theorem (SGT) leading the $\mathcal{H}_\infty$ controller to directly target robustness instead of performance. This approach is known in control community as the input-output approach and is one of the well-accepted and widely-used methods to study stability of systems. Initiated by Zames (1966), the small gain theorem says that the feedback loop will be stable if the loop gain is less than one. This simple rule has been a basis for numerous stabilization techniques in control theory. However, the application of this method cannot be found in flow control problems.

1.6 Objective of the thesis and outline

In this work, two key points of closed-loop control applications are investigated: model reduction through system identification based on observable dynamics and robustness to stable perturbations. The aim is to build a controller suited for experimental applications. With this purpose a subsonic, bi-dimensional cavity flow has been studied through experimental activity and numerical simulations.

As described in Sec. 1.4, system identification technique has been successfully applied to closed-loop linearized control problems. In particular, auto-regressive models permit to predict the measurable output through a linear combination of previous acquisitions and known inputs. However, real applications can be found only for transitional flows at low Reynolds number where non-linear effects are not predominant. Dealing with these non-linearities in real cases is a challenge that can be engaged with an approach based on the system identification technique. This is the first purpose of this thesis, the realization of a non-linear identified model based on experimental acquisitions. The expectation is that such a model could deal with the oscillating behavior of the cavity flow.

Optimal control theory has been widely used in flow control applications. However, many aspects and features of control theory are not considered in fluid mechanics problems that have been historically focused on classical control methods as linear quadratic control. The reason of this "lack of communication" between control and fluid mechanics communities is that the two disciplines have been tied together only in the last two decades and, even though many progresses have been accomplished, the huge potential of control theory has not been fully exploited in flow control. An example is represented by the input-output approach, a technique deeply employed in automatic control to stabilize feedback systems and almost unknown in fluid mechanics domain. The main objective of the present work is then to build a controller based on this technique in order to increase robust behavior to stable perturbations showing that modern automatic control methods can be suited even for flow control applications and can lead to impressive results.

1.6.1 Outline

This thesis is structured as follows: a first part where a real case has been analyzed through an experimental activity and a second part in which robust control is developed from numerical simulations.

In chapter 2 the experimental activity conducted on the S19 wind tunnel is described. The equipment is functional to perform closed-loop control. The qualification measurements are highlighted in Sec. 2.1, focusing on hot-wire measurements, steady and unsteady pressure acquisitions. Particular emphasis is given to frequency content. PIV technique has been used to give a time-resolved description of the flow dynamics and its principle, along with qualitative results, is shown in Sec. 2.2.

The identification of a non-linear reduced-order model is the main subject of chapter 3. Non-linear models are introduced in Sec. 3.1, where the structure of the identification algorithm is defined from a POD basis. TR-PIV measurements are then used to compute POD modes and time projections in Sec. 3.2. In this section, great relevance is also given to time-filtering process over PIV snapshots. Finally, the different phases of the identification process are described in Sec. 3.3, with a detailed analysis on the role of each parameter.

Closed-loop robustness analysis is conducted in chapter 4. Numerical simulations and model reduction are described in Sec. 4.1 and 4.2. The definition of the closed-loop system is given in Sec. 4.3. Here, key roles are represented by the closed-loop transfer functions and perturbations. In the following Sec. 4.4, performances and robustness indicator are defined. These quantities represent the comparison parameters for the control strategies studied. A new interpretation of robustness to stable perturbations is also given. In Sec. 4.5 results of classic control strategies as LQG, LQG/LTR and classic $\mathcal{H}_\infty$ control are shown. These results are compered with those of the robust control proposed in Sec.

4.6. Finally, the behavior to unstable perturbations of the most robust compensator is analyzed in Sec. 4.7, with considerations of future perspectives.

Chapter 2

Experimental activity

In this chapter, we describe the experimental activity carried out in the continuous closed-loop subsonic ($Ma \approx 0.1$) wind tunnel "S19Ch", on the Chalais-Meudon site. We aim at performing a real feedback control capable of suppressing cavity oscillations. To this purpose, the control strategy will consider the possibility of using unsteady measurements, such as "traditional" sensors (pressure probes, hot wires and hot films), as well as time-resolved PIV images. The equipment installed on the wind tunnel has been devised for this objective.

The model mounted in the S19Ch wind tunnel is represented in Fig. 2.1. It consists of a cavity of length $L = 134mm$, original depth $D_o = 210mm$ (then modified to $D_m = 900mm$ in order to modify the fundamental frequency of the cavity) and span $W = 300mm$. Reference conditions measured upstream the cavity, are closed to ambient temperature and pressure: $T_{ref} = 293.7 \pm 10K$ and $P_{ref} = 100383 \pm 600Pa$. The related Reynolds number is then $Re \approx 10^5$.

The experimental setting is equipped with an acquisition system that simultaneously acquires 16 different channels of measurement. Among these, 7 channels are dedicated to unsteady pressure acquisitions; 3 are for relative steady pressure $P_{total} - P_{atmospheric}$ and $P_{static} - P_{total}$ measured upstream the cavity and $P_{static} - P_{atmospheric}$ measured at 28 points along the vein; 1 for a hot-wire probe that could be displaced through a system capable to cover an area of $25cm$ in the streamwise direction and $10cm$ in the vertical direction; 2 channels for temperature acquisitions of T_{ref} and T_{total}. Remaining channels have been eventually used for tests and minor purposes.

To obtain time-resolved PIV snapshots (to have a description of the flow dynamics, to build reduced order models and to be used as sensors in a closed-loop control scheme), a high-frame rate camera and a double cavity laser have been installed. The observation window of 1280×500 pixels is focused only on the shear layer, giving a description of the oscillating motion, but the recirculating dynamic on the bottom of the cavity is not captured.

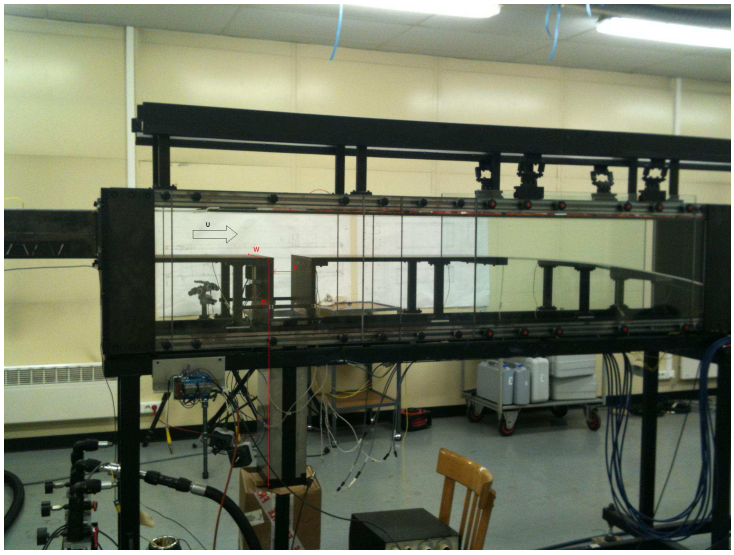

Figure 2.1: Cavity model installed in the S19Ch wind tunnel.

A field-programmable gate array (FPGA) has been included to quickly process information between the TR-PIV system, the actuator (here a low-frequency flap) and the unsteady pressure measurements. In the perspective of closed-loop control, considering the low characteristic frequency of the cavity flow and consequently the low operating frequency of the actuator, the process of analysis and impulse granted by the FPGA system can be considered approximately as real-time process.

The chapter is structured as follows: in Sec. 2.1, measurement techniques and qualification results are presented. These measurements are useful to characterize the flow in terms of boundary layer width, pressure, turbulence intensity and frequency bandwidth, in order to provide the parameters needed for the PIV campaign and the actuator design. Results of TR-PIV are presented in Sec. 2.2. In particular, time resolution permits a high detail of information as small structures displacement and vorticity evolution, within a characteristic period.

2.1 Wind tunnel qualification

In this section we analyze measurements conducted at the wind tunnel S19Ch in order to qualify the vein. The cavity model has been conceived and installed for this specific study and for this reason no reference data was available. Hot-wire measurements in the boundary layer and the free shear layer and pressure measurements, both steady and unsteady pressure, have helped to characterize the flow over the cavity and to modify the geometry in order to have lower and more manageable frequencies.

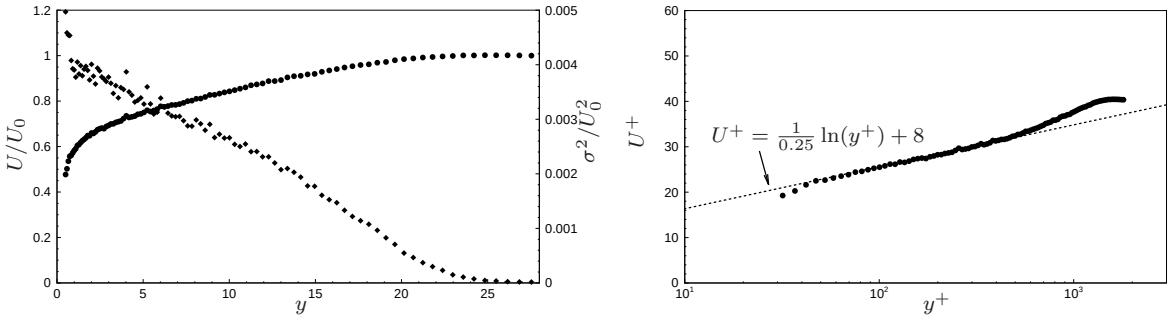

(a) (b)

Figure 2.2: (a) Wall normal evolution of the normalized velocity (circles) and the related variance (diamonds). (b) Scaled velocity in wall units.

2.1.1 Hot-wire measurements

Hot-wire anemometry technique is mostly used to measure turbulence in air flows and it is based on a heat/convection correlation principle. A very thin wire, generally made of tungsten, of diameter ~ 0.5 to 5 μm and length 0.3 to 1 mm, when placed in a flux of air, changes its temperature and so its resistance. Most hot-wires operate at constant temperature, so the change of air velocity causes an increment in the voltage necessary to keep the temperature constant. This imbalance is measured by the data acquisition system and converted by a calibration law to a local velocity.

In the wind-tunnel qualification campaign, the hot-wire technique has been used to obtain a measurement of the upstream boundary layer profile, to characterize the cavity flow frequency and to compute the turbulence level in the flow.

Boundary layer

The upstream boundary layer is measured with a Dantec 55P15 probe, that permits with its specific geometry to approach the wall up to 0.5 mm. Measurements are taken in the upstream region, with the cavity closed in order to have no acoustic disturbance. Results are represented in Fig. 2.2. The first plot (Fig. 2.2(a)) shows the evolution of the normalized velocity U/U_0 in the direction normal to the wall, y, and the corresponding non-dimensional variance. This measurement allows to compute boundary-layer thickness: the 99% thickness $\delta_{.99} = 21.24mm$, the displacement thickness $\delta^* = 3.35mm$, the momentum thickness $\theta = 2.55mm$ and the shape factor $H = 1.31$.

The second plot, shown in Fig. 2.2(b), presents an evolution of the boundary layer in estimated scaled wall units. Since it is not possible to compute the exact value of the velocity very close to the wall, the viscous velocity has been estimated to have unitary value. Results show only the buffer layer around $y^+ = 10$, the log-law region from $y^+ = 3 \times 10^1$ to 2×10^2 and the outer region. The viscous sublayer is clearly not available

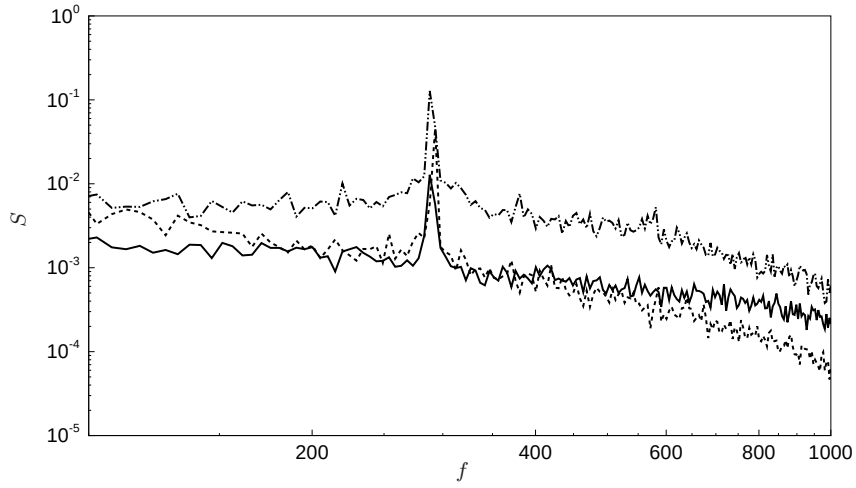

Figure 2.3: Spectra of measured signals (in V) at three different locations in the cavity: $x = 4mm, y = 0mm$ (solid line), $x = 60.7mm, y = -25mm$ (dashed line) and $x = 130mm, y = 0mm$ (dashed-dotted line).

because of the limits of the hot-wire technique when approaching the wall. Note that the logarithmic behavior is well represented, but since the scaling is just estimated, the describing law shows a value of the Von Kármán constant quite different from the classic 0.41.

Mixing layer

The mixing layer has been investigated by displacing a Dantec 55P11 hot wire through an explorer mounted on the top of the cavity, with the flow nominally driven at $40m/s$. The region investigated by the hot-wire probe is a rectangle of 21 points in the longitudinal direction, starting at $4mm$ from the upstream edge of the cavity to $4mm$ to the downstream edge, and 6 points in the normal direction, from $y = 0mm$ to $-25mm$ inside the cavity. These measurements have been used to characterize the frequency range of the cavity. In Fig. 2.3 we observe three spectra of the anemometer acquisition at three different locations: two points close to the upstream and the downstream edge and one inside the cavity in the recirculating region. Near the corners, the spectra presents a peak at 288 Hz, while at the lowest location the peak is located at 293 Hz. This small difference is due to the lack of resolution, since the hot-wire signal is acquired at 20 kHz and composed of 4096 points and the passage to the frequency domain implies a Fourier transform that leads to a frequency step of 4.88 Hz.

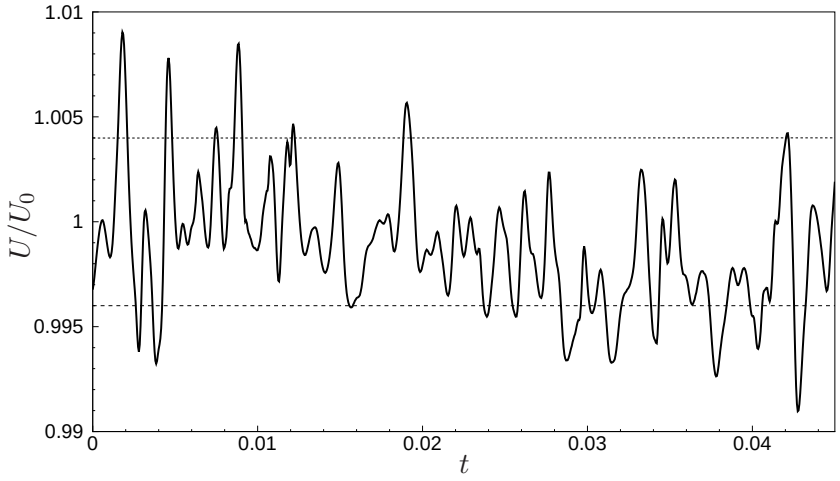

Figure 2.4: Time behavior of a normalized velocity signal acquired with a hot-wire probe located in the free stream.

Turbulence intensity

The quality of a wind-tunnel flow is commonly expressed by the turbulence intensity, also often referred to as turbulence level, defined as:

$$I \equiv \frac{u'}{\bar{U}}, \tag{2.1}$$

where u' is the root-mean-square of the turbulent velocity fluctuations and $\bar{U}$ is the mean velocity. It represents how statistically a flow fluctuates around its mean value, so it is a good representation of how "clean" the flow in a wind tunnel is and it can be easily calculated from a hot-wire acquisition, knowing the mean value and the variance. For this wind tunnel, the turbulence level is $I \approx 0.4\%$ and it is a typical value for high-quality wind tunnels.

In order to better understand the meaning of the turbulence level we can observe Fig. 2.4 where a normalized velocity signal measured in the free stream is represented. The horizontal lines stand for the bounds of the 0.4% of the normalized velocity. We can note how the majority of the oscillations are included between these bounds.

2.1.2 Pressure measurements

The S19 wind-tunnel is equipped with 26 static pressure probes and 7 unsteady pressure Kulite transducers. In this section we show results for both measurement techniques.

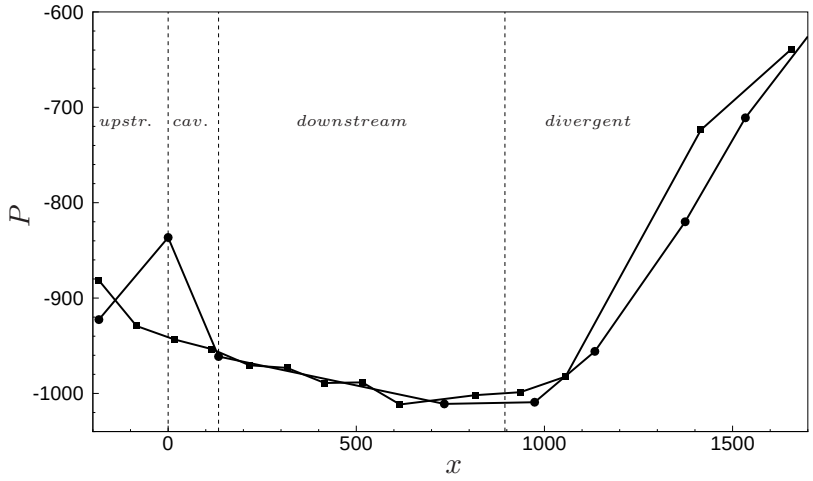

Figure 2.5: Steady pressure measurements along the model section. Pressure values are expressed in Pa, while the longitudinal direction is in mm. Top static probes are represented by squares, bottom probes by circles.

Steady pressure measurements

A series of static pressure probes has been posed along the wind tunnel, from a location 184 mm upstream the cavity to the divergent section, placed on top and on bottom of the vein. Fig. 2.5 shows the longitudinal behavior of the static pressure, with respect to the atmospheric pressure. There is no remarkable difference between the top and the bottom acquisitions, as expected, except for the probes located on the cavity vertical walls. In detail, there is a significant jump in pressure inside the cavity at the upstream wall, while on the downstream wall this jump is not present. The static pressure continues to diminish along the x direction until the divergent region where the flow is finally decelerated.

Unsteady pressure measurements

Unsteady pressure acquisitions are taken from 7 Kulite transducers XCQ-093-15A (15 PSI). Two of them are positioned on the upstream wall of the cavity, four on the downstream wall and one on the bottom. From these acquisitions it has been possible to obtain a power spectra of the cavity, verify that the flow is actually two-dimensional and compare results with those obtained with the hot-wire anemometer. The advantage of using this kind of transducers is a high sampling frequency, here $20kHz$, for 200 blocks of 4096 points, giving a frequency resolution of 4.88 Hz.

In Fig. 2.6 is shown the Sound Pressure Level (SPL) obtained from the power spectra of three different Kulites, one at the upstream wall, one at the downstream wall and one

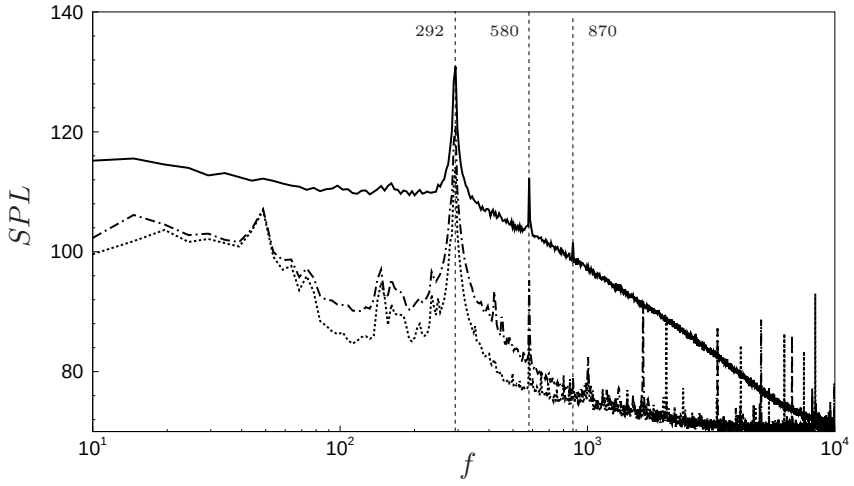

Figure 2.6: SPL, expressed in dB, of unsteady pressure measurements. Transducers are located on the upstream wall of the cavity (dashed line), on the downstream wall (solid line) and on the bottom (dashed-dotted line).

at the bottom wall. The SPL is computed through the relation

$$SPL(dB) = 20 \log_{10} \left(\frac{\sqrt{S}}{p_{ref}} \right) \tag{2.2}$$

where S is the power intensity of the pressure measurement and p_{ref} is the reference pressure equal to $20\mu Pa$ that is considered as the threshold of human hearing. We can observe that all the signals present a peak at $292Hz$ and the second and third harmonics are located at 580 and $870Hz$. Comparing this result with that obtained from the hot-wire probe we can define the characteristic frequency of the cavity as $f_c = 290Hz$. Other considerations can be done on this figure, as the presence of high-frequency noise measured upstream and on the bottom of the cavity.

2.1.3 Frequency adaptation

The objective of this study is to perform a feedback control of a cavity flow. To this aim, an actuator needs to be conceived and the mechanical design imposes some constraints, namely a frequency bound. The imposed maximum range of frequencies that a motor-based actuator on the actual market can afford is about 150 Hz. The wind-tunnel qualification measurements have determined the characteristic cavity frequency as 290 Hz, a frequency twice as high than the one requested by the design of the actuator.

In order to modify the cavity frequency, we use a frequency prediction model as a function of the cavity depth, proposed by East (1966), based on the acoustic mode resonance

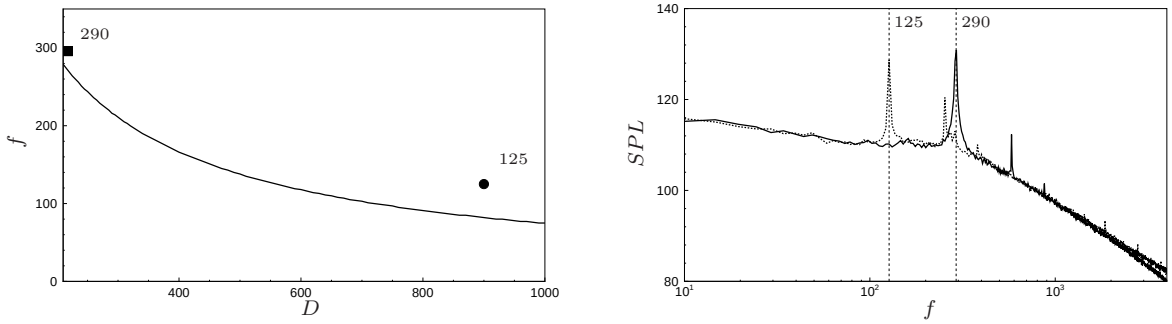

(a) (b)

Figure 2.7: (a) East model for frequency (in Hz) prediction as a function of the cavity depth, D (in mm). The small square represents the characteristic frequency at the original depth, while the circle stands for the frequency obtained after cavity depth modification. (b) Comparison of SPL (in dB) obtained from the same transducer measurement with the original cavity (solid line) and the modified one (dashed line).

in a deep cavity flow. The model reads as follows:

$$f = \frac{a}{D}\frac{0.25}{1 + A(L/D)^B} \tag{2.3}$$

where a represents the number of the harmonic, L and D are the length of the cavity and the depth, respectively, and A and B are empirical coefficients. In Fig. 2.7(a) is represented the prediction model behavior considering a range of depth from the original cavity depth of 210 mm up to 1 m. We can observe that for small depths there is a good correspondence with the actual frequency, while for higher values of D, the model seems to be less accurate. The circle in this plot represents the measured frequency after modifying the cavity depth up to $900mm$. In Fig. 2.7(b) two SPL signals from the same transducer acquisition show how after the geometry modification a smaller and satisfying frequency of 125 Hz has been obtained.

2.2 Time-Resolved PIV

The Particle Image Velocimetry (PIV) technique has been used to characterize the velocity field (U, V) in the cavity mixing layer. The interest is to acquire a series of snapshots at high frequency in order to reconstruct flow dynamics through a modal decomposition. To this aim, a two-dimensional two-components Time-Resolved PIV (2D-2C TR-PIV) technique has been employed. In this section, the general principle of this method is introduced as well as results acquisition and snapshots post-processing.

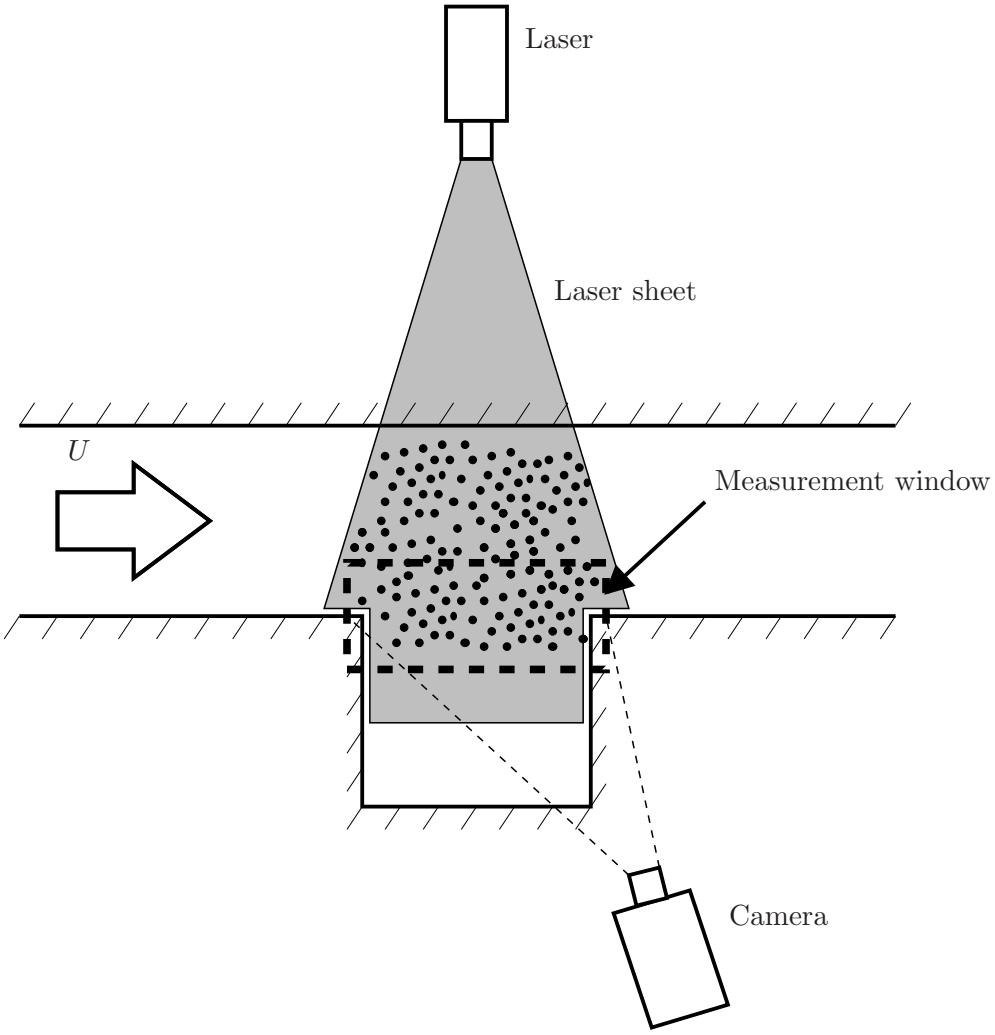

Figure 2.8: Scheme of a 2D-2C PIV acquisition for a cavity flow.

2.2.1 The PIV technique

The principle schematized in Fig. 2.8 is valid for the classic PIV as well as the TR-PIV. It consists in a flow seeded with sprayed oil particles of diameter d_p; a laser source generates a laser sheet which defines the measurement plan; when the laser hits the particles they are illuminated and a camera placed perpendicularly to the sheet acquires a series of pairs of images separated by a time step dt. The velocity field is then calculated through a software that correlates each couple of images in order to find particles' displacements.

2.2.2 TR-PIV measurements

In this study, the TR-PIV technique has been considered. The difference from the classical PIV is the high-frequency acquisition that permits a good time resolution. Time-resolved PIV measures velocity fields and turbulence quantities of transient phenomena. The time-resolved PIV allows to obtain the "real" quantities of transient and turbulent flows

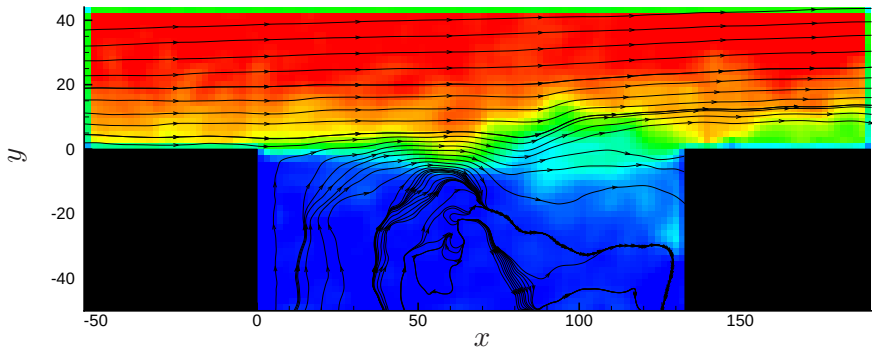

Figure 2.9: TR-PIV snapshot of the longitudinal component U and flow streamtraces. Dimensions of the axes are in mm. The origin is the left corner of the cavity.

because of the highly-defined time resolution. LaVision's *FlowMaster* time-resolved PIV systems include Phantom V.12 digital high-speed camera with 6242 Hz frame rate at full resolution of 1280 $\times$ 800 pixel, dual cavity high-repetition rate solid state laser up to several 10 mJ per pulse and up to 20 kHz repetition rate. All components are fully controlled from the DaVis software and LaVision's High Speed controller (HSC). The HSC enables an easy use of high speed systems with typically demanding trigger requirements like the synchronization of the external frequency of the device with the recording rate of the measurement system.

The camera field of view has been fixed at $244mm \times 94mm$, with a magnification rate of 5.45 px/mm, so that the mean displacement of a particle between two images is 8 pixel. The nominal longitudinal velocity considered for the entire campaign is $U_0 = 34m/s$ and, as stated in the previous section, the cavity fundamental frequency is $f_c \sim 125Hz$. In order to have a time resolution defined enough to permit the reconstruction of the cavity dynamics, we want to have at least 20 points per period, so the sampling frequency is $f_s = 3kHz$ ($6kHz$ for single image). For each acquisition it is possible to store 7500 images, corresponding to about 60 periods.

Velocity field estimation has been realized through the software FOLKI-SPIV (Champagnat et al., 2011). Particles' displacement is computed by a correlation made on each pair of images divided in interrogation windows of 15 pixels. In Fig. 2.9 is shown a snapshot acquired with the TR-PIV technique. The quality of the camera acquisition permits to appreciate the velocity fluctuations in the mixing layer. The oscillating behavior is clearly visible as well as the cavity recirculation on the bottom of the cavity, evidenced by velocity streamstraces.

The high spatial and time resolution allows also to compute and observe the evolution of vortical structures. In Fig. 2.10, the vorticity component ω_z is represented in a series of snapshots that covers an entire oscillating period. The characteristic behavior of the

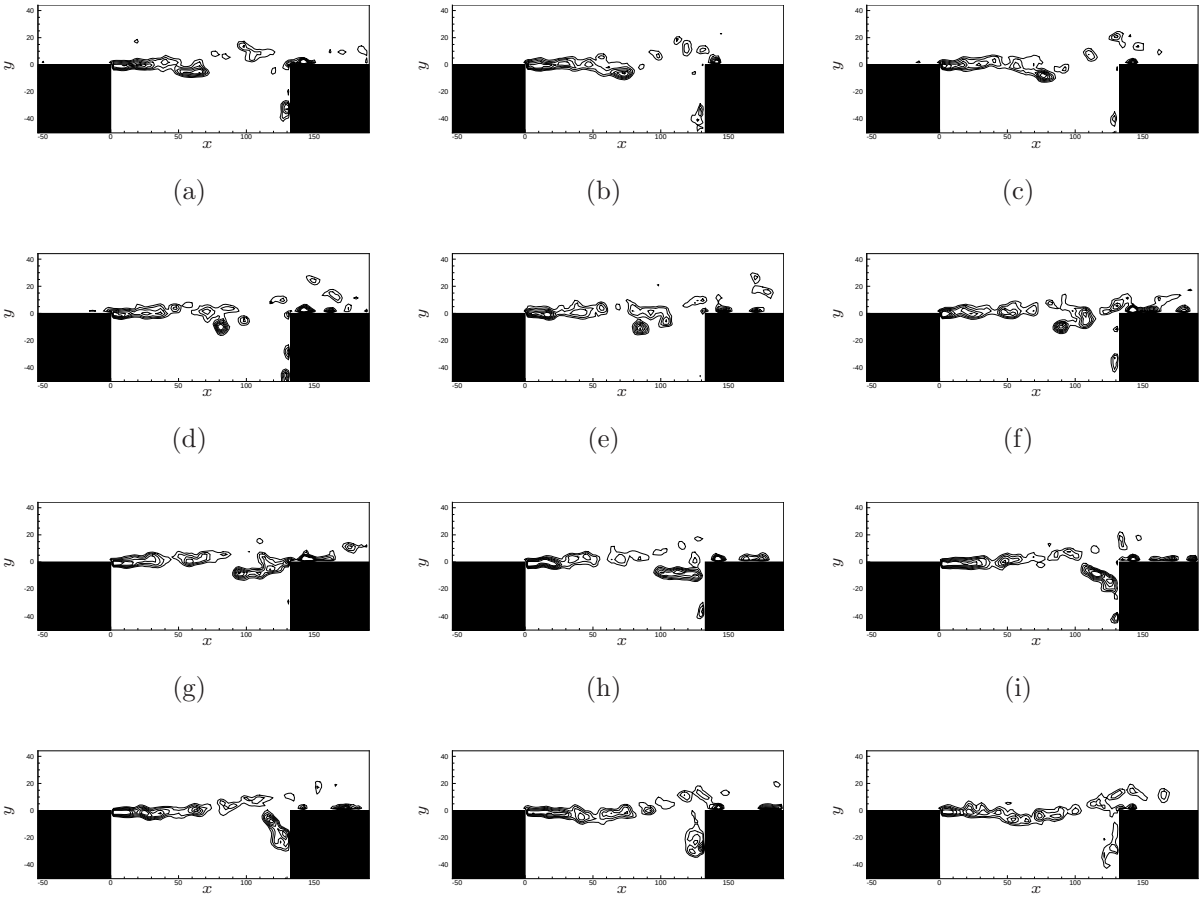

Figure 2.10: Vorticity ω_z development over a characteristic period.

cavity mixing layer can be followed through time by observing a particular structure formed at $x = 50mm$ in Fig. 2.10(a). This eddy progressively detaches from the leading edge vorticity tounge (Fig. 2.10(b)-2.10(d)), regroups with smaller eddies (Fig. 2.10(e)-2.10(g)), impacts on the downstream wall (Fig. 2.10(h)-2.10(k)) and finally looses energy and dissolves (Fig. 2.10(l)). This cycle is representative of the quantity of time information obtained through the TR-PIV.

An important information obtained with the time resolution granted by TR-PIV measurements, is the frequency content. The acquisition capacity is limited to 16 Gb, corresponding to about 8000 snapshots acquired at $3kHz$. With this amount of data, it is possible to produce a power spectra as that pictured in Fig. 2.11. It is obtained from a single point measure over 4096 snapshots. We can observe two important features of the PIV acquisition: the presence of high-frequency noise and the characteristic peak at 126 Hz that confirms qualification results obtained with hot-wire probe and unsteady pressure sensors and represented in Fig. 2.3 and 2.7(b).

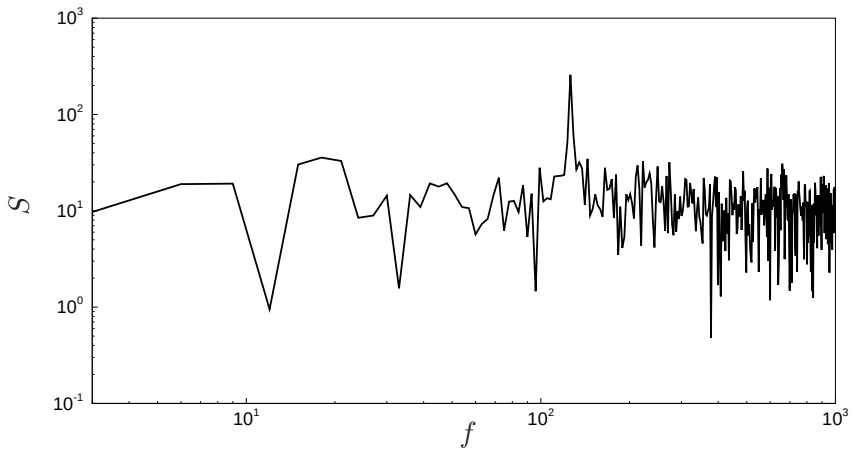

Figure 2.11: Power spectra S of the velocity field computed from TR-PIV measurements. Frequencies are expressed in Hz.

Chapter 3

Non-linear model identification

This chapter describes the system-identification technique used to obtain a non-linear reduced model of a cavity flow. The interest of studying this approach stands in the possibility of application on closed-loop control of oscillating flows. The cavity flow characterized in the previous section is used to develop the necessary tools to obtain the reduce model. It consists on a oscillating flow with a well-defined peak at 126 Hz, but the dynamics are strongly non-linear. This non-linearity has to be taken into account, since the reduced model is derived directly from experimental measurements.

This approach can lead to important results, but using experimental results, with noise and all the complexities coming from a real case, to identify a non-linear model is a path still not explored. The interest is then to understand the real potential of this technique, focusing on the meaning of each parameter and the consequences generated on the identification process.

As explained, measurements from experiments contain a number of information that can effect the identification. A treatment of these results has to be previewed, in order to simplify the identification of the most important dynamics, namely the first harmonic. The application of filters to real measurements has to consider that the main objective is the closed-loop control that implies real-time alteration of the flow. The effect of introducing delays into the system has to be analyzed carefully.

The chapter is structured as follows: non-linear reduced-order models are introduced in Sec. 3.1. A particular focus is given to those models obtained from Proper Orthogonal Decomposition, as Galerkin projection and system identification, to introduce how the structure of the model comes from the physics of the cavity flow. Sec. 3.2 treats routine to obtain POD modes and time projections that will be used as model regressors. Time-filtering on trajectories are discussed in this same section giving a critical comparison between original data and filtered ones. Last section (3.3) is devoted to the identification process and all those problems caused by non-linearity, time delay and time integration, pointing out the difficulty of this approach with a real non-linear case.

3.1 Non-linear reduced models

Methods of analysis and control of cavity flow oscillations rely on the knowledge of a model representing the most important dynamics of the system. As in many fluids problems, in cavity flows one does need to control only the main instabilities and larger eddies. A model reduction based on an energetic principle should be sufficient to successfully approximate the limit cycle of the cavity tones.

In this section, we then discuss non-linear reduced-order models based on Proper Orthogonal Decomposition (POD). In particular, we focus on reduced model obtained by Galerkin projection of Navier-Stokes equations and on input/output system identification. Galerkin projection, due to its widespread use in closed-loop control, is taken as reference for the algorithm structure design. However, the limitations and drawbacks of its requirements are used to motivate the choice of focusing on the system identification approach to obtain the ROM. In particular, we highlight the advantages of the identification technique, which relies only on dynamics directly observed from measurements.

3.1.1 Proper orthogonal decomposition

The POD was introduced in turbulence by Lumley (1967) and is widely used to extract coherent structures existing in turbulent flows. It consists in finding a deterministic function $\Phi(x, y)$ that describes the spatial location of the most representative structures of the instance $\mathrm{U}(x, y, t)$. The time dependent quantity in our case stands for the velocity field $\mathrm{U} = (U, V)$, acquired from the TR-PIV measurements.

The method used to compute POD, known as *Snapshot method*, has been introduced by Sirovich (1987). For a given set of M snapshots, it reduces to an eigenvalue problem

$$\sum_{i=1}^{M} C(t_i, t_j) a_n(t_i) = \lambda_n a_n(t_j), \tag{3.1}$$

with the correlation tensor $C(t_i, t_j)$, defined through the inner product:

$$C(t_i, t_j) = \frac{\Delta x \Delta y}{4} \left[U_i^* U_j + V_i^* V_j \right], \tag{3.2}$$

where Δx and Δy represent the spatial discretization in the longitudinal and normal direction respectively. The solution of the eigenvalue problem gives M eigenvalues λ_n $(n = 1, ..., M)$ and the associated eigenvectors ϕ_n. The eigenvalues, since the time instance considered is the velocity field, represent the contribution of each mode to the total kinetic energy. By projecting each velocity component onto the normalized eigenvectors, following an energetic criteria that keeps only the most energetic N eigenvalues, the modes $\Phi_n^u(x, y)$

and $\Phi_n^v(x,y)$ can be easily computed as:

$$\Phi_n^u(x,y) = \frac{1}{\sqrt{M}} U\phi_n\sqrt{\lambda_n}, \tag{3.3a}$$

$$\Phi_n^v(x,y) = \frac{1}{\sqrt{M}} V\phi_n\sqrt{\lambda_n}. \tag{3.3b}$$

The obtained functions represent a couple of normalized and bi-orthogonal basis, that is commonly used in model reduction.

The last step is then to compute the temporal projections $a_n(t)$. For each mode the n^{th} trajectory is obtained by:

$$a_n(t) = \frac{\Delta x \Delta y}{4} \left(U^* \Phi_n^u + V^* \Phi_n^v\right). \tag{3.4}$$

The velocity field can be approximated, with relatively good accuracy, with a small number of modes, due to the energetic efficacy of POD basis. This is the great advantage of a POD-based reduction, along with ease in solving an eigenvalue problem from an elevated number of snapshots.

3.1.2 Galerkin projection

The most classical and used model reduction technique in flow control is the Galerkin projection. It consists in projecting Navier-Stokes equations onto an orthogonal basis that energetically reproduces the main features and the input-output behavior of the original system. The choice of the basis is then crucial and can lead to undesired effects. It is typically used in numerical flow control applications, as we will do in Chapter 4, as well as in experimental environments. However, our purpose is not to analyze in detail such technique, but Galerkin projection is here considered for its wide use in flow control, to highlight its limitations and to introduce the resulting structure of the model, with particular focus on non-linear terms. For more details about this technique, the reader is referred to a number of references such as Rowley et al. (2004), Rowley and Batten (2008), Cordier et al. (2008), and Bergmann et al. (2009).

The reduced model is derived from Navier-Stokes equations. The velocity field can be approximated with the product of the POD functions $\Phi_n(x,y)$ with the time projections $a_n(t)$ related to the N most energetic eigenvalues λ_n, as:

$$\mathrm{U}(x,y,t) \approx \sum_{n=1}^{N} \Phi_n(x,y) a_n(t). \tag{3.5}$$

By projection of the Navier-Stokes equations onto the POD basis, the reduced-order

problem becomes, in a general case, a problem for the time projections $a_n(t)$:

$$\frac{\mathrm{d}a_n(t)}{\mathrm{d}t} = A_n + \sum_{i=1}^{N} B_n^j a_i + \sum_{i=1}^{N}\sum_{j=1}^{N} C_n^{ij} a_i a_j, \qquad n = 1, ..., N. \tag{3.6}$$

where coefficients A_n, B_n^i and C_n^{ij} are constants, and N corresponds to the number of modes used in the basis. Note that non-linear terms arise from the projection of the Navier-Stokes equations onto the POD basis. The same structure, will be used in the system identification process, considering only non-linear terms with a physical meaning.

This method is widely used in a great number of applications. However, the reduced models based on Galerkin projection present some notable limitations and drawbacks. The model must accurately describe non-linear dynamics since time-integration could lead to a final state different from the initial assumption. Another problem is represented by the necessity of an observable basis, that implies an adjoint simulation. The spatial representation of the actuator represents a limit in experimental applications and an additional model is normally required. Noise has to be treated with particular accuracy and a statistical information is required for the Kalman filter estimation.

3.1.3 System identification

An alternative approach to obtain a reduced-order model is the system identification. The great advantage of this technique is that it only relies on data arising from simulations or experiments. The system is treated more as a black-box where the only interest is in the frequency response for a given set of known data.

As for Galerkin projection, for system identification technique, a reduction of the model is necessary to perform flow control. The choice of the same basis will lead to the same reduced-order model for a projected or an identified model. In this case, the structure in Eq. (3.6) can be used to identify coefficients from known data. This same structure can be modified by adding more terms if necessary, to improve the predicted output.

Independently from the used algorithm, the system identification technique consists in two different phases: a learning phase followed by a validation. In the first, coefficients are computed with a least-square method in order to fit a known set of data. In the second phase, the same coefficients are kept constant and the capacity of the model to reproduce a different data-set is validated. For this purpose, different parameters and features can influence the final result, as the number of previous known data, basis dimension, non-linearities.

Even though system identification techniques seem to be perfect for experimental applications, it presents some limitations that can be summarized in the following. The

main problem is the treatment of the non-linear dynamics. Dealing with non-linearity is a big challenge since previous positive results are obtained on linear or linearized dynamics and the behavior in a case such as that of the S19 cavity flow is still unknown. In addition, we have to consider that the regression algorithm has to be tuned. Coefficients are usually based on a physical interpretation and setting them properly requires some attention.

3.2 POD modes from TR-PIV measurements

The basis chosen for model reduction is obtained from POD modes, that were obtained by processing TR-PIV acquisitions. In this section the procedure to obtain POD and time trajectories is described. The objective is to have time-evolving projection coefficients that can be used in the system identification procedure. Time filtering will be used to focus on the low-frequency dynamics of the cavity flow.

3.2.1 POD modes and trajectories

The computation of POD modes and projections can be easily achieved from TR-PIV measurements. The series of snapshots acquired in the experimental campaign is divided into different velocities and configurations. For this study, an unperturbed configuration at the nominal velocity of 34 m/s has been chosen to design the reduced-order model.

In order to compute the correlation term in Eq. (3.2), 500 snapshots, corresponding to about 20 periods, are assembled as $N_p \times N_s$ matrix, where N_p is the number of geometric points, equal to 6400, and N_s is the number of snapshots. The geometric parameters used to non-dimensionalize the modes are $\Delta_x = \Delta_y = 1.92mm$.

The solution of the eigenvalue problem leads to the eigenvalues represented in Fig. 3.1. It is evident that the first two modes represent the biggest amount of energy, though lower than the 40% of the total. In order to have a representation of at least 50% of the total energy, we need to consider the first 9 modes ; note that considering more POD modes will increase the number of regressors in the system identification process. A steeper slope in the eigenvalues contribution would be preferred for model reduction and a way to decrease the importance of less energetic modes has to be found.

POD modes Φ_n^u and Φ_n^v are computed from Eq. (3.3). In Fig. 3.2 are represented the first 2, the 4^{th} and the 5^{th} POD modes. The spatial distribution of the POD structures highlights the coupling of each pair of modes, as expected. The same expectation resided in the smaller dimension of eddies for less energetic modes. These results are then coherent with all the previous studies on cavity flows.

The spatial distribution corresponding to the third mode is unexpected, since it shows a strong asymmetry in the longitudinal component (Φ_3^u) and a very weak intensity in the normal component (Φ_3^v), as it can be observed in Fig. 3.3. This mode seems to be

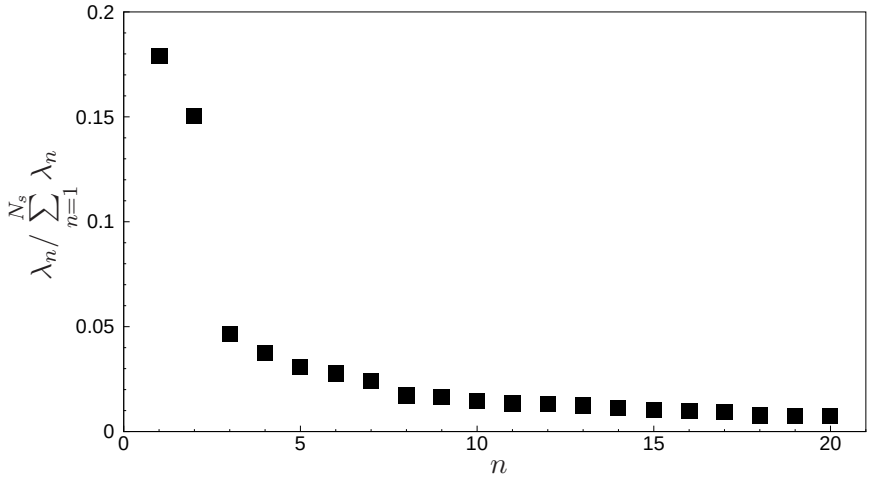

Figure 3.1: Contribution of the first 20 eigenvalues computed from the correlation term corresponding to a set of N_s =500 snapshot acquired at 3 kHz with a flow at 34 m/s.

linked more to the mean flow than to fluctuations, but it turns out that it is a spurious mode. By a detailed observation of velocity fields, we noticed that its presence is produced by reflections generated by the laser sheet which were not completely eliminated. The energetic level is huge in the longitudinal direction and very low in the vertical component. This is caused by the presence of a reflection in the downstream corner of the cavity that influences the velocity field in that region. The result is a discontinuity in the flow direction and consequently a high level of energy. Since this mode does not represent any physical turbulent eddy, we choose not to consider it as part of the basis for model reduction.

The last step is to compute projections $a_n(t)$ that will be used as regressors in the system identification process. From Fig. 3.4 we can observe the time behavior of the first four trajectories, i.e. the projections of the snapshots onto the POD basis, within the first 25 periods. As expected from POD modes, a_1 and a_2 are more regular and more intense than the followers since snapshots are projected to symmetric modes as those in Fig. 3.2(a)-3.2(d). The characteristic frequency is evident in all cases, thanks to the time resolution of 20 point per period. However, even in projections related to the most energetic modes, a modulation is present indicating the presence of several frequencies around the peak at 126 Hz. By observing the smallest projections, a high frequency noise is also remarked. For these reasons an analysis of snapshot filtering seems an interesting contribution.

3.2.2 Time-filtering

The observation of time projections leads us to filter TR-PIV measurements in order to avoid high-frequency noise and modulations around the characteristic peak. This procedure is not common in experimental results, but since the objective is to develop an

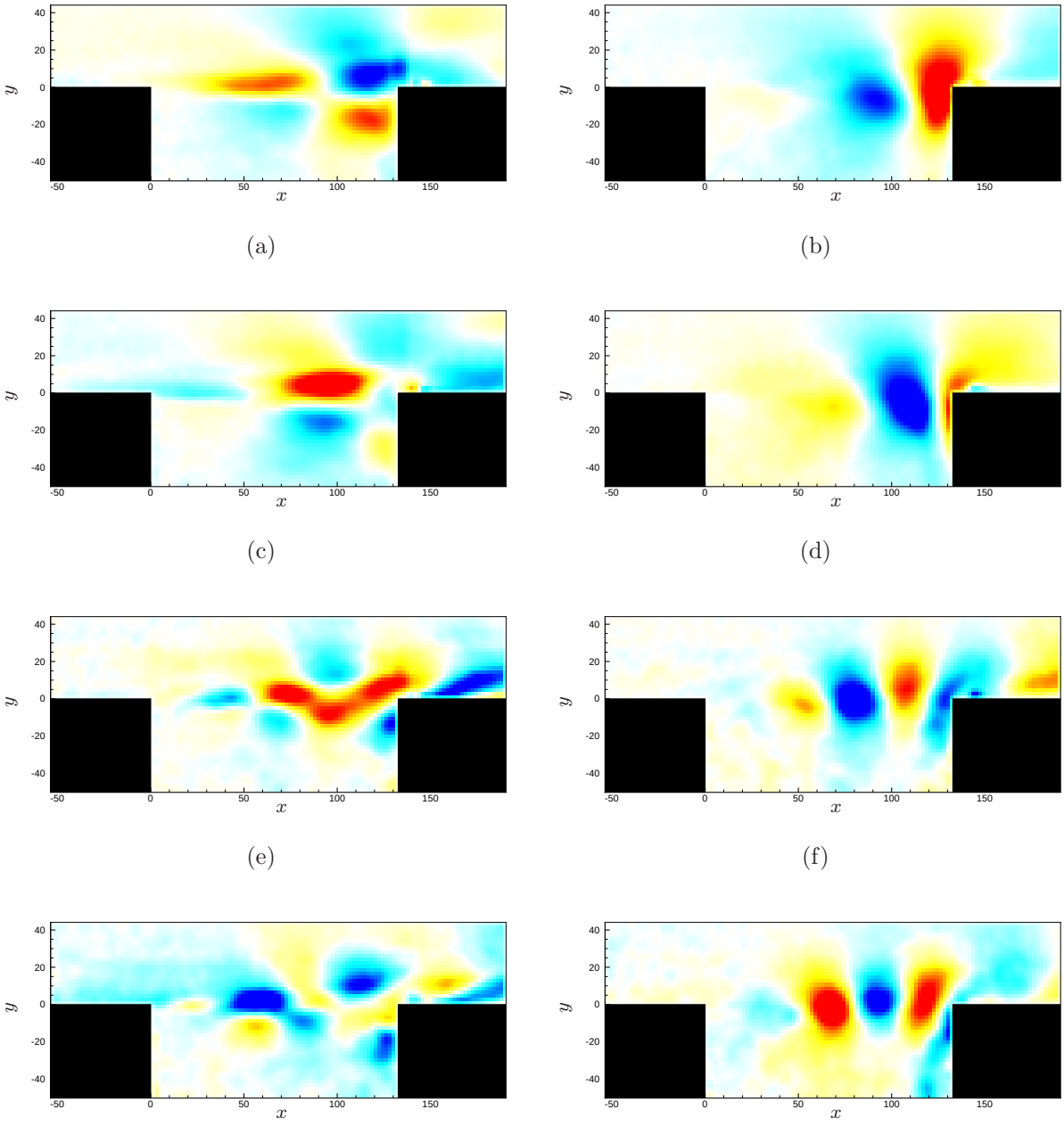

(a) (b)

(c) (d)

(e) (f)

(g) (h)

Figure 3.2: POD modes computed from 500 snapshot acquired at 3 kHz with a flow at 34 m/s. (a) Φ_1^u, (b) Φ_1^v, (c) Φ_2^u, (d) Φ_2^v, (e) Φ_4^u, (f) Φ_4^v, (g) Φ_5^u, (h) Φ_5^v. Levels are from -0.035 to 0.035.

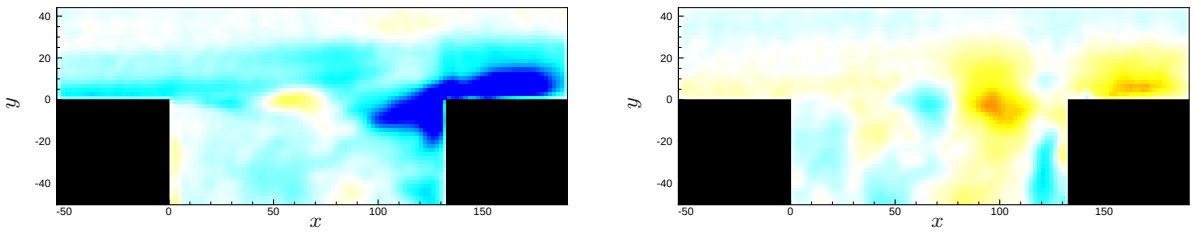

(a) (b)

Figure 3.3: Third POD mode computed from 500 snapshots acquired at 3 kHz with a flow at 34 m/s. (a) Φ_3^u, (b) Φ_3^v. Levels are from -0.035 to 0.035.

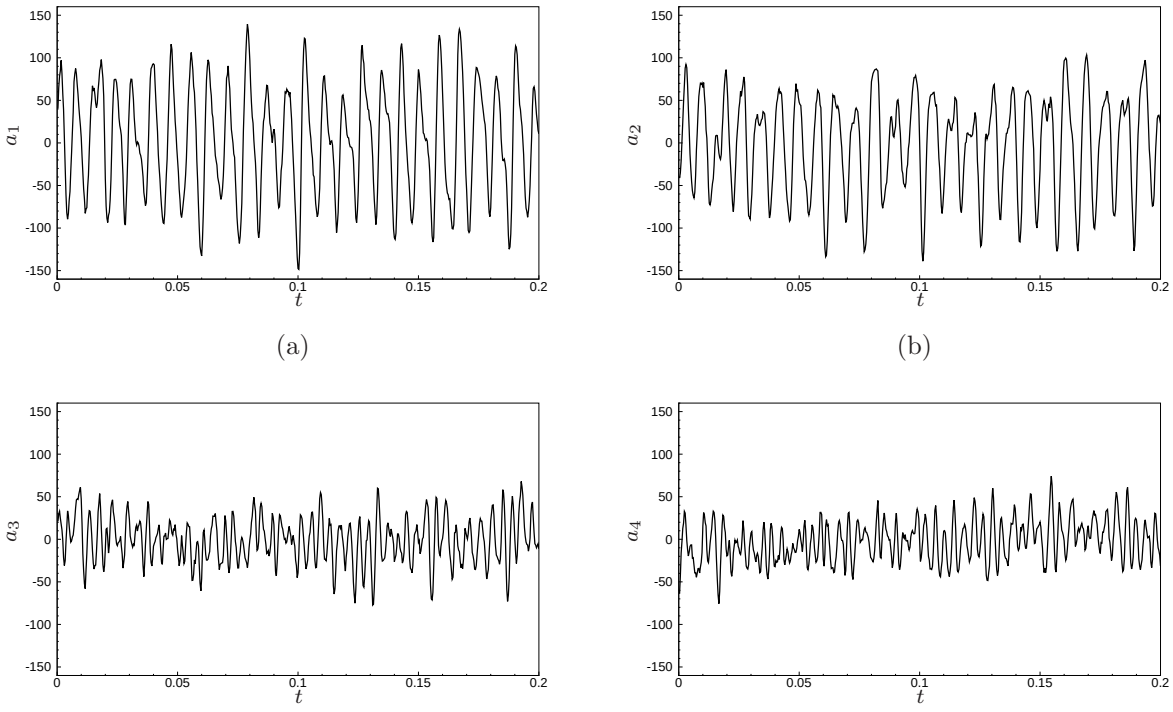

(a) (b)

(c) (d)

Figure 3.4: Time projections corresponding to the first 4 POD modes computed from snapshots acquired at $3kHz$ at a velocity of 34 m/s.

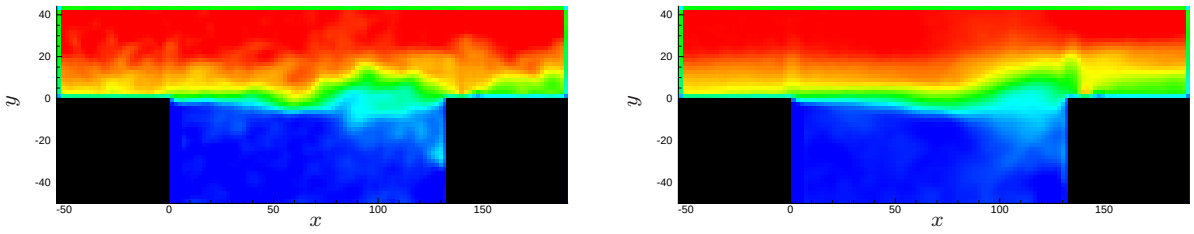

(a) (b)

Figure 3.5: Comparison of the original longitudinal velocity field (a) and the filtered longitudinal velocity field (b) at the same instant t.

algorithm to identify a reduced-order model, it is worth filtering high frequencies in order to simplify the identification procedure.

A Fourier filter has been applied to the original set of snapshots. This filter consists in performing a Fast Fourier Transform (FFT) through the snapshots, putting to 0 all coefficients higher than a certain frequency (in our case 150 Hz) and anti-transform with an Inverse Fourier Transform (IFT). We then processed 4096 snapshots, corresponding to 195 periods, and used the resulting flow fields to compute POD modes and trajectories. This procedure should highlight the most significant dynamics of the oscillating cavity behavior and consequently use, for the identification, a small number of modes, ideally the first two.

In Fig. 3.5, we can compare an example of an original snapshot and the corresponding filtered flow field. The first effect of applying a time filter is that spatial structures are also filtered. We can notice how the smallest eddies, related to the highest frequencies, disappear and only the "main" motion survives.

Another result is the amplification of the reflection on the downstream corner of the cavity. Velocity field at this location is not natural since a discontinuity is present. Unfortunately, this kind of errors are common in optic techniques and are not easily solvable (Scarano and Sciacchitano, 2011). This particular result explains the shape of the 3^{rd} mode. In fact, the presence of a discontinuity is energetic enough to make the related structure to appear among the first modes and probably affects higher order POD modes. In the system identification phase this consequence has to be considered.

Once the fields are filtered, POD modes and time projections can be computed as it has been done with the original snapshots. In Fig. 3.6 the energy contribution of the first 20 modes shows how the first two modes increased their importance on the total kinetic energy.

The first 4 modes $\Phi_n^u(x,y)$ and $\Phi_n^v(x,y)$, excluding the 3^{rd}, can be computed with the same procedure as described in the previous section. Modes shown in Fig. 3.7 reveal the consequence of time filtering. We can observe that the first two modes are not affected

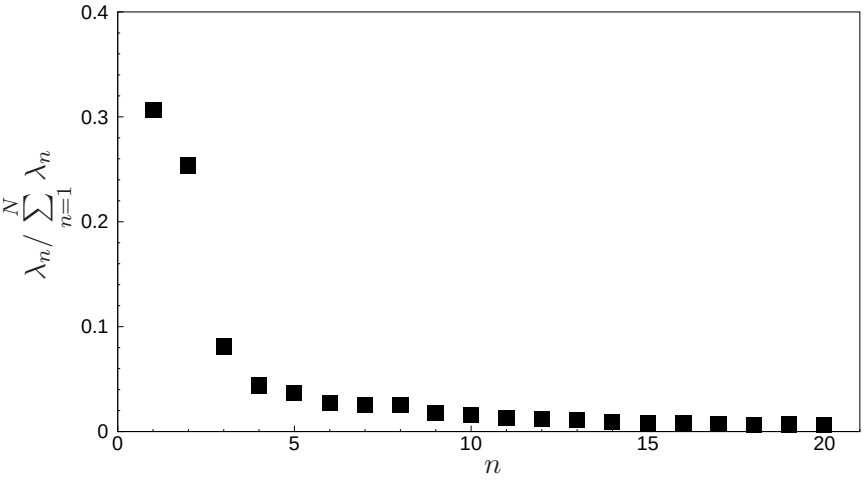

Figure 3.6: Contribution of the first 20 eigenvalues computed from the correlation term corresponding to a set of N_s =500 snapshot acquired at 3 kHz with a flow at 34 m/s and filtered with a Fourier filter abouve 150 Hz.

by the FFT, since they are related to the main oscillating motion. This is not a trivial result since solving the eigenvalue problem implies the use of a non-linear procedure as the singular value decomposition. A different matter is the effect on the 4^{th} and 5^{th} mode. In these cases the filter produces a relevant modification in the spatial distribution related to the oscillating smallest eddies. The result is clearly not physical and the loss of information is huge. This leads to consider for model reduction only the first two modes, related to the resonance at $126Hz$. This choice reduces the dynamics represented by the model close to those of a classic harmonic oscillator.

In Fig. 3.8 filtered trajectories, obtained by projection of the filtered snapshots onto the first two modes, are shown. By comparison with the corresponding trajectories in Fig. 3.4, the shape is much more regular in the filtered case. However, projections are still strongly modulated, confirming the presence of several frequencies around the characteristic peak, but the high frequency noise is avoided everywhere. On the original time projections (those obtained from the original set of snapshots) the same Fourier filter has been applied and results are compared in the same figure. We can note that computing time projections from filtered fields and directly filter trajectories obtained with the original snapshots, produce the same result. In fact, red and black lines, representing filtered trajectories and projections from filtered fields respectively, superpose perfectly, confirming that the FFT at $150Hz$ does not affect the oscillating motion at $126Hz$.

A final remark can be done on the use of the FFT. The Fourier filter acts directly on the spectra, without introducing any delays. The objective of this procedure was to highlight the main dynamics in order to obtain a model representing a bigger amount of energy. If image-filtering was a productive path in this sense, we can implement a real

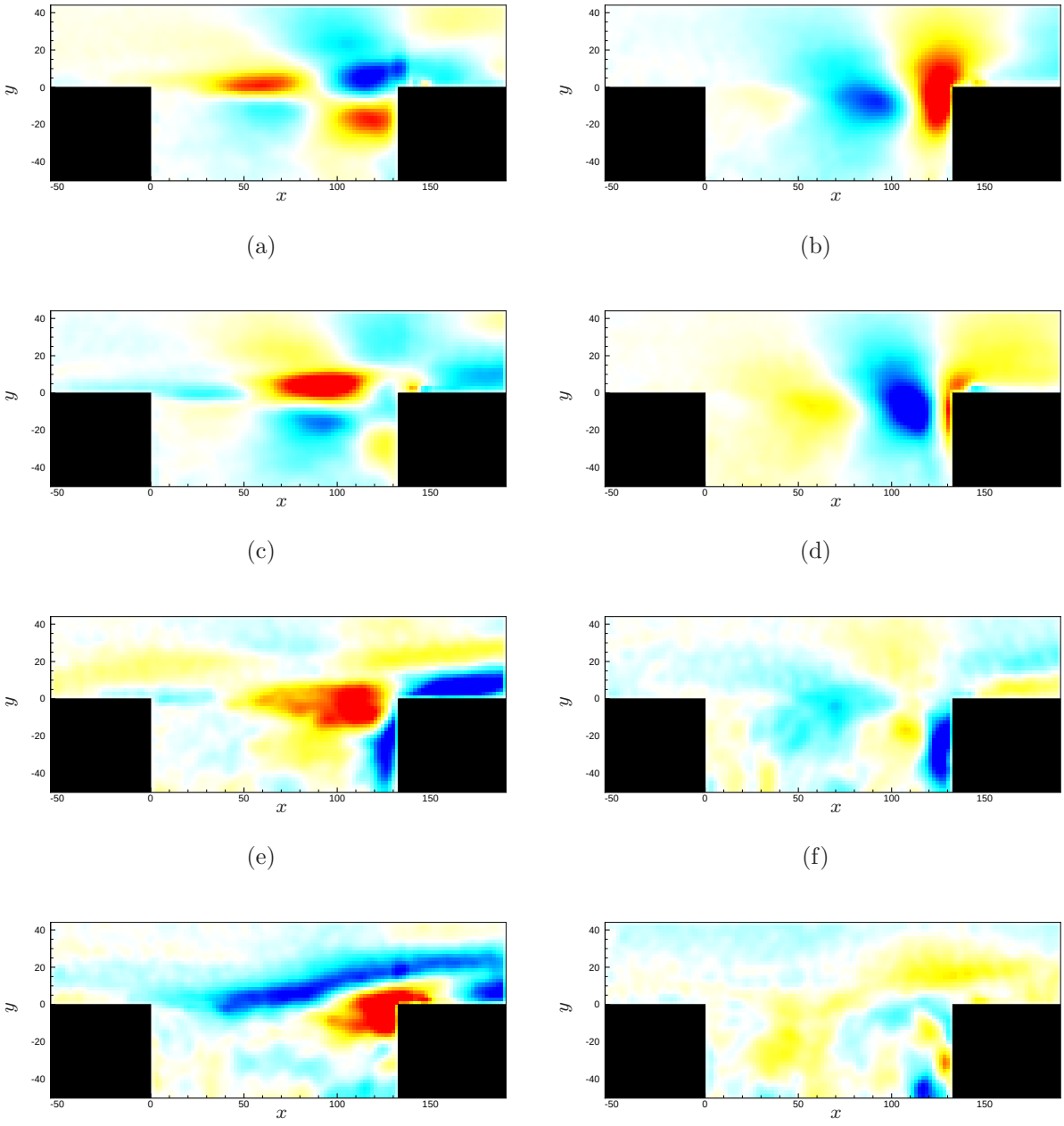

(a) (b)

(c) (d)

(e) (f)

(g) (h)

Figure 3.7: First 4 POD modes computed from 500 snapshot acquired at 3 kHz with a flow at 34 m/s and filtered with a Fourier filter above 150 Hz. (a) Φ_1^u, (b) Φ_1^v, (c) Φ_2^u, (d) Φ_2^v, (e) Φ_4^u, (f) Φ_4^v, (g) Φ_5^u, (h) Φ_5^v. Levels are from -0.035 to 0.035.

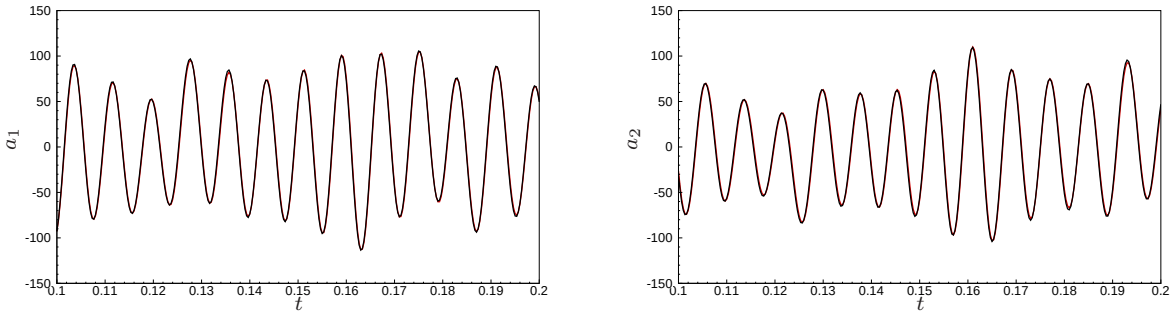

(a) (b)

Figure 3.8: Comparison of the time projections corresponding to the first 2 POD modes computed from snapshots acquired at $3kHz$ at a velocity of 34 m/s and filtered with a Fourier filter above 150 Hz. Red lines represent the filtered trajectories obtained from the original velocity fields; black lines represent trajectories from the filtered snapshots.

filter introducing a delay to deal with. We then consider only for this study the Fourier filter an easier way to accomplish this purpose.

3.2.3 Summary

Dealing with experimental results implies the presence of high frequency noise and a high energetic level related to the smallest eddies. In this section, we proposed a model reduction based on an energetic criterion. To this aim we computed POD modes and time projections from TR-PIV snapshots. Features related to the high frequency content have been detected in the observation of trajectories as well as a high energetic contribution of the smallest eddies. Since the reduced-order model is not capable to represent high frequency dynamics, an approach based on time filtering has been proposed. Results have shown that time filtering helps the selection of the most energetic modes, focusing on the low frequency dynamics related to the main oscillating motion. This is considered as a novel approach in post-processing of PIV measurements.

3.3 NLARX model structure and identification of the free dynamics

The Non-Linear Auto-Regressive eXogenous (NLARX) model identification is analyzed in more detail. Here, the key role of every parameter and the problem of the regularization, are described. After a sensitivity analysis, the model obtained is identified on a learning dataset and validated on a different set of data. We show the difference between a single time-step prediction and a long-period simulation and how, in this second case, the model may reveal its instability. Results presented in the following are obtained after a

parametric analysis on the whole set of parameters present in the identification procedure.

3.3.1 Model description

The NLARX model is obtained in two steps: a learning phase and a testing phase. In the learning phase a small number of periods is used to identify the non-linear model coefficients modulating regressors $a_n(t-i)$ and their non-linear combinations. The coefficients of the model are computed in order to fit as best as possible the original data. In the following validation phase, these are kept constant and the dynamics are computed and compared with a different set of data. This second phase can be done with two different approaches, simulation or prediction. The simulation consists in integrating the resulting model up to a given finite time knowing only the initial state, while the second approach only assesses the quality of the prediction over one time step (this is more limiting test since the initial state is provided at every time step).

The NLARX model is as a non-linear combination of the various time projections $a_n(t)$. It depends on a number of different parameters: the number of modes used, the order of the algorithm, i.e. the number of non-linear terms, and time delay, corresponding to the number of previous regressors considered. For the trajectory related to the first mode $a_1(t)$, the prediction algorithm can be written as:

$$a_1(t) = \theta_0 + \sum_{i=1}^{N}\sum_{n=1}^{n_d} A_{in}a_i(t-n) + \sum_{j=1}^{N}\sum_{i=1}^{N}\sum_{n=1}^{n_d} B_{ijn}a_i(t-n)a_j(t-n) + \sum_{k=1}^{N}\sum_{j=1}^{N}\sum_{i=1}^{N}\sum_{n=1}^{n_d} C_{ijkn}a_i(t-n)a_j(t-n)a_k(t-n), \quad (3.7)$$

where N corresponds to the number of modes used, n_d is the time delay, and θ_0, A_{in}, B_{ijn} and C_{ijkn} are the coefficients to be identified. Note that the algorithm structure in Eq. (3.7) differs from that obtained from Galerkin projection in Eq. (3.6) for the third order term. This term has been added to the algorithm formulation since it leads to better results. A third order term can be found in the Stuart-Landau amplitude equation used in the stability analysis of a cavity flow by Sipp and Lebedev (2007).

In a more compact form, considering the whole time history of n_t time steps and all the time projections N, Eq. (3.7) can be rewritten as:

$$\mathrm{Y} = \mathrm{Q} \cdot \mathrm{R}, \quad (3.8)$$

where Y is the $N \times (n_t - n_d)$ matrix containing the predicted trajectories, Q is a $N \times (9 \times n_d + 1)$ coefficients matrix and R is the regressors matrix containing all the non-linear combinations of the previous time projections and has dimension $(19 \times n_d + 1) \times (n_t - n_d)$.

3.3.2 Model learning

In the learning phase the coefficients matrix Q is computed through a least-square algorithm from Eq. (3.8):

$$\mathrm{Q} = \mathrm{Y}\mathrm{R}^* \left(\mathrm{R}\mathrm{R}^*\right)^{-1}. \tag{3.9}$$

The solution of this problem may not easily be solved because of the dimensions of the problem and because of the nearly singular matrix $\mathrm{R}\mathrm{R}^*$.

The dimension of the problem depends on the number of regressors n_t chosen to reconstruct previous time history, time delay n_d, the order of the model and the number of modes N. The combination of these parameters can increase the problem dimension, but since the number of modes and the number of previous points are kept small, dimension is a manageable problem.

An ill-posed problem can be a more bothersome issue. In the least-square method the inversion of the matrix $\mathrm{R}\mathrm{R}^*$ is needed and a poor conditioning can affect the final result. In order to avoid this problem, the Tikhonov regularization is adopted. It consists in including the Tikhonov matrix Γ in the least-square problem and regulate ill-conditioning through a factor α:

$$\mathrm{Q} = \mathrm{Y}\mathrm{R}^* \left(\mathrm{R}\mathrm{R}^* + \alpha\Gamma\Gamma^*\right)^{-1}. \tag{3.10}$$

In this case, the Tikhonov matrix has been chosen as the identity matrix while α is tuned from 0 (no need of regularization) up to 2 for more complex cases.

Single time-step simulation

In Fig. 3.9, the model identified is compared to the learning data set. The model used is a full third-order model, computed on a data set of $n_t = 300$ elements, with a delay $n_d = 4$ and based on 2 filtered modes, obtained in the previous section. The model reproduces the original data accurately, with a fit of 99.8% for both trajectories. This result is expected since the solution of the least-square problem is optimal to fit known data on a single time-step. Considering only two coupled modes, filtered and representing the most important contribution to total energy, has the evident consequence of a perfect fit. A less trivial, but also less efficient, result can be obtained by considering non-filtered modes.

Long-period prediction

The model obtained from Eq. (3.10) fits the learning data-set with a negligible error if we perform a single time-step simulation. A robust model should reproduce the set of data on which it has been computed even if integrated in a long-period prediction. In Fig. 3.10 the comparison between the predicted trajectories (red lines) and the original ones

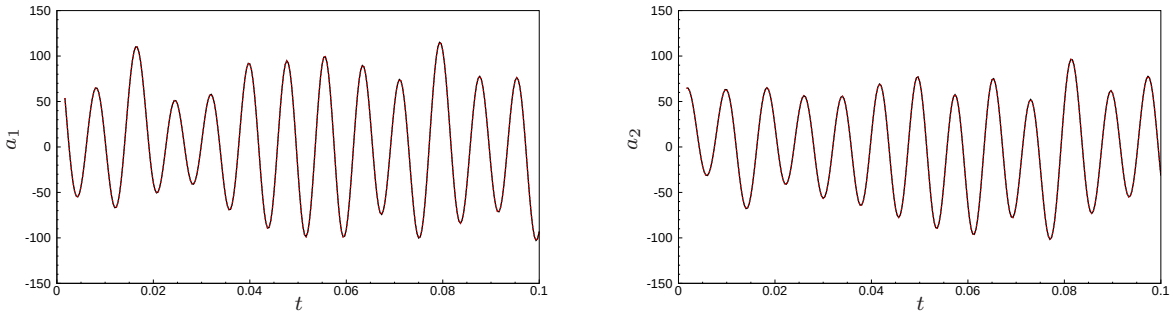

(a) (b)

Figure 3.9: Model fitting from the learning data set of the first 2 time projections. Black lines represent the original data, red lines represent the model.

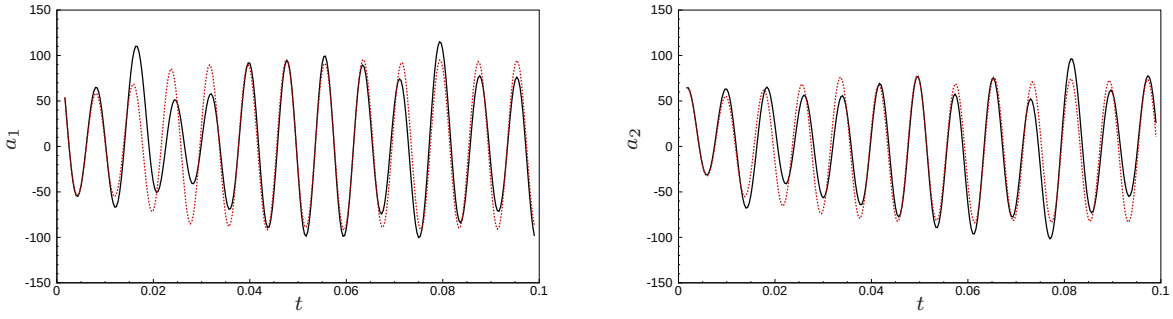

(a) (b)

Figure 3.10: Model fitting from the learning data set of the first 2 time projections, considering a long-period prediction. Black lines represent the original data, red lines represent the model.

(black lines) shows the true behavior of the identified model. The fitting is decreased to 63.5% for a_1 and 67.5% for a_2, evincing a poor robustness of the non-linear model. In particular, although the frequency behavior is well captured, the model fails to reproduce the non-linearity and stabilizes to a fixed-amplitude oscillation.

These results are obtained after a parametric analysis on the whole set of parameters and represent the best compromise among them. However, the long-time prediction poor fitting is not encouraging for our purpose, since the non-linearity still represents a great issue to deal with.

3.3.3 Model validation

The model found in the learning phase has to be validated on a different data set. This procedure can be done, even in this phase, with two different approaches: a single time-step simulation or a long-period prediction. Results shown in the following confirm considerations about robustness sorted out in the learning phase.

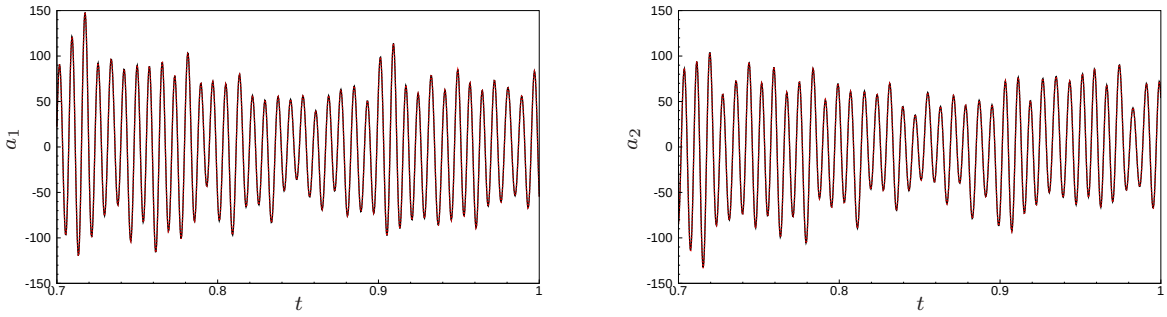

(a) (b)

Figure 3.11: Model fitting from the testing data set of the first 2 time projections. The model is obtained with a single time-step simulation. Black lines represent the original data, red lines represent the model.

Single time-step simulation

The simulation approach consists in keeping the coefficients matrix Q constant and compute the new state by knowing the previous at each time step. This method assumes that the correct state is available and it cannot be considered realistic. However, it is interesting to observe the behavior of the model on a different set of data.

In Fig. 3.11 the model is validated with a single time-step simulation on the first 2 trajectories. The model reproduces the dynamics with no significant errors. The fit obtained is in fact 99.7% on the first mode and 99.6% on the second.

Long-period prediction

The long-period prediction can be considered as the definitive test of the model. In the prediction phase only the initial state is known and the model predicts the new state as a function of data previously estimated. This time integration reproduces what happens in a real application since the state is not known at every time step.

As we can observe in Fig. 3.12, the model fails to reproduce the dynamics of the time projections, with only a poor fit of 18.0% and 16.0% for the two modes. This result cannot be improved by changing model parameters and this limit has to be related to the presence of the non-linearity. In fact, by observing the predicted trajectory, the oscillating behavior is well represented in frequency, as in the learning phase. Despite this, non-linear behavior is not reproduced, even though the oscillation is stable.

3.3.4 Critical analysis

A non-linear model reproducing at least the most important oscillating motions has been identified. Because of the simplicity of the model, due to the choice of reducing the number

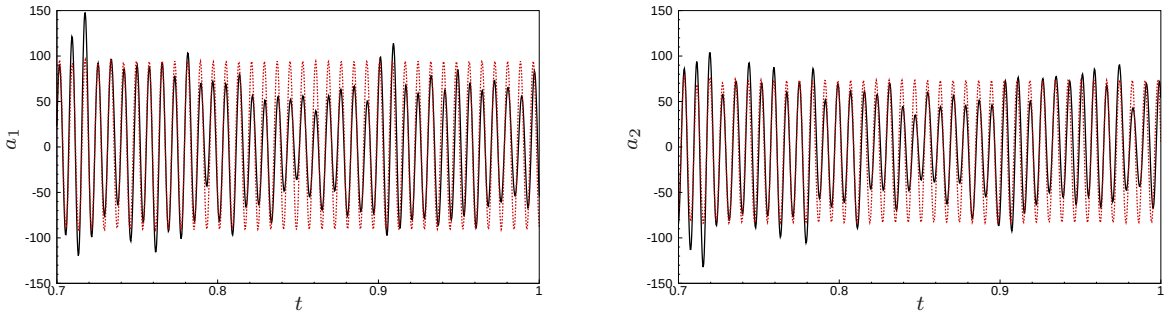

(a) (b)

Figure 3.12: Model fitting from the testing data set of the first 2 time projections. The model is obtained with a long-period prediction. Black lines represent the original data, red lines represent the model.

of modes to only the first two, the oscillation characteristic frequency is well reproduced and even after long-period integration the trajectory prediction does not blow up. On the other hand, capturing non-linearities is still a hard challenge. This is a strong limitation since every choice was made to reduce any other influence and keep only non-linearity as challenging point. This result has a definitive impact on future choices on closed-loop control strategies applied to our configuration.

Despite this consideration, in order to find the best strategy to identify the non-linear model, all parameters have been analyzed. The effect of each parameter can be summarized as follows.

Model order. Non-linear terms, as quadratic and cubic terms, are present in the model. Their presence is justified by the Navier-Stokes equations and the Stuart-Landau model. The influence on the model is an increased fit in both phases, learning and validation. However, the model is more complex and consequently more sensitive to any other change of parameters and this can affect the time integration leading the model to blow up.

Number of modes. The number of trajectories used increases the number of variables to be identified. This does not affect the learning phase, but the long-period prediction, because more non-linearities are introduced into the model.

Time delay. The number of known time instants are not necessarily useful to improve the model. On the contrary, because of the non-linear nature of the cavity flow and consequently of the time trajectories, the model is forced to follow a path that is not repeatable. Increasing n_d more than 2 immediately causes a violent blowing-up of the predicted model.

The system identification technique, analyzed in this chapter, revealed a great potential for flow-control applications. The possibility of obtaining a reduced-order model directly from observable dynamics is still an undeniable advantage with respect to a model obtained from Galerkin projection. However, non-linearity represents a huge limitation

to this approach. It has been demonstrated that a non-linear model has a poor behavior in predicting dynamics in a long term. In addition, the model is strongly dependent on the parameters used to tune the coefficients computation, implying a bad robustness of this technique.

Chapter 4

Robust feedback control of a cavity flow

This chapter describes a strategy to obtain a more robust control based on a reduced model from Petrov-Galerkin projection of linearized Navier-Stokes equation onto unstable global modes and stable balanced POD modes. Results are gathered from numerical simulations of a laminar flow over a squared cavity, the same case analyzed by Sipp and Lebedev (2007) and Barbagallo et al. (2009).

System identification has been analyzed in the previous chapter as a valid approach to obtain a reduced model that can be easily used to develop a control technique to control oscillating flows in real applications. However, it has been shown how this technique is strongly limited by non-linear behavior of the cavity flow examined and is not robust to changes of the set of parameters considered in the identification process. These drawbacks led us to consider other strategies to develop a control technique with good perspective in real applications. The most promising is to increase control robustness to external perturbations.

The need of robust control begun with the necessity of compensate for the limitations of the Linear Quadratic Gaussian (LQG) control when applied far from the design conditions. The lack of robustness to external disturbances is remarked when a Linear Quadratic Regulator (LQR) is coupled with a Kalman filter that estimates the state. Optimal control theory and its limitations is explained in a number of references as Burl (1998).

In order to increase robustness in linear control, two strategies have been undertaken: Loop-Transfer Recovery (LTR) and robust control based on $\mathcal{H}_\infty$ norm to define the cost function. The first technique has been introduced by Moore et al. (1981) and it consists in introducing a colored fictitious noise to the system. Robust $\mathcal{H}_\infty$ control technique, from Doyle et al. (1989), has been applied to flow control by Bewley and Liu (1998), showing good results in increasing robustness by defining the cost function as a min-max problem, i.e. designing the controller that minimizes the cost considering the worst disturbance.

These two techniques are considered as references to develop a strategy that consider robustness directly into the definition of the cost function

The chapter is structured as follows: cavity flow is defined in Sec. 4.1 as well as linearized governing equations. The cavity problem is completed by actuator and sensor definition. In Sec. 4.2 the procedure to obtain a reduced-order model is described. In particular, we focused on a basis composed by global modes for the unstable subspace and balance POD modes for the stable subspace. The closed-loop system is defined in Sec. 4.3, through the definition of the closed-loop transfer function and perturbations. The key role of this study is played by the definition of performances and robustness in Sec. 4.4. Along with classical robustness from Nyquist theorem, a model based on unstructured uncertainties is proposed. Results from classic control design, i.e. LQG, LTR and $\mathcal{H}_\infty$ control, are shown in Sec. 4.5 while robust control results obtained with the strategy proposed in this study are proposed in Sec. 4.6. A final consideration on unstable perturbations, as changes in Reynolds number, and the possibility of suppress such disturbances, are analyzed in Sec. 4.7.

4.1 Flow configuration, governing equations and setup

4.1.1 Flow configuration

We consider a two-dimensional open square cavity, which has the same geometry and boundary conditions as that described in Sipp and Lebedev (2007). The reference quantities used to non-dimensionalize the governing equations are the uniform flow velocity U_∞, the cavity depth D, thus the Reynolds number is defined as $Re = U_\infty D/\nu$, where ν is the viscosity. The origin of the coordinate system is set at the upstream corner of the cavity, so that the downstream edge is at $(x = 1, y = 0)$. On the boundaries, conditions are set as follows: uniform unitary flow at the inlet boundary (x=-1.2), free-slip condition on the upper boundary ($y = 0.5$) and on the boundaries ($-1.2 \leq x < -0.4, y = 0$) and ($1.75 < x \geq 2.5$), while from the starting point of the laminar boundary layer at $(x = -0.4, y = 0)$ the no-slip condition is prescribed, together with cavity walls and the downstream wall until $(x = 1.75, y = 0)$. The mesh used is composed by 194771 triangles, corresponding to 880495 degrees of freedom for the three variables (u, v, p).

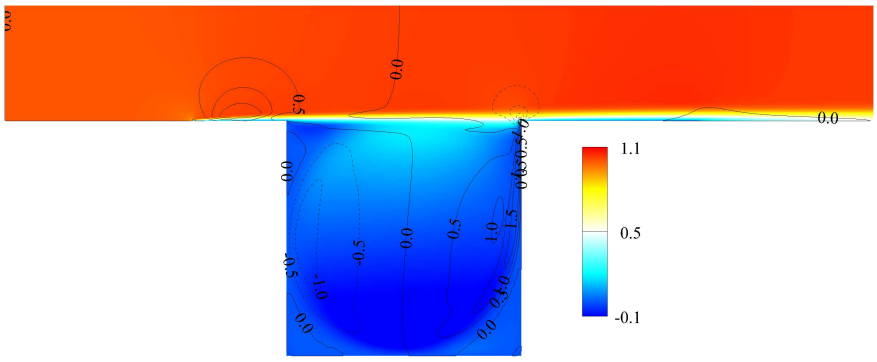

Figure 4.1: The contour plot corresponds to the streamwise component of the base flow, u_0 obtained at $Re = 7500$, while the spatial profile of the control input $u(t)$ is represented by the isolines.

4.1.2 Governing equations

The full non-dimensionalized non-linear governing equations are written for the velocity field $\mathrm{u} = (u, v)$ and the pressure p.

$$\frac{\partial \mathrm{u}}{\partial t} + (\mathrm{u} \cdot \nabla)\,\mathrm{u} = -\nabla p + \frac{1}{Re}\Delta \mathrm{u}, \tag{4.1a}$$

$$\nabla \cdot \mathrm{u} = 0. \tag{4.1b}$$

Before proceeding with linear control design, the flow has to be linearized around a steady solution, the base flow $\mathrm{u}_0(x, y) = (u_0, v_0)$. It is determined with a Newton-Raphson method, after setting to zero the unsteady term of the non-linear Navier-Stokes equations summarized in Eq. (4.1). The base flow in Fig. 4.1 displays a thin shear layer and a recirculating vortex in the cavity. The boundary layer starting at $(x = -0.4, y = 0)$ is also visible.

Once the steady solution is computed, the flow can be decomposed into base flow and unsteady perturbations $\mathrm{u}'(x, y, t) = (u', v')$, so that $\mathrm{u} = \mathrm{u}_0 + \mathrm{u}'$ and $p = p_0 + p'$. By substituting the expression for u and p into Eq. (4.1) and the base flow being a steady solution of the Navier-Stokes equations, we obtain the perturbative form of the governing equations:

$$\frac{\partial \mathrm{u}'}{\partial t} + (\mathrm{u}' \cdot \nabla)\,\mathrm{u}_0 + (\mathrm{u}_0 \cdot \nabla)\,\mathrm{u}' + (\mathrm{u}' \cdot \nabla)\,\mathrm{u}' = -\nabla p' + \frac{1}{Re}\Delta \mathrm{u}', \tag{4.2a}$$

$$\nabla \cdot \mathrm{u}' = 0. \tag{4.2b}$$

The evolution of the perturbations $\mathrm{u}' = (u', v')$ and p', obtained by linearization of the non-dimensionalized two-dimensional Navier-Stokes equations around the base flow

u_0, reads as follows:

$$\frac{\partial \mathrm{u}'}{\partial t} + (\mathrm{u}' \cdot \nabla)\,\mathrm{u}_0 + (\mathrm{u}_0 \cdot \nabla)\,\mathrm{u}' = -\nabla p' + \frac{1}{Re}\Delta \mathrm{u}', \tag{4.3a}$$

$$\nabla \cdot \mathrm{u}' = 0, \tag{4.3b}$$

or in compact form:

$$\mathscr{Q}\frac{\mathrm{d}\mathscr{X}}{\mathrm{d}t} = \mathscr{A}\,\mathscr{X}, \tag{4.4}$$

where $\mathscr{Q}$ is the identity matrix selecting only the velocity components, $\mathscr{X} = (\mathscr{U}, \mathscr{V}, \mathscr{P})$ is the state vector composed by the perturbations of the two velocity components and the pressure field, and $\mathscr{A}$ is the linearized Navier-Stokes operator. The spatial discretization is finally obtained through a mesh of unstructured (P2,P2,P1) finite elements. The final form of the discretized governing equations is:

$$\mathrm{Q}\frac{\mathrm{dX}}{\mathrm{d}t} = \mathrm{AX}. \tag{4.5}$$

4.1.3 Actuator and sensor definition

The control input considered is a blowing and suction actuator, added to the system (4.4) through a modification of the boundary condition over a section of the wall near the upstream edge of the cavity, as shown by the isolines in Fig. 4.1. The spatial profile $\mathscr{B}_2$ is the solution of the steady inhomogeneous problem due to the modification of the boundary condition, so that:

$$\mathscr{Q}\frac{\mathrm{d}\mathscr{X}}{\mathrm{d}t} = \mathscr{A}\,\mathscr{X} + \mathscr{Q}\mathscr{B}_2\tilde{u}(t), \tag{4.6}$$

We also introduce the measurement of the boundary layer near the downstream edge of the cavity:

$$\tilde{m}(t) = \int_{x=1}^{x=1.1} \left.\frac{\partial u}{\partial y}\right|_{y=0} \mathrm{d}x = \mathscr{C}_2\mathscr{X}. \tag{4.7}$$

In the SISO system we also introduce a noise to the control input, $w(t)$, and to the measurement, $g(t)$. The state noise w is therefore spatially introduced into the system by B_2 since it is related to the control input, i.e. a noise introduced directly by the actuator. The measurement noise g is always present in every practical application and it is simply added to the measurement. The state-space formulation of the flow control problem,

avoiding time dependency for an easier reading, finally reads as:

$$Q\frac{\mathrm{dX}}{\mathrm{d}t} = \mathrm{AX} + Q\mathrm{B}_2 u + Q\mathrm{B}_2 w, \tag{4.8a}$$

$$m = \mathrm{C}_2\mathrm{X} + g, \tag{4.8b}$$

where the matrix C_2 extracts the shear of the boundary layer from the state vector X. More details on noises and how they affect control design will be given in Sec. 4.3.1.

4.2 Model reduction

Because of the high number of degrees of freedom required for the discretization adopted to solve the Navier-Stokes equations, the design of a compensator that stabilizes the problem defined in Eq. (4.8) is not easy. However, the compensator only needs the most important features of the dynamics between the sensor and the actuator. For this reason, a reduced-order model is required. In addition, we also consider that for a real-time control, the compensator should be as fast as possible with respect to the flow dynamics, so it needs to be based on a reduce-order model.

In order to obtain a reduced-order model, it is common to use a projection technique or a system identification technique. We already spoke about the latter in Chapter 3, where this technique is based on an auto-regressive non-linear model, learned from experimental results. Here we focus on a Petrov-Galerkin projection technique since the objective of this part of the study is to obtain a method that increases robustness and a more classical technique for the reduced-order model is sufficient.

In model reduction procedure, the objective is to find a matrix V, called the reduced basis, such that the state vector X can be decomposed as:

$$\mathrm{X} = V\hat{\mathrm{X}},$$

where the upper symbol $(\hat{\bullet})$ represents a reduced quantity. With a second basis W that satisfies the bi-orthogonality condition with V, such that $W^*QV = I$, the reduced state vector is then:

$$\hat{\mathrm{X}} = W^*Q\mathrm{X},$$

so that the resulting system in the state-space form, can be rewritten as:

$$\frac{\mathrm{d}\hat{\mathrm{X}}}{\mathrm{d}t} = \hat{\mathrm{A}}\hat{\mathrm{X}} + \hat{\mathrm{B}}_2 u + \hat{\mathrm{B}}_2 w, \tag{4.9a}$$

$$m = \hat{\mathrm{C}}_2\hat{\mathrm{X}} + g, \tag{4.9b}$$

where the reduced matrix are computed as:

$$\hat{\mathrm{A}} = W^*\mathrm{A}V, \qquad \hat{\mathrm{B}}_2 = W^*Q\mathrm{B}_2, \qquad \hat{\mathrm{C}}_2 = \mathrm{C}_2V.$$

The choice of the reduced basis is critical for good performances. Since the objective is to stabilize an unstable flow, unstable global modes must be included in the reduction basis. The action of the controller, however, also triggers some stable states; for this reason, it is necessary to include in the reduction basis a stable subspace, which can be treated separately from the unstable problem, due to the choice of using global modes. The choice of the stable basis is not trivial: a solution deeply analyzed by Barbagallo et al. (2009) is to use a model truncation based on Balanced POD (BPOD) modes obtained with the *Snapshot method* introduced by Rowley (2005). In the following we discuss in more detail global modes and BPOD modes.

4.2.1 Global modes

Global modes are used as a projection basis in order to obtain a reduced-order model of the unstable subspace. These modes are the eigenvectors of the linearized Navier-Stokes operator and they represent the spatial structures related to the eigenvalues. From the system described in Eq. (4.5) global modes can be computed by assuming an exponential time-dependence for the state vector $\mathrm{X}(x,y,t) = \tilde{\mathrm{X}}(x,y)\mathrm{e}^{\lambda t}$, with $\lambda \in \mathbb{C}$, leading to the eigenvalue problem:

$$\lambda \mathrm{Q}\tilde{\mathrm{X}} = \mathrm{A}\tilde{\mathrm{X}}, \tag{4.10}$$

that can be solved using Arnoldi methods based on a shift-invert strategy and a sparse direct LU solver (MUMPS (Amestoy et al., 2001)) to handle the matrix inverses. The eigenvalues are complex $\lambda = \sigma + \mathrm{i}\omega$, where σ and ω correspond to the amplification rate and frequency of the modes. The basis obtained is non-orthogonal since global modes do not satisfy this property. An adjoint basis is therefore required to project along the directions of the global modes; it is obtained by computing the eigenvalues of the adjoint linearized Navier-Stokes operator. As in Barbagallo et al. (2009), we compute only the unstable global modes, since they are used only to represent the unstable subspace. In this study, we consider four different unstable cases: the first two ($Re = 5500$ and 6500) have three unstable modes, while the third (7500) and the fourth (8000) present a fourth weak instability, as shown in Fig. 4.2.

As an example, in Fig. 4.3, we have represented some global modes computed at Reynolds 7500. It is seen that the number of structures in the shear-layer increases, as expected, with the frequency of the modes. These global modes have already been described by Barbagallo et al. (2009). Finally, in Fig. 4.3(d), a typical adjoint structure which is, as expected, located at the left corner of the cavity because of the convective

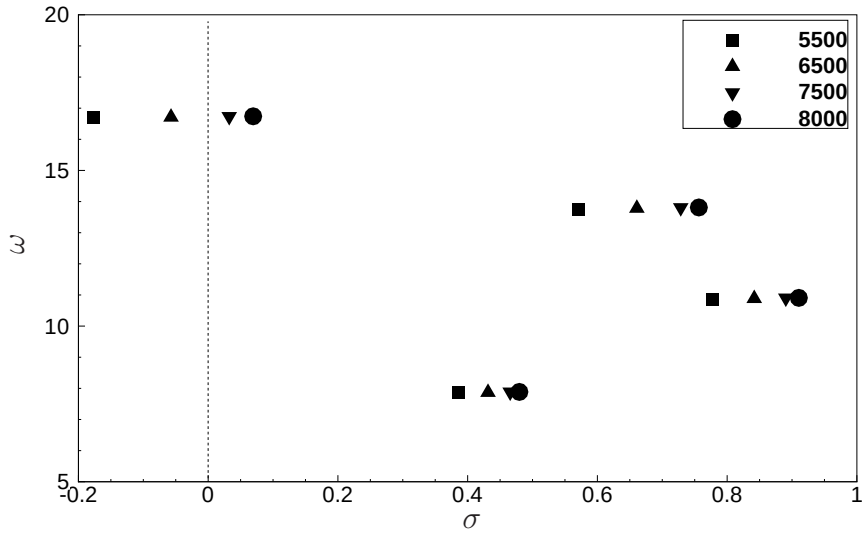

Figure 4.2: Least stable direct global modes at different Reynolds numbers.

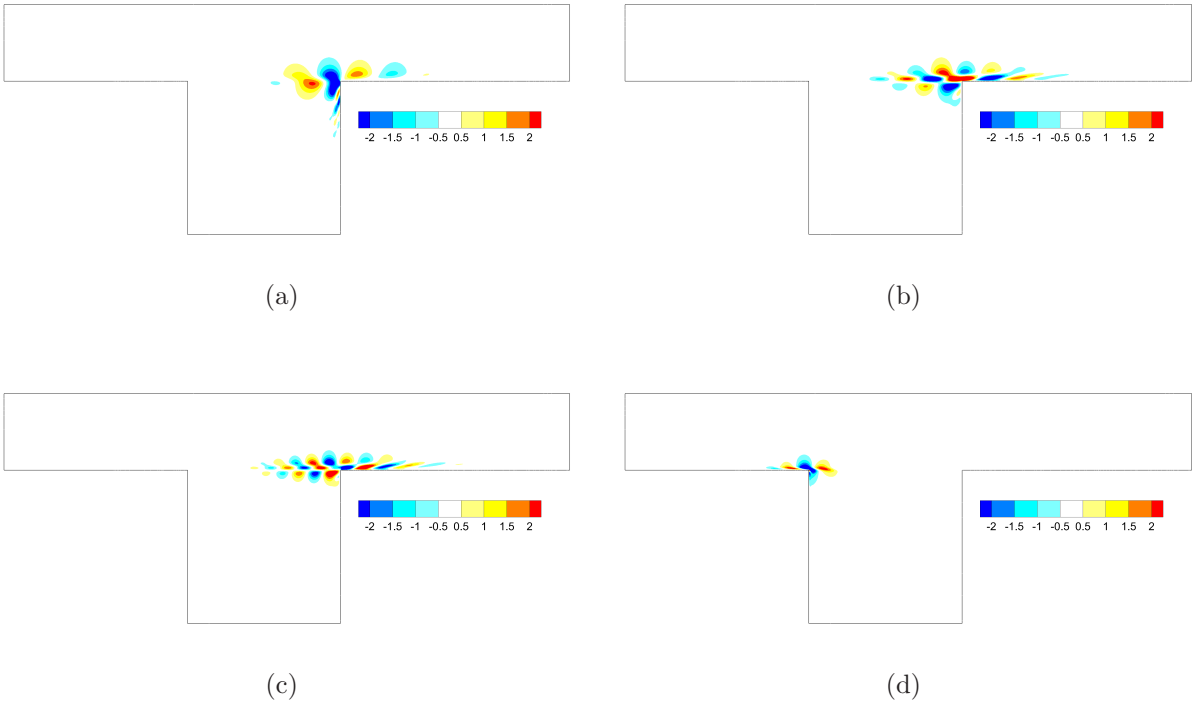

Figure 4.3: (a) cross-stream component of the direct global mode at $\omega = 7.9$; (b) streamwise component of the direct global mode at $\omega = 10.9$; (c) streamwise component of the direct global mode at $\omega = 16.7$; (d) cross-stream component of the adjoint global mode at $\omega = -13.8$.

non-normality.

4.2.2 Balanced POD modes

Considering the system described by 4.8, we would like that the stable subspace of the truncated model should be as controllable than observable. We therefore introduce the *Controllability Gramian* G_C and the *Observability Gramian* G_O. With X denoting a divergence-free flow field, the controllability gramian is related to the control energy through the relation $\int_0^\infty u^*(t)u(t) = \mathrm{X}^*\mathrm{G}_C^{-1}\mathrm{X}$, so it represents how much an input affects each state. On the other hand, the observability gramian is related to the measurement energy through $\int_0^\infty m^*(t)m(t) = \mathrm{X}^*\mathrm{G}_O\mathrm{X}$, indicating how much each state affects future outputs. A balanced truncation selects the structures that are most observable and controllable and therefore excludes states that are either weakly controllable or weakly observable.

To compute the Gramians, we have to perform linearized DNS simulations of impulse responses in the stable subspace of the system 4.8. First, to approximate G_C, we solve the direct problem initialized by the control state B_2:

$$Q\frac{\mathrm{dX}}{\mathrm{d}t} = \mathrm{A}_s\mathrm{X}, \tag{4.11a}$$

$$\mathrm{X}(0) = P_s\mathrm{B}_2. \tag{4.11b}$$

Then, to approximate G_O, we solve the adjoint problem initialized with the measurement state C_2^*:

$$Q\frac{\mathrm{dY}}{\mathrm{d}t} = \mathrm{A}_s^*\mathrm{Y}, \tag{4.12a}$$

$$\mathrm{Y}(0) = P_s^*\mathrm{C}_2^*. \tag{4.12b}$$

Every time step, all the solutions are projected onto the stable space, by the projection matrices P_s and P_s^*. The controllability Gramian can be now computed as:

$$\mathrm{G}_C = \mathrm{X}\mathrm{X}^*, \tag{4.13}$$

while the observability Gramian is:

$$\mathrm{G}_O = \mathrm{Y}\mathrm{Y}^*. \tag{4.14}$$

The balanced truncation is then computed by performing a Singular Value Decomposition (SVD) of the matrix $\mathrm{Y}^*\mathrm{X} = U\Sigma V^*$, and using, as a reduction basis, the matrix T and S,

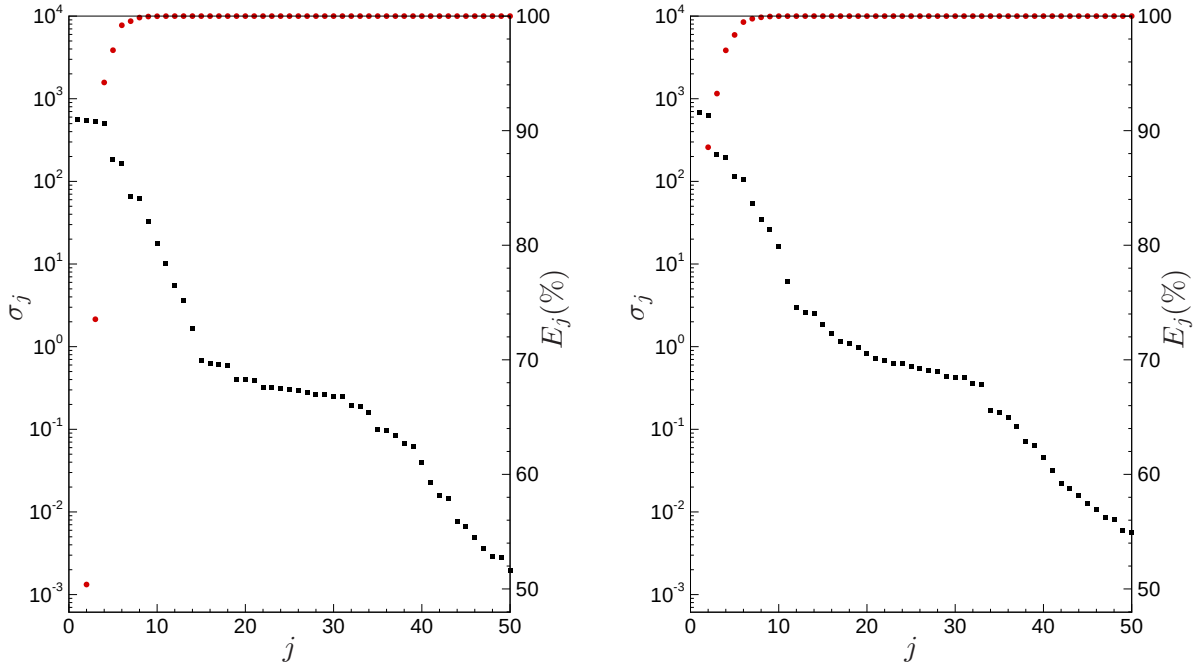

Figure 4.4: Hankel singular values σ_j for Reynolds (a) 5500 and (b) 7500.

obtained as:

$$T = \mathrm{X}V\Sigma^{-1/2}, \qquad S = \mathrm{Y}U\Sigma^{-1/2},$$

that represent the Balanced POD modes and their dual modes. The number of BPOD modes, i.e. the dimension of T and S, to consider in order to capture the most important dynamics, are chosen from the fall-off of the Hankel singular values Σ_i. In figure 4.4 are shown the Hankel singular values for two different Reynolds numbers, 5500 and 7500. From the approximation criterion, based on the $\mathcal{H}_\infty$-error norm of the open-loop transfer function and defined in Barbagallo et al. (2009), we know that, for the present case of cavity flow, a few balanced modes (10 at least) are sufficient to reproduce the exact dynamic with a relative error lower than 1%.

In our study we consider 14 BPOD modes for $Re = 5500$ and 6500, and 12 BPOD modes for 7500 and 8000, in order to have a reduced model of dimension 20×20. In Fig. 4.5 the comparison of the impulse response of the actual system projected on the stable subspace from a DNS and the stable part of the reduced model obtained with a BPOD basis, shows how perfectly the reduced model represents the actual stable subsystem. In Fig. 4.5(a) is represented the time response, while in Fig. 4.5(b) is shown the amplitude of the open-loop transfer function of the stable subspace from the input $u(t)$ to the measurement $m(t)$, computed as Fourier transforms of the impulse responses shown in Fig. 4.5. We show both graphics in order to introduce the frequency domain as the frequency

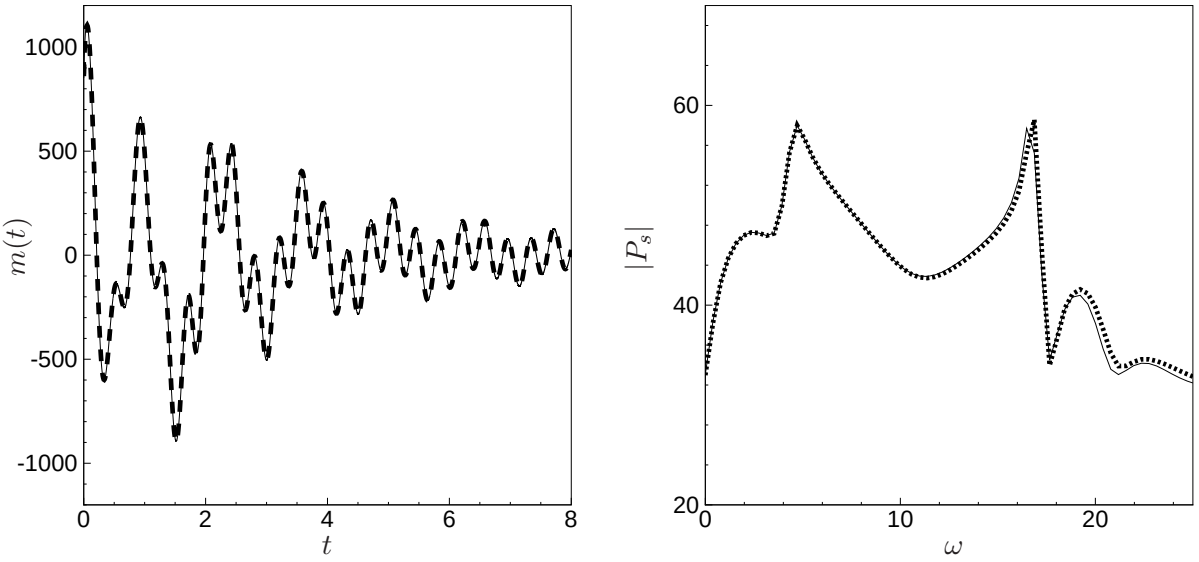

(a) (b)

Figure 4.5: Impulse response of the stable system at Reynolds 5500. (a) Time behavior of the measurement $m(t)$. (b) Open-loop transfer function amplitude in dB over a range of frequencies expressed in rad/s. Thick dashed line corresponds to the DNS; thin solid line corresponds to the reduced model based on BPOD.

domain will be favored in the rest of this study.

4.2.3 Summary

In order to design a compensator from a high-dimensional problem, a reduced-order model, representing the input/output dynamics, is required. Since the flow must be stabilized, unstable global modes are considered as a subspace of the model basis. The need of including stable modes to the reduced-order model, led us to consider balanced POD modes. In this section we have shown that only a few of these modes are capable to reproduce input/output dynamics with a negligible error, since they are based on controllability and observability properties of the system, and can be easily used as reduction basis.

4.3 Closed-loop system

The closed-loop system stability and its behavior to stable perturbations represent the principles leading the compensator design. The main features related to the closed-loop system, namely the closed-loop transfer function and the closed-loop perturbations, are defined in the following.

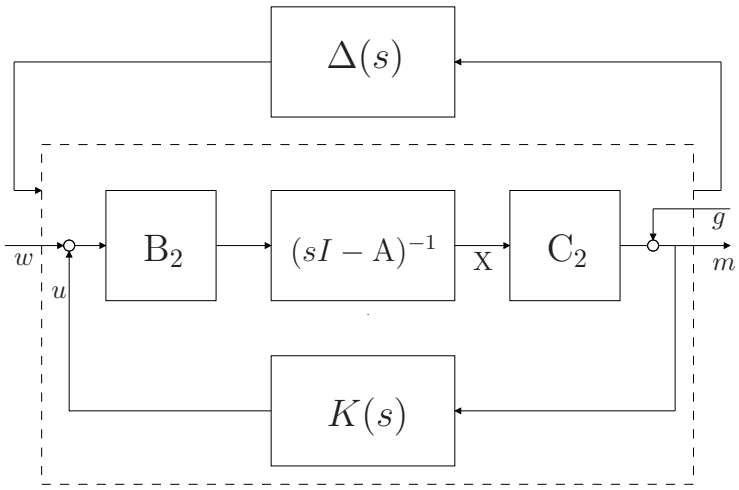

Figure 4.6: Closed-loop perturbed system. The closed-loop system composed by the plant and the compensator is enclosed in the dashed box. Noises w and g are the system inputs, while m is the measurement output. The perturbation $\Delta(s)$ represents all possible disturbances to the closed-loop system.

4.3.1 Closed-loop transfer function

The system described by Eq. (4.9) represents the plant with state and measurement disturbances added. The related open-loop transfer function is written with a Laplace transform as:

$$P(s) = \mathrm{C}_2 \left(sI - \mathrm{A}\right)^{-1} \mathrm{B}_2. \tag{4.15}$$

Since the cavity flow is unstable, the objective of this study is the design of a compensator that stabilizes the plant. We add to the system a compensator that closes the loop between the measurement and the control input as represented in the block diagram of Fig. 4.6. The compensator estimates the state, provides a control gain matrix and can be designed with any control strategy. It acts only on the control input u, providing a feedback law from the measurement m and it is represented by the transfer function $K(s)$. Note that here we do not define the compensator transfer function $K(s)$, since it depends on the control design and is specific for each strategy.

Once the loop is closed, the resulting system has to be stable, i.e. the closed-loop transfer function must not have poles with real part in the right half-plane. We then consider, as an example, the transfer functions representing the dynamics between the measurement m and the noise g:

$$T^{cl}_{mg}(s) = \frac{P(s)K(s)}{1 - P(s)K(s)}. \tag{4.16}$$

It can be shown that the poles of the numerator are canceled by those of the denominator, so the only possible instabilities reside in the zeros of the denominator. The condition

imposed in the compensator design is then that all the solutions of $1 - P(s)K(s) = 0$ have negative real part. This condition has to be satisfied when designing $K(s)$.

4.3.2 Closed-loop perturbations

In real systems the presence of certain disturbances can affect the stability of the closed-loop system. In Fig. 4.6, a perturbation $\Delta(s)$ is added as a feedback to the stable closed-loop. The connection of the uncertainty to the stable closed-loop is not yet specified since it can represent a measurement error, an amplification of the control input or an excitation of the internal dynamics. For this reason, Δ is modeled as a transfer-function, with a pair of complex-conjugate stable poles $\lambda_\Delta^{1,2} = \sigma_\Delta \pm i\omega_\Delta$ and a zero at σ_Δ, so that the transfer function reads:

$$\Delta(s) = \frac{1}{s - \lambda_\Delta^1} + \frac{1}{s - \lambda_\Delta^2} = \frac{2s - 2\sigma_\Delta}{s^2 - 2\sigma_\Delta s + \sigma_\Delta^2 + \omega_\Delta^2}. \tag{4.17}$$

The closer the poles are to the imaginary axis, the more a resonance will appear if the damping ratio $\zeta = -\sigma_\Delta/\omega_\Delta$ is smaller than 1. In this case the perturbed system is under-damped, i.e. the system will oscillate exceeding the desired output.

In Fig. 4.7 the behavior of the filter for a given frequency $\omega_\Delta = 10 rad/s$ for different values of σ_Δ is presented. The amplitude of the filter transfer function is represented on two axes, one expressed in dB and the other indicating the real absolute value computed from (4.17). It can be noticed that this filter does not behave as a classical low-pass filter, since the gain is not unitary meaning that for every frequency the effect of the disturbance will be always a reduction of the closed-loop transfer function amplitude, except for smaller values of ζ. Once applied to the system, this kind of filter always damps low frequencies by a factor depending on the values of σ_Δ and ω_Δ, while the behavior at higher frequencies is asymptotic as $1/\omega_\Delta^2$.

4.4 Performance and robustness definition

Since the main objective of this paper is to investigate the robustness stability and the performances of an output-feedback compensator, we need to define a set of measures that define unambiguously performance and robustness.

4.4.1 Performance definition

The performance of a generic partial-state control problem, is quantified by a cost function, normally based on a 2-norm or an ∞-norm. For a generic transfer function $H(s)$ describing, in Laplace space, the dynamics between an output $y(t)$ and an input $u(t)$

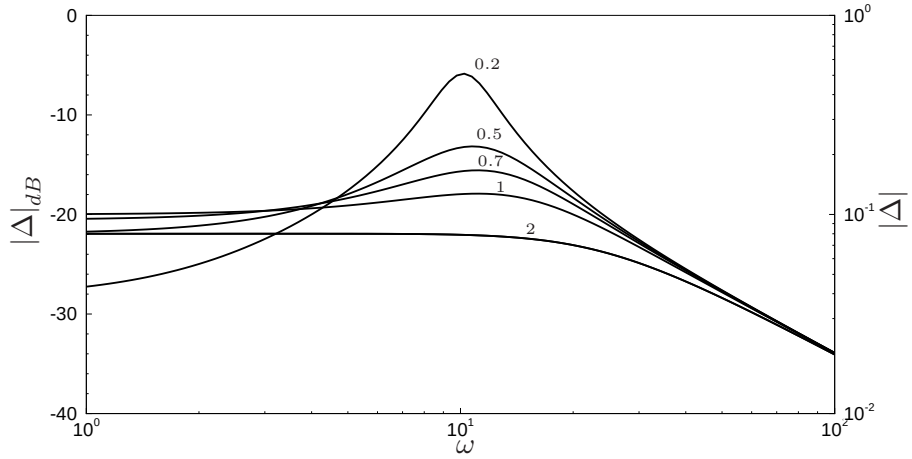

Figure 4.7: Amplitude of the perturbation Δ expressed in dB on the left axis and non-dimensional on the right axis, for a given range of frequencies in rad/s. Every curve is obtained from Eq. (4.17), with a fixed value of $\omega_\Delta = 10 rad/s$. Values close to each curve indicate the damping ratio $\zeta = -\sigma_\Delta/\omega_\Delta$.

(SISO), the 2-norm and the ∞-norm are defined as follows:

$$\|H\|_2 := \left(\frac{1}{2\pi}\int_{-\infty}^{\infty} |H(j\omega)|^2 \,\mathrm{d}\omega\right)^{\frac{1}{2}}, \tag{4.18}$$

$$\|H\|_\infty := \sup_\omega |H(j\omega)| \tag{4.19}$$

In terms of the time domain, it may be shown that: $\|H\|_2 = \|y\|_2$ for a simulation $y(t)$ triggered by $u(t) = \delta$ and $y(0) = 0$, while $\|H\|_\infty = \sup_{\|u\|_2 \neq 0} \frac{\|y\|_2}{\|u\|_2}$ for simulations $y(t)$ triggered by any $u(t)$ and $y(0) = 0$. Here the 2-norm of a signal is defined as $\|y\|_2 = \left(\int_0^\infty |y(t)|^2 \,\mathrm{d}t\right)^{\frac{1}{2}}$. Note that the definition in the time domain is allowed by the Parseval theorem only if stable systems are considered, while the definition in the frequency domain is allowed also for unstable systems as soon as there is no marginal pole.

The cost function is related to desired outputs, experienced noise environments and has properties depending to the used norms. In this study, as well as in the majority of flow control applications, we fixed as reference output the amount of control input $z_u = u$ and the output measurement $z_m = \mathrm{C_2X}$, while the measurement noise and the actuator noise are chosen as the reference disturbance environments. As outlined in Sec. 4.3.1, the compensator shall be designed to guarantee the stability of the closed-loop system. Here we introduce the performance as an additional target of the compensator design. In Fig. 4.8 a scheme describes performance definition as the output of the closed-loop system when excited by the two noises g and w. These definitions hold whatever the control strategy that manages to stabilize the closed-loop system, i.e. the technique used for the compensator design. For both desired outputs, performances are cost functions

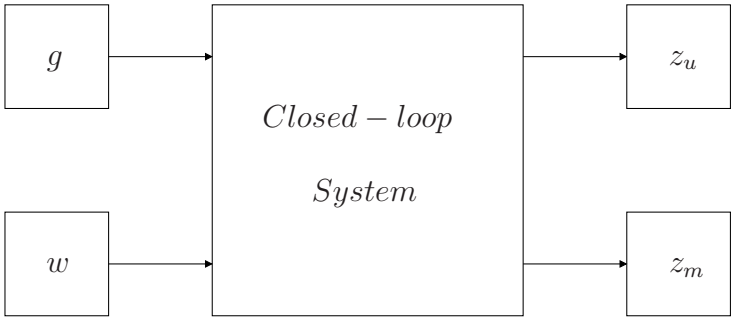

Figure 4.8: Closed-loop system with performances definition.

defined as the 2-norm and the ∞-norm of the closed-loop transfer functions between the disturbances w and g and the reference outputs z_u and z_m. Defining disturbances as $d = \{w, g\}$ and the desired outputs $z = \{z_m, z_u\}$, the set of closed-loop transfer functions read as follows:

$$T_{zd}^{cl}(s) = \begin{bmatrix} T_{mg}^{cl}(s) & T_{mw}^{cl}(s) \\ T_{ug}^{cl}(s) & T_{uw}^{cl}(s) \end{bmatrix} = \begin{bmatrix} \dfrac{P(s)K(s)}{1-P(s)K(s)} & \dfrac{P(s)}{1-P(s)K(s)} \\ \dfrac{K(s)}{1-P(s)K(s)} & \dfrac{P(s)K(s)}{1-P(s)K(s)} \end{bmatrix}, \tag{4.20}$$

so that $z = T_{zd}^{cl}(s)d$. For each term of Eq. (4.20) we can finally define performances as:

$$\Phi_2^{zd} = \left\| T_{zd}^{cl} \right\|_2, \tag{4.21}$$

and

$$\Phi_\infty^{zd} = \left\| T_{zd}^{cl} \right\|_\infty. \tag{4.22}$$

These parameters represent a cost of control design and should be kept as small as possible. A controller has better performance than another if it has smaller values of Φ_∞^{zd} and Φ_2^{zd}.

4.4.2 Classic robustness definition

The discrepancy between the model used in the control design P and the real plant $\tilde{P}$ can lead to a bad performance once the compensator is implemented in the real system $\tilde{P}$. The problem is that if the controller is designed only to have good performances, the stability to unknown perturbations (here $\tilde{P} - P$) is not assured.

The stability of a closed-loop system (Burl, 1998) is always given by an analysis of the zeros of:

$$1 - P(s)K(s) = 0. \tag{4.23}$$

The closed-loop system is internally stable if all the solutions of Eq. (4.23) have negative real parts. Since the closed-loop system is designed to be stable, robustness is the capa-

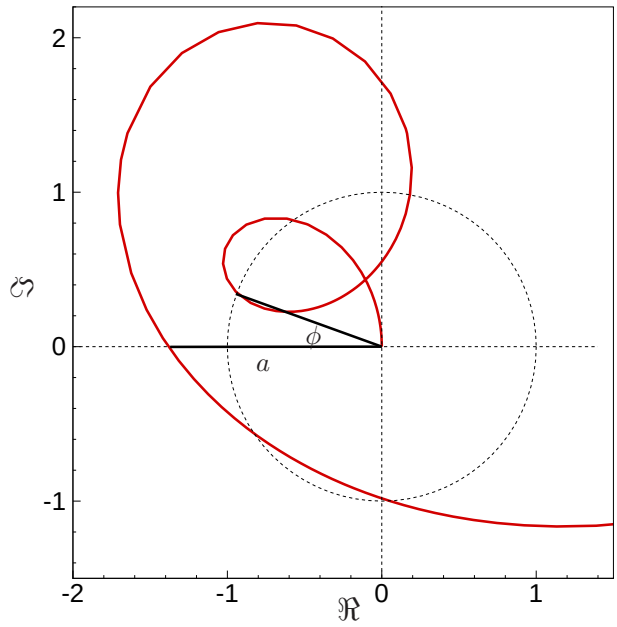

Figure 4.9: Graphical representation of the Nyquist criterion.

bility of the compensated system to remain stable after a perturbation, i.e. the ability of a controller, designed on a reduced model P, of being robust in a slightly different system $\tilde{P}$. Following this definition, if we perturb the compensated plant, the higher the stability margin, the more robust.

In order to quantify the robustness margins, we define the actual plant as the reduced-model plant perturbed by two different perturbations, one that changes its magnitude, i.e. the amplitude of the measured response to a random input, and one its phase, i.e. a delay in the input-output dynamics. These two models are summarized as follows:

$$\tilde{P}(s) = \alpha P(s), \tag{4.24a}$$

$$\tilde{P}(s) = e^{i\phi} P(s). \tag{4.24b}$$

We then define GM^+ as the smallest gain α greater than 1 that produces a zero with a positive real part in $1 - \tilde{P}(s)C(s)$, GM^- as the highest gain α between 0 and 1 that causes the instability of the system, and the phase margin PM as the minimum positive angle ϕ that causes instability.

The robustness analysis described above is the Nyquist stability criterion applied to the uncertain system in Eq. (4.24). From the Nyquist plot, gain and phase margins can

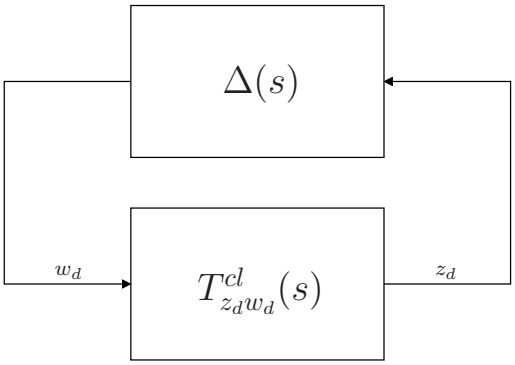

Figure 4.10: Unstructured uncertainty block scheme.

be determined graphically. In particular, from Fig. 4.9, gain margins are defined as:

$$GM^{+} = 20\log_{10}\left(-\frac{1}{a}\right), 0 > a > -1, \tag{4.25a}$$

$$GM^{-} = 20\log_{10}\left(-\frac{1}{a}\right), a < -1, \tag{4.25b}$$

$$PM = \phi. \tag{4.25c}$$

4.4.3 Unstructured uncertainty

In the previous classic robustness definition, the mathematical model used consists in a gain and phase perturbation of the nominal plant $P(s)$. In order to evaluate system robustness, other types of perturbations may be used. In particular, we consider perturbations of the closed-loop system called unstructured uncertainties, whom transfer function is stable and characterized by a given ∞-norm.

We consider the closed-loop system in Fig. 4.10 that has a disturbance input w_d and a perturbed output z_d. We combine the compensator $K(s)$ with the plant $P(s)$ in order to obtain the closed-loop system described by $T^{cl}_{z_d w_d}(s)$ with a stable perturbation $\Delta(s)$ in a feedback loop. If we evaluate the internal stability (the reader is referred to Burl (1998) for a detailed demonstration), we find out that if the perturbation $\Delta(s)$ is stable and bounded, i.e. if $\|\Delta\|_\infty \leq 1/\gamma$, the condition for internal stability is that:

$$\left\|T^{cl}_{z_d w_d}\right\|_\infty < \gamma, \tag{4.26}$$

This result is known as Small Gain Theorem (SGT).

The SGT, as just explained, involves the parameter γ that represents the bound relating the closed-loop system and the admissible stable perturbation. The actual link between $T^{cl}_{z_d w_d}(s)$ and $\Delta(s)$ can be deeply and more clearly analyzed by simply non-dimensionalizing the perturbation with the amplitude of the closed-loop transfer function,

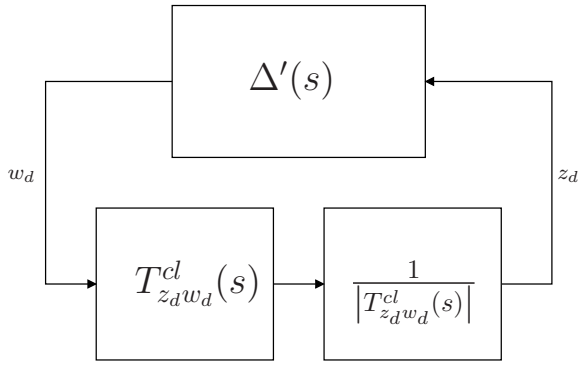

Figure 4.11: Normalized unstructured uncertainty block scheme.

so that:

$$\Delta(s) = \Delta'(s)\frac{1}{\left|T^{cl}_{z_d w_d}(s)\right|}. \tag{4.27}$$

In Fig. 4.11 the normalized system is shown. The stability condition in Eq. (4.26) is still valid, but the normalization implies the the bound on the perturbation Δ' is now expressed as:

$$\left\|\Delta'(s)\right\|_\infty = \left\|\Delta(s)\left|T^{cl}_{z_d w_d}(s)\right|\right\|_\infty \leq 1. \tag{4.28}$$

By definition of the ∞-norm, it follows that the inequality in Eq. (4.28) is valid if:

$$|\Delta(s)| \leq \frac{1}{\left|T^{cl}_{z_d w_d}(s)\right|}, \qquad \forall\omega. \tag{4.29}$$

This last result implies that the condition for robust stability expressed by the SGT is violated, and the system becomes unstable, when the amplitude of a stable perturbation is bigger than the inverse of the amplitude of the closed-loop transfer function. Eq. (4.29) also states that the condition on the amplitude of perturbations and closed-loop system just explained has to be verified for all the range of frequencies. This consideration is hidden in the classical formulation of the SGT in Eq. (4.26). From these considerations, we can then define the maximum disturbance allowed as the inverse of the ∞-norm of the closed-loop transfer function:

$$\rho_\infty = \frac{1}{\left\|T^{cl}_{z_d w_d}(s)\right\|_\infty} \tag{4.30}$$

In this study, we consider two types of connections of the unstructured perturbation to the closed-loop system: the input-multiplicative model and the input-to-output model, both represented in Fig. 4.12.

Input-multiplicative perturbation

This type of perturbations represents unknown perturbations in series with the plant. The model is described in Fig. 4.12(a). The stable disturbance $\Delta(s)$ acts on the stable

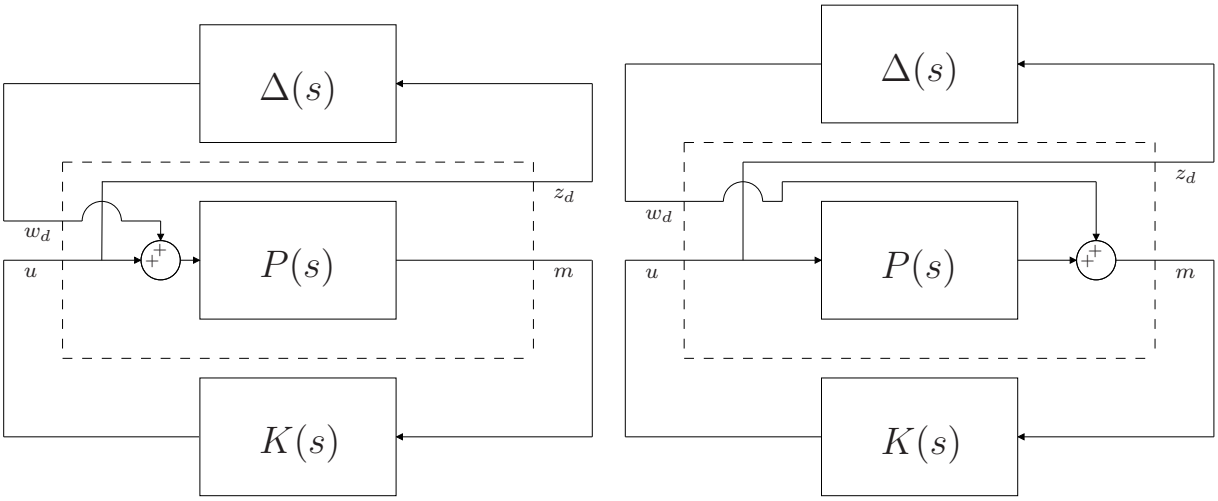

Figure 4.12: Unstructured uncertainty models used. (a) input-multiplicative model; (b) input-to-output model.

closed-loop system by modifying the open-loop transfer function P. The perturbed plant transfer function is then:

$$\tilde{P}(s) = P(s)\left(1 + \Delta(s)\right), \tag{4.31}$$

where $P(s)$ is the nominal plant and in our case corresponds to the reduced model.

The set of equations considered in this particular case, referred to the scheme in Fig. 4.12(a), is then:

$$\dot{\mathrm{X}} = \mathrm{AX} + \mathrm{B}_2 u + \mathrm{B}_2 w_d \tag{4.32a}$$

$$m = \mathrm{C}_2\mathrm{X} \tag{4.32b}$$

$$z_d = u \tag{4.32c}$$

$$w_d = \Delta(s) z_d \tag{4.32d}$$

$$u = K(s) m, \tag{4.32e}$$

from that the closed-loop transfer function can be expressed as:

$$T^{cl,im}_{z_d w_d}(s) = \frac{K(s)P(s)}{1 - K(s)P(s)}. \tag{4.33}$$

Since we are interested in the robust stability of the closed-loop system when the perturbation is introduced to the system as an input-multiplicative disturbance, i.e. when the curve of the amplitude of $\Delta(s)$ remains under the curve of the inverse of the closed-loop transfer function $T^{cl}_{z_d w_d}(s)$, we define the robustness indicator related to this type of

perturbation as:

$$\rho_{\infty}^{im} = \frac{1}{\left\| T_{z_d w_d}^{cl,im}(s) \right\|_{\infty}} \tag{4.34}$$

In order to guarantee robust control, using the SGT we know that, with a stable perturbation, the value of ρ_{∞} shall be as big as possible.

Input-to-output perturbation

The input-to-output perturbation expresses an additive uncertainty operating in parallel with the plant as schematized in Fig. 4.12(b). Adding a stable perturbation $\Delta(s)$ in feedback with the closed-loop system corresponds to a modification of the open-loop transfer function as:

$$\tilde{P}(s) = P(s) + \Delta(s), \tag{4.35}$$

where $P(s)$ is the nominal plant as in the previous case.

We consider as set of equations related to the input-to-output model the following:

$$\dot{\mathrm{X}} = \mathrm{AX} + \mathrm{B}_2 u \tag{4.36a}$$

$$m = \mathrm{C}_2 \mathrm{X} + w_d \tag{4.36b}$$

$$z_d = u \tag{4.36c}$$

$$w_d = \Delta(s) z_d \tag{4.36d}$$

$$u = K(s) m. \tag{4.36e}$$

The closed-loop transfer function can be defined as:

$$T_{z_d w_d}^{cl,io}(s) = \frac{K(s)}{1 - K(s)P(s)}. \tag{4.37}$$

As for the input-multiplicative case, we can define the robustness indicator related to the inverse of the ∞-norm of the closed-loop transfer function defined in Eq. (4.37):

$$\rho_{\infty}^{io} = \frac{1}{\left\| T_{z_d w_d}^{cl,io}(s) \right\|_{\infty}}. \tag{4.38}$$

4.4.4 Summary

Performances and robustness represent the features on which a controller efficacy is evaluated. In this section these characteristics have been defined. Performances are classically defined as the 2-norm and the ∞-norm of the closed-loop transfer functions from the external disturbances and the desired outputs. On the other hand, robustness can be defined from the classical Nyquist approach as stability margins or in a modern inter-

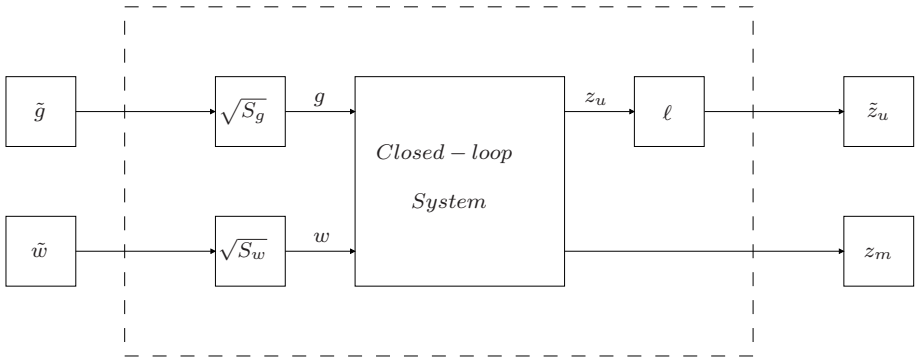

Figure 4.13: Closed-loop system with performances and design parameters.

pretation of the small gain theorem. This study provided a new definition of robustness as the maximum stable disturbance allowed that makes the closed-loop system unstable. This perturbation can be modeled as an unstructured uncertainty in feedback to the system and the robustness indicator can be defined as the inverse of the ∞-norm of the closed-loop transfer function from the perturbed input to the perturbation output.

4.5 Control design targeting performance

Flow control implies the modification of the normal behavior of a flow in order to obtain a desired state. To this aim, among different active-control strategies, optimal control is frequently used. In this study we analyze optimal-control related strategies and we evaluate in each case the robustness measures. We then consider for the compensator design the closed-loop system represented in Fig. 4.6 and the input/output definition schematized in Fig. 4.13. The blocks containing S_g and S_w represent noise weights that in the particular case of white noises correspond to the noise variances, while ℓ is the control cost. The resulting set of equations is then:

$$\dot{\mathrm{X}} = \mathrm{A}\mathrm{X} + \mathrm{B}_2 u + \mathrm{B}_2\sqrt{S_w}\tilde{w}, \tag{4.39a}$$

$$m = \mathrm{C}_2\mathrm{X} + \sqrt{S_g}\tilde{g}, \tag{4.39b}$$

$$z_m = \mathrm{C}_2\mathrm{X}, \tag{4.39c}$$

$$\tilde{z}_u = \ell u, \tag{4.39d}$$

$$u = K(s)m. \tag{4.39e}$$

The control design is based on a variational principle that leads to a minimization of a cost function of the desired output. This cost function could be different if we consider a $\mathcal{H}_2$ control, that minimizes the 2-norm, or a $\mathcal{H}_\infty$ control, that minimizes the ∞-norm. Once the desired output z is specified, the minimization of the cost function leads to a pair of Riccati equations, one corresponding to the controller, the other one to the estimator.

For each case, we define the minimized norm, the cost function, the Riccati equations for the controller and the estimator, and the final form of the compensator. We eventually show and discuss performances and robustness results.

4.5.1 LQG in small gain limit hypothesis

Optimal control methodologies are widely used in flow control applications. Linear Quadratic Regulator (LQR) technique provides the designer with flexibility to perform trade-offs among various performance criteria. The limitation of this method is that the state must be known when generating the control. High-order systems represent then a huge limitation since measuring the whole state can be expensive. A preferable methodology consists in using a partial state information and then estimating the state with a Kalman filter. When the LQR is coupled with a state estimator and control noise and measurement disturbances are modeled as white noise, we obtain a Linear Quadratic Gaussian (LQG) regulator. Details on LQR and Kalman filter design can be found in any control manual as in Burl (1998).

The objective of the LQG control is the optimal minimization of the closed-loop transfer function. Here the term "optimal" refers to seeking the minimum of the 2-norm of the closed-loop transfer function Φ_2^{zd}, as it is defined in Sec. 4.4. In the present study we consider the Small Gain Limit (SGL) hypothesis. As explained in Barbagallo et al. (2009), it consists in a condition that appears as the control cost ℓ and the ratio between measurement disturbance $\sqrt{S_g}$ and input noise $\sqrt{S_w}$ tend to infinity. In this particular situation, the controller and the Kalman filter act only on the unstable modes. Under this particular condition, the design reduces to the minimization of the 2-norm of the closed-loop transfer function between the measurement perturbation and the control input, i.e. the minimization of Φ_2^{ug}.

In the following, a description of the design technique is given along with the analysis of performance and robustness results.

Framework

The design of an LQG compensator consists of a LQR controller and a state estimator, the Kalman Filter. Both controller and estimator are designed from a variational principle that minimizes a cost function, leading to a Riccati equation. This kind of controller follows the $\mathcal{H}_2$ control theory, since the cost function is obtained from the 2-norm of the desired output. In the $\mathcal{H}_2$ framework, the control and the estimator design are decoupled, so we firstly proceed to the design of the controller. The cost function can be formalized

as that corresponding to the LQR design:

$$\mathcal{F}_c^2 = \int_0^T (\mathrm{C_2X})^* \, \mathrm{C_2X} + \ell^2 u^2 \mathrm{d}t. \tag{4.40}$$

The minimization of Eq. (4.40) leads to the Riccati equation:

$$\mathrm{A}^*\mathcal{X} + \mathcal{X}\mathrm{A} - \mathcal{X}\mathrm{B_2B_2^*}\mathcal{X} + \frac{1}{\ell^2}\mathrm{C_2^*C_2} = 0 \tag{4.41}$$

but, since we are in the SGL, the last term is negligible, so that:

$$\mathrm{A}^*\mathcal{X} + \mathcal{X}\mathrm{A} - \mathcal{X}\mathrm{B_2B_2^*}\mathcal{X} = 0. \tag{4.42}$$

We express the control gain matrix that stabilizes the system 4.9, as $\mathrm{K} = -\mathrm{B_2}\mathcal{X}$.

The design of the Kalman filter follows the same procedure of the controller design. The estimated state is described by the following equation:

$$\dot{\mathrm{X}}_e = \mathrm{AX}_e + \mathrm{B_2}u - \mathrm{L}\left(m - \mathrm{C_2X}_e\right), \tag{4.43}$$

where the matrix L is the Kalman gain. Since the estimation leads to an error from the real state, the design of the Kalman filter has the objective of minimizing the mean square estimation error between the real state X and X_e. The error dynamics equation can be obtained by subtracting Eq. (4.43) to the first line of Eq. (4.39):

$$\dot{e} = \left(A - \mathrm{LC_2}\right) e + \mathrm{B_2}\sqrt{S_w}\tilde{w} - \mathrm{L}\sqrt{S_g}\tilde{g}. \tag{4.44}$$

The objective functional can be formalized as:

$$\mathcal{F}_e^2 = \int_0^T E\left[e^* e\right] \mathrm{d}t, \tag{4.45}$$

where the function $E[]$ stands for the expected value.

The minimization of the objective functional in Eq. (4.45) leads to a Riccati equation for the estimator:

$$\mathrm{A}\mathcal{Y} + \mathcal{Y}\mathrm{A}^* - \mathcal{Y}\mathrm{C_2^*C_2}\mathcal{Y} + \frac{S_w}{S_g}\mathrm{B_2B_2^*} = 0, \tag{4.46}$$

which reads in the SGL:

$$\mathrm{A}\mathcal{Y} + \mathcal{Y}\mathrm{A}^* - \mathcal{Y}\mathrm{C_2^*C_2}\mathcal{Y} = 0, \tag{4.47}$$

with $\mathcal{Y}$ satisfying the Riccati equation. The Kalman gain can be eventually computed as $\mathrm{L} = -\mathcal{Y}\mathrm{C_2^*}$. Since the feedback input is related to the estimated state as $u = \mathrm{KX}_e$, we

Re	GM^+	GM^-	PM	ρ_∞^{im}	ρ_∞^{io}	Φ_2^{mg}	Φ_2^{ug}	Φ_∞^{mg}	Φ_∞^{ug}	Φ_2^{mw}	Φ_2^{uw}	Φ_∞^{mw}	Φ_∞^{uw}
5500	2.28	-1.06	8.62	0.12	47.7	7.04	0.019	8.68	0.021	2978	7.04	3179	8.68
6500	1.82	-0.65	7.75	0.07	42.4	8.56	0.022	14.1	0.024	8032	8.56	43307	14.1
7500	0.32	-0.53	2.32	0.04	39.5	10.2	0.025	26.4	0.025	23389	10.2	181016	26.4
8000	0.73	-0.88	5.06	0.09	38.7	9.91	0.025	11.5	0.026	8556	9.91	40520	11.5

Table 4.1: Robustness analysis results at different Reynolds numbers on the SGL conditions. Gain margins are in dB and phase margin is in degrees.

can define the output feedback transfer function that appears in Eq. (4.39):

$$K(s) = -\mathrm{K}\left[sI - (\mathrm{A} + \mathrm{B_2K} + \mathrm{LC_2})\right]^{-1}\mathrm{L}. \tag{4.48}$$

The compensator designed with the technique described above can be analyzed on its performance and robustness behavior.

Results

The LQG compensator is one of the most used algorithm in many control problems. Unfortunately, the resulting compensator lacks robustness and this is considered as an important issue in real control applications. A robustness and performance analysis is carried out to show this behavior at different Reynolds numbers. The objective in this analysis is to know how the plant, manipulated by a compensator designed on a given reduced model, reacts to stable perturbations added to the compensated system and so when the system begins to be unstable.

In Table 4.1 are summarized performance and robustness results. Since control design targets performance with a $\mathcal{H}_2$ approach, we expect to obtain small values of the Φ_2^{zd}. In particular, due to the SGL hypothesis, values of the quantity Φ_2^{ug} are the smallest that can be obtained with any control technique. For this reason, values corresponding to this quantity are taken as reference for comparison with other control techniques. Practically, the value of 0.021, representing the performance Φ_2^{ug} for Reynolds 5500, is the lowest cost payed in the present study, with comparison to all control techniques studied.

The design of the LQG is based on performance minimization and the consequence is a lack in robustness. The observation of Nyquist stability margins reveals admissible amplitude perturbations about $\pm 1dB$ and phase margins below 10 , evincing poor robustness. Parameters ρ_∞^{im} and ρ_∞^{io} express the bound of admissible perturbations introduced in series and in parallel to the closed-loop system before the closed-loop system becomes unstable. Since the input-multiplicative perturbation seems to be the most critical we use it as an example to better understand the meaning of this kind of uncertainties and the SGT.

In fig. 4.14(a) is represented the stability threshold of the closed-loop system perturbed by an input-multiplicative uncertainty $\Delta(s)$ as defined in Eq. (4.17). The graphic is

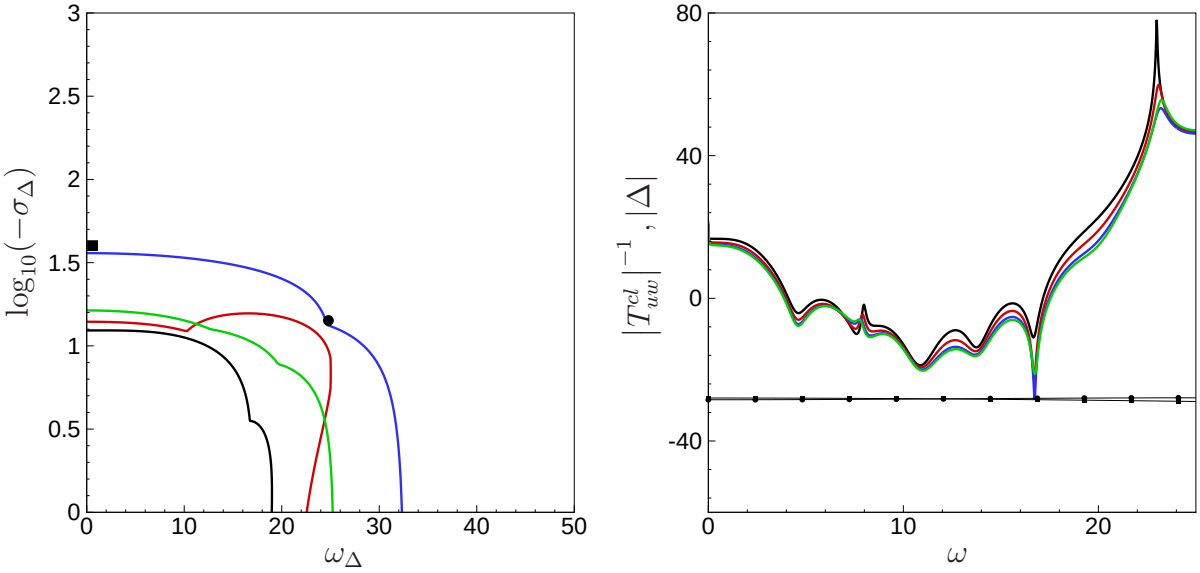

(a) (b)

Figure 4.14: (a) Stability threshold for an input-multiplicative perturbation of a closed-loop system with an LQG/SGL compensator at different Reynolds numbers; (b) amplitude, expressed in dB, of the inverse closed-loop transfer function. For both figures, the black line corresponds to $Re = 5500$ case, red line $Re = 6500$, blue line $Re = 7500$ and green line $Re = 8000$. Lines with squares and circles in (b) represent $|\Delta|$ and are obtained with the fixed values of σ_Δ and ω_Δ represented by a square and a circle in (a).

obtained by varying the parameters σ_Δ and ω_Δ. Inside the bounded region (the lowest left corner), the perturbed closed-loop system is unstable. As explained in Sec. 4.4.3, the instability arises when the amplitude of the perturbation is bigger than the inverse of the amplitude of the closed-loop transfer function. The parameter ρ_∞^{im} indicates how large could be the admissible perturbation or, in other words, how big is the minimum of $1/\left|T_{uw}^{cl}\right|$. As expected from the values of ρ_∞^{im}, the case corresponding to $Re = 7500$ is the least robust, while the closed-loop system designed at $Re = 5500$ is the most robust, but results for the other two cases are in contrast with robustness analysis, even though they are coherent with Nyquist margins criterion. This misleading result comes from the closed-loop transfer function. If we look at the amplitude of $1/\left|T_{uw}^{cl}\right|$, shown in Fig. 4.14(b), we observe a negative peak that is more accentuated for $Re = 7500$ and it progressively attenuates by diminishing the Reynolds. This local minimum is equivalent to ρ_∞^{im} for $Re = 7500$ and 8000 and its presence at high frequency makes these last cases less robust.

Summary

The linear quadratic control is the most used technique on flow control applications. It has been considered in this study as it represents the simplest way to obtain a linear controller and a reference case to understand performance and robustness analysis. It has been shown that, since this design technique is optimized on a 2-norm performance, the obtained compensator presents poor robustness properties in terms of stability margins as well as rejection of unstructured uncertainties. This result suggests to seek other techniques to achieve satisfying robustness properties.

4.5.2 Loop transfer recovery

From the optimal control theory (Burl, 1998; Zhou et al., 1996), we have knowledge of high robustness properties of linear quadratic regulators. They present, in fact, gain margins between 0.5 and ∞ ($GM^- = -6dB$ and $GM^+ = \infty dB$) and phase margin of at least 60 . This is valid only if the entire state is known at every instant. By duality, a similar consideration can be done for an optimal estimator, i.e. the Kalman filter. When the controller is realized combined with an estimator, robustness properties are not guaranteed anymore, indeed in some cases these margins are reduced to values such low to easily transform the system from stable to unstable even for small changes in its characteristic parameters. The reason of this behavior is that the open-loop transfer function of the optimal controller and that of the Kalman filter are completely different from that obtained by combining controller and estimator.

The technique of the Loop Transfer Recovery (LTR) tries to design the estimation gain

matrix L of the LQG in order to recover stability margins and the robustness to input-multiplicative perturbations of the LQR. The LTR method can be intuitively understood by considering the closed-loop system opened between the control input and the Kalman filter and making the dynamic of the estimator sufficiently fast to be ignored. This purpose can be accomplished with the introduction of a fictitious noise $w_f(t)$, with variance S_{w_f}, to the control input in the estimator design. By increasing the noise to ∞ the poles are driven toward a condition where they are canceled by the plant zeros, leading the open-loop transfer function to that of the optimal estimator. Since this technique is based on a cancellation poles-zeros, it is not applicable if there are no zeros in the right haf-plane, i.e. for minimum phase systems, and the number of measurements is greater than or equal to the number of control inputs.

The addition of the fictitious noise in the Kalman filter design leads to a suboptimal LQG problem with noise increasing. The consequence is an increment in robustness properties, but on the other hand also an increment of the cost as the noise is increased. The design of the LQG/LTR compensator is then based on a compromise between robustness and performance. As this technique is a modification of the LQG problem, the objective of the the LQG/LTR control problem is the minimization of the 2-norm of the closed-loop transfer function. In this case, since the control cost and the noise ratio can assume any values, there is not a preferred minimized performance as in the previous case, but all the four components of Φ_2^{zd} are minimized.

In the following a description of the framework is briefly summarized. Thereafter, a sensitivity analysis on the design parameters is given and finally, results for the best-robustness case are presented.

Framework

In the LQG/LTR control design the objective functional for the controller and the estimator are defined as in Eq. (4.40) and (4.45). With respect to the previous case, the design parameters can assume finite values, in particular the control cost ℓ can tend to a small value, meaning a "cheap" control, as well as to a great value, leading again the controller to the SGL hypothesis. The noise ratio S_{w_f}/S_g has also a finite value and could be chosen as a design parameter.

The LTR framework is similar to the SGL case, being both LQG controllers. The Riccati equation for the controller is then:

$$\mathrm{A}^*\mathcal{X} + \mathcal{X}\mathrm{A} - \frac{1}{\ell^2}\mathcal{X}\mathrm{B}_2\mathrm{B}_2^*\mathcal{X} + \mathrm{C}_2^*\mathrm{C}_2 = 0, \tag{4.49}$$

where ℓ is a finite number and the control gain matrix defined as $\mathrm{K} = -\ell^{-2}\mathrm{B}_2\mathcal{X}$. Note that in the limit $\ell \to \infty$, we reach the SGL hypothesis(see Sec. 4.5.1).

The Kalman filter design is then depending on the ratio S_{w_f}/S_g. The associated Riccati equation reads:

$$\mathrm{A}\mathcal{Y} + \mathcal{Y}\mathrm{A}^* - \frac{S_{w_f}}{S_g}\mathcal{Y}\mathrm{C}_2^*\mathrm{C}_2\mathcal{Y} + \mathrm{B}_2\mathrm{B}_2^* = 0. \tag{4.50}$$

The Kalman gain matrix is defined as $\mathrm{L}_{LTR} = -S_{w_f}/S_g\mathcal{Y}\mathrm{C}_2^*$, while the output feedback transfer function $K(s)$ has the same structure as in Eq. (4.48. Note that in the limit $S_{w_f}/S_g \to 0$, we reach the SGL hypothesis (see Sec. 4.5.1).

Since we can vary the values of ℓ and S_{w_f}/S_g, a parametric study on these two parameters can be performed.

Parametric study

The two parameters, the control cost ℓ and the noise ratio S_{w_f}/S_g, can be taken in a large range of values. A parametric study will then enable to find which combination is the most robust and also the most affordable in terms of performances. For each case, the investigated range for the control cost is between 10^{-4} and 10^4, while the noise ratio is varied within 10^{-8} and 10^8.

Contour plots in Fig. 4.15 show the robustness indicator ρ_∞^{im} computed for every Reynolds number along with the iso-lines representing the quantity ρ_∞^{io}. For every case the behavior is the same with a region of high robustness for positive values of $\log_{10}(S_{w_f}/S_g \cdot \ell^2)$, with a local maximum, for both ρ_∞^{im} and ρ_∞^{io}, obtained at intermediate values of ℓ^2 and S_{w_f}/S_g. We then choose, as design point for the LQG/LTR control, a cost weight of $\ell = 10^{1.75}$ and a noise ratio of $S_{w_f}/S_g = 10^{-3.5}$, which corresponds to the maximum robustness to input-multiplicative and input-to-output stable perturbations.

Results for $\ell = 10^{1.75}$ and $S_{w_f}/S_g = 10^{-3.5}$

In Tab. 4.2 results for the best-robustness property case are summarized. Robustness and performances can be easily compared to the SGL case, since both control design are made with the $\mathcal{H}_2$ approach. The case analyzed here presents a smaller value of ℓ than the SGL and a bigger value of S_w, increased by the fictitious noise. These have a consequence on performances depending on the control input, namely Φ_2^{ug} and Φ_2^{uw}. In particular, while the reduced cost of control leads to an increment in the performance related to the control input, as in Φ_2^{ug}, the increment of noise acts in the opposite way, leading to a smaller value of Φ_2^{uw} than that of the SGL case.

The LTR technique has been introduced to increase robustness an this result is clearly achieved as it can be observed by analyzing values of stability margins and unstructured perturbations rejection. If compared with the previous case, in fact, the maximum disturbance allowed has been increased from 50% to 250% considering a input-multiplicative

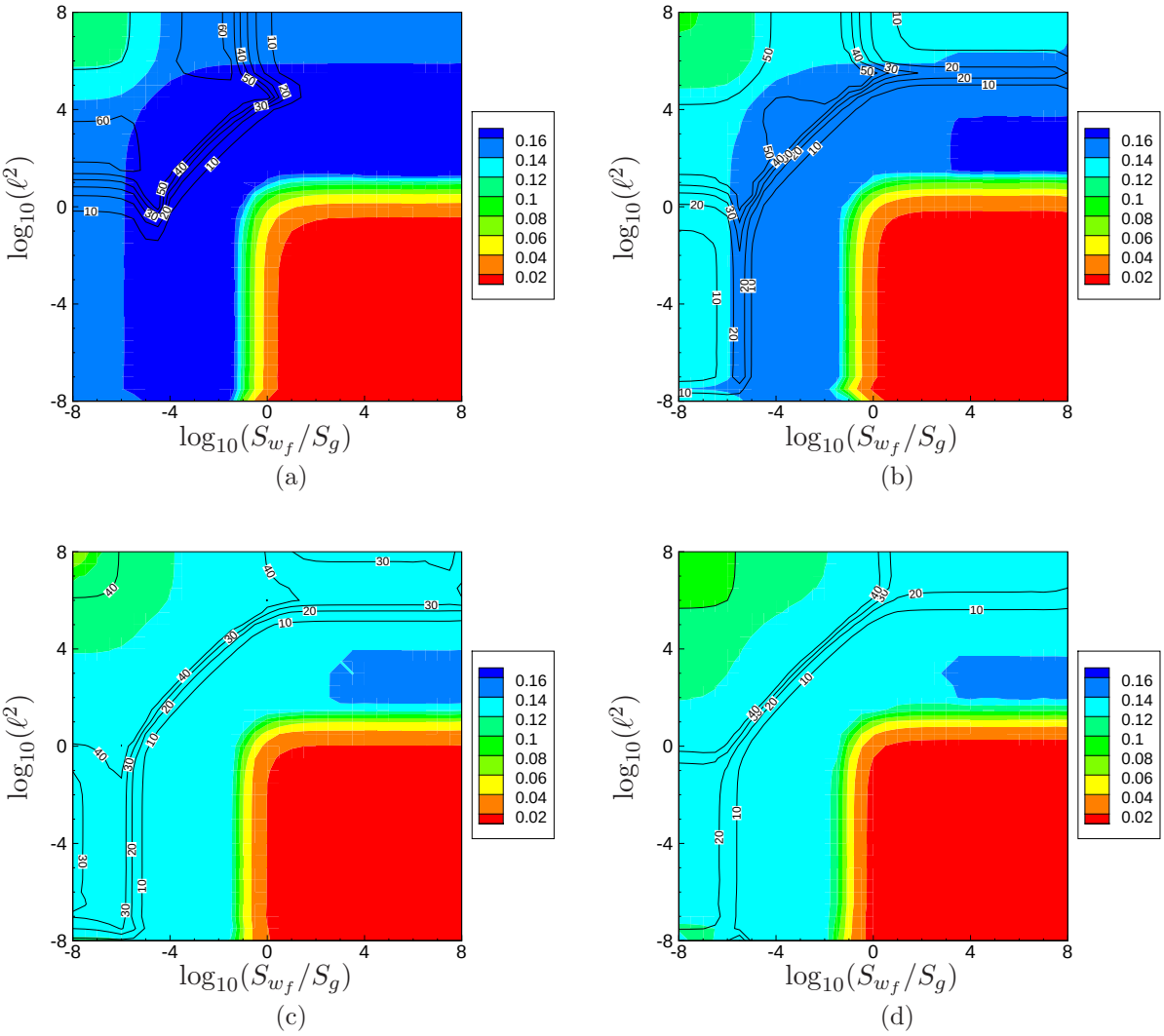

Figure 4.15: Parametric analysis over the four different Reynolds numbers. Contours correspond to the robustness parameter ρ_∞^{im}. Iso-lines correspond to ρ_∞^{io}

Re	GM^+	GM^-	PM	ρ_∞^{im}	ρ_∞^{io}	Φ_2^{mg}	Φ_2^{ug}	Φ_∞^{mg}	Φ_∞^{ug}	Φ_2^{mw}	Φ_2^{uw}	Φ_∞^{mw}	Φ_∞^{uw}
5500	1.54	-1.72	10.2	0.18	54.1	6.60	0.028	5.66	0.019	2493	6.60	1897	5.66
6500	1.32	-1.46	8.78	0.15	49.0	7.71	0.032	6.57	0.020	2890	7.71	2218	6.57
7500	1.18	-1.29	7.84	0.14	47.3	8.71	0.038	7.35	0.021	3336	8.71	2645	7.35
8000	1.13	-1.23	7.50	0.13	47.6	9.15	0.043	7.67	0.021	3577	9.15	2885	7.67

Table 4.2: Best robustness analysis results at different Reynolds numbers on the LQG/LTR controller design. Gain margins are in dB and phase margin is in degrees. All results are for $S_{w_f}/S_g = 10^{-3.5}$ and $\ell^2 = 10^{3.5}$

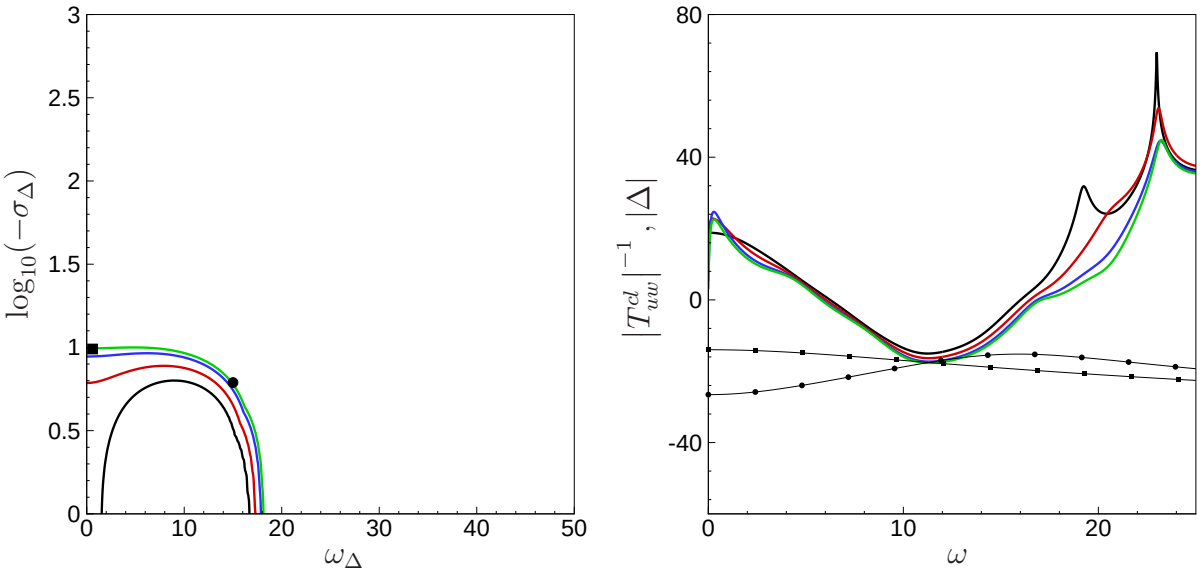

(a) (b)

Figure 4.16: (a) Stability threshold for an input-multiplicative perturbation on closed-loop systems with an LQG/LTR compensator at different Reynolds numbers; (b) amplitude, expressed in dB, of the inverse closed-loop transfer function; the amplitude is expressed in dB while the frequency in rad/s. For both figures, black line corresponds to $Re = 5500$ case, red line to $Re = 6500$, blue line to $Re = 7500$ and green line to $Re = 8000$. Lines with squares and circles in (b) represent $|\Delta|$ and are obtained with the fixed values of σ_Δ and ω_Δ represented by a square and a circle in (a).

perturbation and between 15 and 20% for a input-to-output perturbation.

In Fig. 4.16(a) the stability threshold is clearly coherent with ρ_∞^{im} in Tab. 4.2, since robustness decreases with Reynolds numbers, and the bounded region is also narrower than in the previous case. The explanation to this result is evident by looking at the clean shape of the amplitude of $1/\left|T_{uw}^{cl}\right|$ in Fig. 4.16(b) and the absence of other local minima.

Summary

The loop transfer recovery is a method that modifies the LQG technique in order to make the estimator dynamics infinitely faster than those of the controller. Under these conditions the compensator can be considered as a linear quadratic regulator that presents good robustness properties. These conditions are obtained with the introduction of a fictitious noise into the system in the estimator design phase. Even though robustness has been increased, this method presents some drawbacks related to its application in non-minimum phase systems.

4.5.3 $\mathcal{H}_\infty$ control

Control design techniques previously proposed are based on the minimization of the 2-norm of the closed-loop transfer function. The main limitation of the family of compensators designed with a $\mathcal{H}_2$ strategy is a poor robustness to external perturbations and even with the help of corrective methods as the LTR, the robustness problem is not completely solved. Instead of a 2-norm approach, the optimization problem can be formulated with a different approach, based on a ∞-norm. This design control strategy has been introduced by Doyle et al. (1989) and succesfully, in terms of increment in robustness, applied by Bewley and Liu (1998) since it has been related to the minimization of the worst-case of disturbance that represents a classic engineering problem.

The $\mathcal{H}_\infty$ technique analyzed here has the functional objective to minimize the upper bound of the ∞-norm of the closed-loop transfer function from the control input to the measurement noise, Φ_∞^{ug}. Therefore, even though from this strategy a good robustness is often recovered, the $\mathcal{H}_\infty$ control design can be considered a performance-based technique. The solution of the control problem, formalized with a Riccati approach, is not unique since it provides a family of stabilizing controllers that satisfy the condition of the closed-loop transfer function bounded by a design parameter γ.

In the following, the $\mathcal{H}_\infty$ control problem is formulated as a min-max problem and robustness and performances results of the obtained controller are then discussed.

Framework

The formulation of the cost function, for controller and estimator, can be expressed as a min-max problem. The objective of these problems is to find, for the controller, the optimal control input that minimizes the effect of the worst possible disturbance and, for the estimation problem, the measurement m such that the closed-loop transfer function between the disturbance input and the estimation error is bounded. For both problems, the bound of the closed-loop transfer function is expressed by the parameter γ, which acts in opposition with the cost of the control input and the estimation error minimization, but has the foremost role of coupling the design of controller and estimator, since it appears in both Riccati equations.

The two cost function can be expressed as follows:

$$\mathcal{F}_\rfloor^\infty = \int_0^T (\mathrm{XC}_2)^* \, \mathrm{C}_2\mathrm{X} + \ell^2 u^2 - \gamma^2 w^2 \mathrm{d}t, \tag{4.51}$$

for the controller, and

$$\mathcal{F}_e^\infty = \int_0^T E\left[e^* e\right] - \gamma^2 w^2 \mathrm{d}t, \tag{4.52}$$

for the estimator. Note that the state equation of the estimation error differs from that

in Eq. (4.43). The estimated state, in fact, can be expressed as:

$$\frac{\mathrm{dX}_e}{\mathrm{d}t} = \mathrm{A}_\infty \mathrm{X}_e - \mathrm{Z}_\infty \mathrm{L}m, \tag{4.53}$$

where A_∞ and Z_∞ read as follows:

$$\mathrm{A}_\infty = \mathrm{A} + \frac{1}{\gamma^2}\mathrm{B}_2\mathrm{B}_2^*\mathcal{X} + \mathrm{B}_2\mathrm{K} + \mathrm{Z}_\infty\mathrm{L}\mathrm{C}_2, \tag{4.54a}$$

$$\mathrm{Z}_\infty = \left(I - \frac{1}{\gamma^2}\mathcal{X}\mathcal{Y}\right)^{-1}, \tag{4.54b}$$

being $\mathcal{X}$ and $\mathcal{Y}$ solutions of the Riccati equations for the controller

$$\mathrm{A}^*\mathcal{X} + \mathcal{X}\mathrm{A} - \mathcal{X}\left(\frac{1}{\ell^2}\mathrm{B}_2\mathrm{B}_2^* - \frac{1}{\gamma^2}\mathrm{B}_2\mathrm{B}_2^*\right)\mathcal{X} + \mathrm{C}_2^*\mathrm{C}_2 = 0, \tag{4.55}$$

and for the estimator:

$$\mathrm{A}\mathcal{Y} + \mathcal{Y}\mathrm{A}^* - \mathcal{Y}\left(\frac{S_w}{S_g}\mathrm{C}_2^*\mathrm{C}_2 - \frac{1}{\gamma^2}\mathrm{C}_2^*\mathrm{C}_2\right)\mathcal{Y} + \mathrm{B}_2\mathrm{B}_2^* = 0. \tag{4.56}$$

Furthermore, the solutions of equations (4.55) and (4.56) are subordinated to a condition on the spectral radius, i.e. the maximum eigenvalue $\lambda_i \in \mathbb{C}$, of the scalar product $\mathcal{X}\mathcal{Y}$:

$$\rho\left(\mathcal{X}\mathcal{Y}\right) = \max_i\left(|\lambda_i|\right) < \gamma^2. \tag{4.57}$$

The above condition has to be satisfied and imposes the lower limit of λ_i. The procedure is then to fix ℓ and the ratio S_w/S_g and decrease iteratively the value of γ, until the condition in Eq. (4.57) is violated. We eventually express the gain matrix $\mathrm{K} = -\mathrm{B}_2^*\mathcal{X}$ and the Kalman matrix $\mathrm{L} = -\mathcal{Y}\mathrm{C}_2^*$.

The output feedback transfer function can easily be computed from the system described in Eq. (4.53) and reads as:

$$K(s) = -\mathrm{K}\left(sI - \mathrm{A}_\infty\right)^{-1}\mathrm{Z}_\infty\mathrm{L}. \tag{4.58}$$

Results

The performance and robustness analysis is carried out with different values of parameters ℓ and S_w/S_g. In Tables 4.3 results for the most robust case are summarized. The set of parameters has been varied to reproduce some cases of interest in order to have a comparison with the other control cases. Among the entire set of studied cases, the one with noise ratio and control cost fixed as in the LQG/LTR case has resulted in the best results. Especially in terms of negative gain margin, the min-max problem seems

Re	γ	GM^+	GM^-	PM	ρ_∞^{im}	ρ_∞^{io}	Φ_2^{mg}	Φ_2^{ug}	Φ_∞^{mg}	Φ_∞^{ug}	Φ_2^{mw}	Φ_2^{uw}	Φ_∞^{mw}	Φ_∞^{uw}
5500	2.49	0.015	-3.27	1.04	0.002	0.51	40.0	0.143	562	1.98	11486	40.0	159723	562
6500	2.67	0.014	-2.80	0.83	0.001	0.40	49.7	0.165	764	2.50	15251	49.7	234085	764
7500	2.81	0.013	-2.49	0.91	0.002	0.51	48.5	0.150	652	1.95	16248	48.5	218550	652
8000	2.87	0.012	-2.37	0.87	0.001	0.51	51.2	0.153	696	1.97	17982	51.2	145252	696

Table 4.3: Robustness analysis results at different Reynolds numbers for a $\mathcal{H}_\infty$ controller that targets performance. Gain margins are in dB and phase margin is in degrees. All results are for $S_w/S_g = 10^{-3.5}$ and $\ell^2 = 10^{3.5}$

to ameliorate this robustness indicator, but all other quantities, expressing robustness or performances, are considerably worse than for previous cases.

In particular in Fig. 4.17(a), we remark a wide unstable area for small frequencies and compared to other cases no advantage in robustness has been gained by using this compensator. Reynolds dependency also plays a key role, stronger than in the LQG/SGL, and it is evident by observing the closed-loop transfer function amplitude in Fig. 4.17(b) that shows a more pronounced negative peak for $Re = 5500$ and 7500. The presence of this peak, as for the SGL case, seems to be coherent with the positive gain margin and the phase margin, that are worse for these last cases.

The reason why this controller fails so badly is not truly investigated. Our purpose was to simply apply the method proposed by Bewley and Liu (1998). Our objective is to show how the "classic" robust control strategy cannot be applied as it is, just as an optimization of the min-max problem using the ∞-norm. In other words, our purpose was to prove that a $\mathcal{H}_\infty$ design does not necessarily yield a robust controller, as already suggested by Burl (1998).

Summary

In this section, a compensator has been designed with the classical $\mathcal{H}_\infty$ technique, introduced by Doyle et al. (1989). This method provides a controller based on the minimization of the ∞-norm of the closed-loop transfer function. Contrary to Bewley and Liu (1998), this technique shows catastrophic results in terms of robustness. We have shown here that the simple application of this method, if a perturbation rejection model is not included in control design, does not automatically provide a robust compensator.

4.6 Control design targeting robustness

In order to obtain a robust controller we studied a different approach to that proposed by Doyle et al. (1989) and applied in Bewley and Liu (1998). The strategy comes from the $\mathcal{H}_\infty$ control theory, but involves the application of the Small Gain Theorem (SGT) when feedback stable perturbations act on the clsoed-loop system. The method proposed in this section deeply differs from the previous $\mathcal{H}_\infty$ control, since the objective is not just to

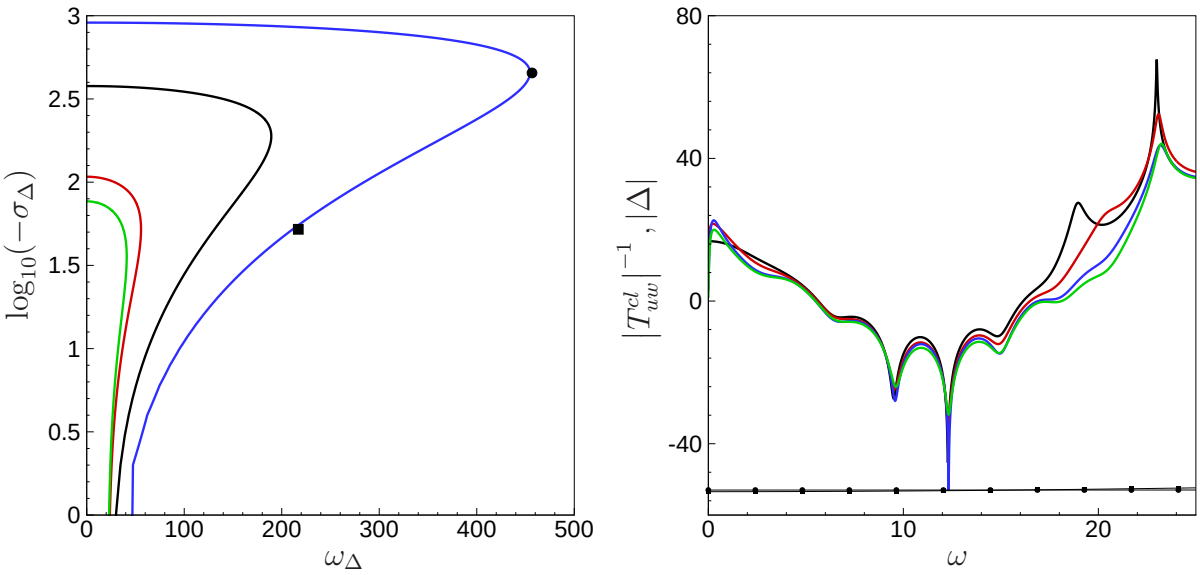

(a) (b)

Figure 4.17: (a) Stability threshold for an input-multiplicative perturbation on closed-loop systems with a "classic" $\mathcal{H}_\infty$ compensator at different Reynolds numbers; (b) amplitude, expressed in dB, of the inverse closed-loop transfer function. For both figures, the black line corresponds to $Re = 5500$ case, the red line to $Re = 6500$, the blue line to $Re = 7500$ and the green line to $Re = 8000$. Lines with squares and circles in (b) represent $|\Delta|$ and are obtained with the fixed values of σ_Δ and ω_Δ represented by a square and a circle in (a).

minimize the ∞-norm of the closed-loop transfer function. In this case, an unstructured uncertainty is added in feedback to the closed-loop system so that the desired output of the system is the input of the disturbance model, whose output is the input of the compensator. Control design problem has the objective of maximize the allowed perturbation delta with a $\mathcal{H}_\infty$ approach, i.e. maximize the bound of ∞-norm of Δ.

The SGT, explained in Sec. 4.4, states that the condition on the perturbation model can be satisfied with the minimization of the ∞-norm of the closed-loop transfer function between the perturbation output and the perturbed input. This objective leads to a compensator that directly targets a specific disturbance with respect to whom the closed-loop system is led to be more robust. Here, two different models of unstructured disturbances are considered: the input-multiplicative model and the input-to-output model. For each control design strategy, the framework describing the design technique and results of performance and robustness of the obtained compensators are given.

4.6.1 Input-multiplicative perturbation

In this case we chose as disturbance an input noise proportional to the control input, that is now the disturbance performance z_d, applied to the closed-loop system as in the system in Fig. 4.12(a). As discussed in Sec. 4.4, the input-multiplicative perturbation represents a disturbance in series with the system, commonly present in engineering problems. Increasing the rejection ability of the compensator to this kind of perturbations represents a desired achievement in control design, as seen for the LTR technique.

From the definition of the input-multiplicative unstructured uncertainty defined by Eq. (4.32) and schematized in Fig. 4.12(a), the controller is designed and both performances and robustness results are analyzed.

Framework

The compensator design is based on the minimization of the ∞-norm of the closed-loop transfer function between the disturbance model input w_d and output z_d. This can be formalized with the expression of the cost function for controller and estimator as:

$$\mathcal{F}_c^\infty = \int_0^T z_d^2 - \gamma^2 w_d^2 \mathrm{d}t, \tag{4.59}$$

and

$$\mathcal{F}_e^\infty = \int_0^T E\left[e^* e\right] - \gamma^2 w_d^2 \mathrm{d}t. \tag{4.60}$$

Note that the estimator state equation is the same of Eq. (4.53).

Re	γ	GM^+	GM^-	PM	ρ_∞^{im}	ρ_∞^{io}	Φ_2^{mg}	Φ_2^{ug}	Φ_∞^{mg}	Φ_∞^{ug}	Φ_2^{mw}	Φ_2^{uw}	Φ_∞^{mw}	Φ_∞^{uw}
5500	4.37	1.79	-2.26	13.2	0.23	0.24	15.3	13.2	4.36	4.13	4382	15.3	3928	4.36
6500	5.13	1.55	-1.88	11.2	0.20	0.54	11.9	2.09	5.12	1.85	5373	11.9	11093	5.12
7500	5.75	1.39	-1.66	10.0	0.17	0.97	13.2	2.60	5.73	1.03	7164	13.2	30184	5.73
8000	6.03	1.34	-1.58	9.56	0.17	0.84	14.0	3.17	5.99	1.19	6683	14.0	15851	5.99

Table 4.4: Robustness analysis results at different Reynolds numbers for a $\mathcal{H}_\infty$ controller with input-multiplicative disturbance. Gain margins are in dB and phase margin is in degrees.

The set of Riccati equations to be solved are then:

$$\mathrm{A}^*\mathcal{X} + \mathcal{X}\mathrm{A} - \mathcal{X}\left(\mathrm{B}_2\mathrm{B}_2^* - \frac{1}{\gamma^2}\mathrm{B}_2\mathrm{B}_2^*\right)\mathcal{X} = 0, \tag{4.61}$$

for the controller, with the control gain matrix $\mathrm{K} = -\mathrm{B}_2^*\mathcal{X}$, and:

$$\mathrm{A}\mathcal{Y} + \mathcal{Y}\mathrm{A}^* - \mathcal{Y}\mathrm{C}_2^*\mathrm{C}_2\mathcal{Y} + \mathrm{B}_2\mathrm{B}_2^* = 0, \tag{4.62}$$

for the estimator, with the Kalman gain matrix defined as $\mathrm{L} = -\mathcal{Y}\mathrm{C}_2^*$. The two equations have to be solved in the limit imposed by the condition of the spectral radius of the scalar product $\mathcal{X}\mathcal{Y}$, as for the standard $\mathcal{H}_\infty$ control proposed by Doyle et al. (1989). This condition is even more important here than in the classic robust control. In fact, looking at the above equations we can remark how the estimator design does not directly depend to γ unless for this condition, that has to be satisfied.

Results

Once the loop is closed we can perform the robustness and performance analysis. In Tab. 4.4 are summarized results for the input-multiplicative perturbation case. In this case, the most immediate result is an increasing in robustness, for stability margins and unstructured uncertainty related to the input-multiplicative perturbation model, paid with an increased cost in performances and a poor robustness to disturbances in series with the closed-loop system. This result highlights the importance of directly targeting robustness through a disturbance model. In fact, since this technique is built on a model that rejects input-multiplicative perturbations, any other type of disturbances is penalized. The cost payed is not only in terms of performances, but also in robustness to different perturbations.

In Fig. 4.18(a), the stability threshold presents a region of instability at low frequencies, a large band where the bound of stability oscillates around a minimum and a region that is eventually more stable at higher frequencies. This behavior is explained by observing the closed-loop transfer function in Fig. 4.18(b). The controller based on the maximization of the admissible input-multiplicative perturbation results on the closed-

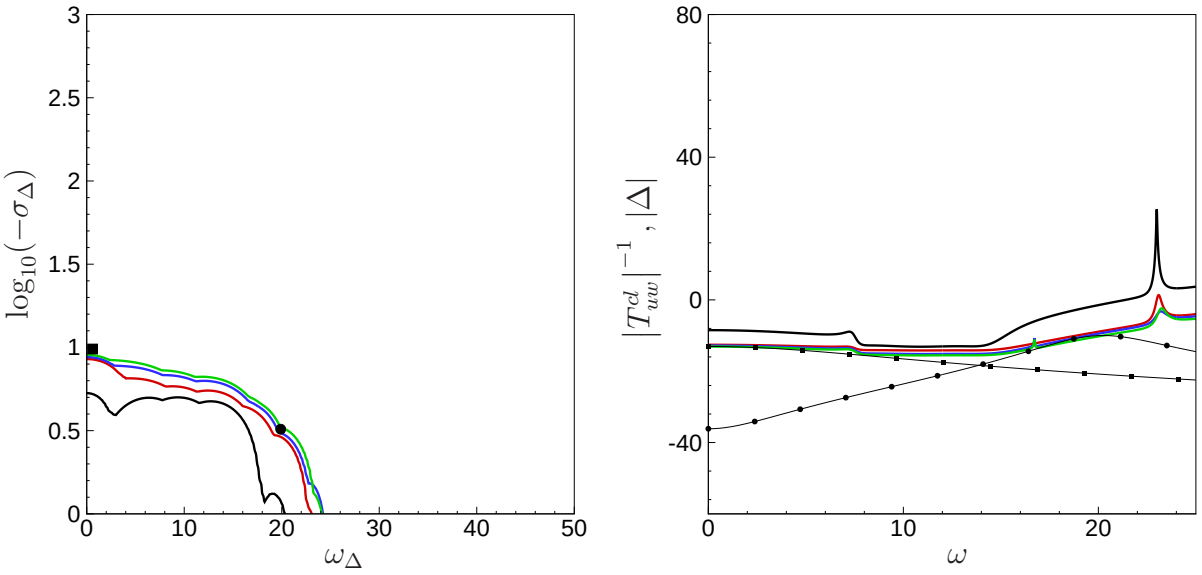

(a) (b)

Figure 4.18: (a) Stability threshold for an input-multiplicative perturbation on closed-loop systems with an input-multiplicative $\mathcal{H}_\infty$ compensator at different Reynolds numbers; (b) amplitude, expressed in dB, of the inverse closed-loop transfer function. For both figures, black line corresponds to $Re = 5500$ case, red line $Re = 6500$, blue line $Re = 7500$ and green line $Re = 8000$. Lines with squares and circles in (b) represent $|\Delta|$ and are obtained with the fixed values of σ_Δ and ω_Δ represented by a square and a circle in (a).

loop transfer function as a bandpass filter, with a band as large as possible. This result, compared with the LTR case, shows how the robust control is better for a wide range of frequencies around the natural frequency of the system, while it does not accept perturbations at lower or higher frequencies. This result is explained by considering that if we use the ∞-norm to design the controller, we only act on the maximum value of the admissible disturbance, that is actually higher than any other controller.

Summary

A controller that deals with input-multiplicative perturbations has been designed. This kind of disturbance is really common in engineering applications. In this study, a compensator has been designed by including the rejection to this perturbation in the definition of the objective functional. Through the small gain theorem the last sentence means that robustness to these perturbations is directly included in the definition of the objective functional. The analysis of robustness results has shown that this novel approach of compensator design provides a controller that is stable to input-multiplicative perturbations in a wide range of frequency.

Re	γ	GM^+	GM^-	PM	ρ_∞^{im}	ρ_∞^{io}	Φ_2^{mg}	Φ_2^{ug}	Φ_∞^{mg}	Φ_∞^{ug}	Φ_2^{mw}	Φ_2^{uw}	Φ_∞^{mw}	Φ_∞^{uw}
5500	0.016	1.92	-1.54	11.1	0.16	67.4	7.91	0.022	6.14	0.015	3864	7.91	4611	6.14
6500	0.016	0.91	-0.89	2.36	0.04	63.6	12.7	0.032	24.8	0.016	15175	12.7	81259	24.8
7500	0.032	0.31	-0.55	2.31	0.03	44.8	10.2	0.025	27.3	0.022	24173	10.2	187310	27.3
8000	0.029	0.70	-1.02	4.85	0.08	44.6	9.95	0.026	12.0	0.022	8876	9.95	42298	12.0

Table 4.5: Robustness analysis results at different Reynolds numbers for a $\mathcal{H}_\infty$ controller with input-to-output disturbance. Gain margins are in dB and phase margin is in degrees.

4.6.2 Input-to-output perturbation

The second case studied is an input-to-output perturbation model. This model represents a stable disturbance in parallel with the system. Even though is less common than the input-multiplicative uncertainty, this model is useful in this study to better understand the robust control design technique and how the target of design is robustness to a specific perturbation. With respect to the previous case, we consider the problem defined in Eq. (4.36) and represented in Fig. 4.12(b).

Framework

The cost function for the controller and the estimator are the same of the previous case, defined in Eq. (4.59) and (4.60). Here the $\mathcal{H}_\infty$ parameter γ acts on compensator design only through the condition on the spectral radius, as the Riccati equations are decoupled, as shown below.

$$\mathrm{A}^*\mathcal{X} + \mathcal{X}\mathrm{A} - \mathcal{X}\mathrm{B}_2\mathrm{B}_2^*\mathcal{X} + \mathrm{C}_2^*\mathrm{C}_2 = 0. \tag{4.63}$$

$$\mathrm{A}\mathcal{Y} + \mathcal{Y}\mathrm{A}^* - \mathcal{Y}\mathrm{C}_2^*\mathrm{C}_2\mathcal{Y} + \mathrm{B}_2\mathrm{B}_2^* = 0. \tag{4.64}$$

As usual, the control and estimator gain matrix are $\mathrm{K} = -\mathrm{B}_2^*\mathcal{X}$ and $\mathrm{L} = -\mathcal{Y}\mathrm{C}_2^*$, while the compensator matrix A_∞ is:

$$\mathrm{A}_\infty = \mathrm{A} + \mathrm{B}_2\mathrm{K} + \mathrm{Z}_\infty\mathrm{L}\mathrm{C}_2. \tag{4.65}$$

Results

In Tab. 4.5 results are summarized. With respect to the input-multiplicative model, this controller presents poor values of robustness except those corresponding to disturbances in parallel with the closed-loop system. More generally, even performances are more costly than the previous case and this cost is payed only to give to the closed-loop system a great robustness only to an input-to-output perturbation.

This behavior is more evident in Fig. 4.19. The region of instability is widely bigger because of the presence of the negative peak at $\omega \sim 17 rad/s$, since the method based on the SGT focused only on reduction of the bound of the corresponding modeled perturbation. In this case, the compensator is optimal to sustain disturbances in parallel with

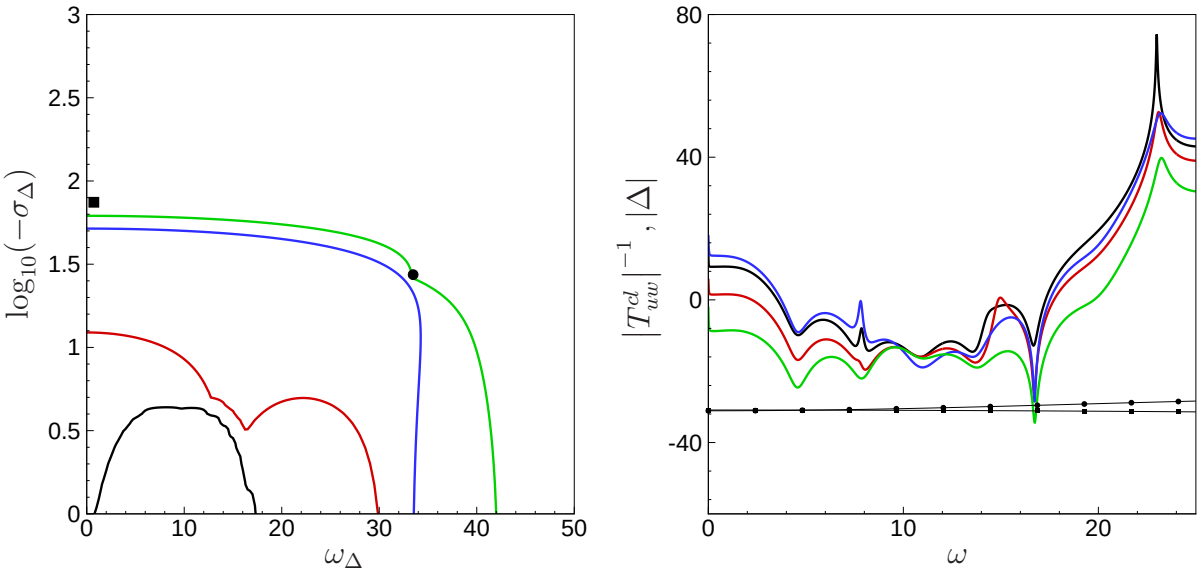

(a) (b)

Figure 4.19: (a) Stability threshold for a input-multiplicative perturbation on closed-loop systems with an input-to-output $\mathcal{H}_\infty$ compensator at different Reynolds numbers; (b) amplitude, expressed in dB, of the inverse closed-loop transfer function. For both figures, black line corresponds to $Re = 5500$ case, red line $Re = 6500$, blue line $Re = 7500$ and green line $Re = 8000$. Lines with squares and circles in (b) represent $|\Delta|$ and are obtained with the fixed values of σ_Δ and ω_Δ represented by a square and a circle in (a).

closed-loop system, but is not robust to other type of stable perturbations.

Summary

A different type of perturbation model has been considered in the definition of the design objective functional. The input-to-output model represents a disturbance in parallel with the closed-loop system. This model has been used to provide a controller that rejects this kind of perturbation. Even though this compensator shows good robustness to input-to-output perturbations, this case has been considered to show that the choice of disturbance rejection considered in the compensator design excludes robustness to other types of perturbations. In fact, the controller provided in this section presents poor robustness properties to input-multiplicative perturbations.

4.7 Unstable perturbations

The design methods analyzed in this study have been compared on their property of robustness to stable perturbations connected to closed-loop system through an input-multiplicative model. In particular, we designed a robust $\mathcal{H}_\infty$ controller that directly

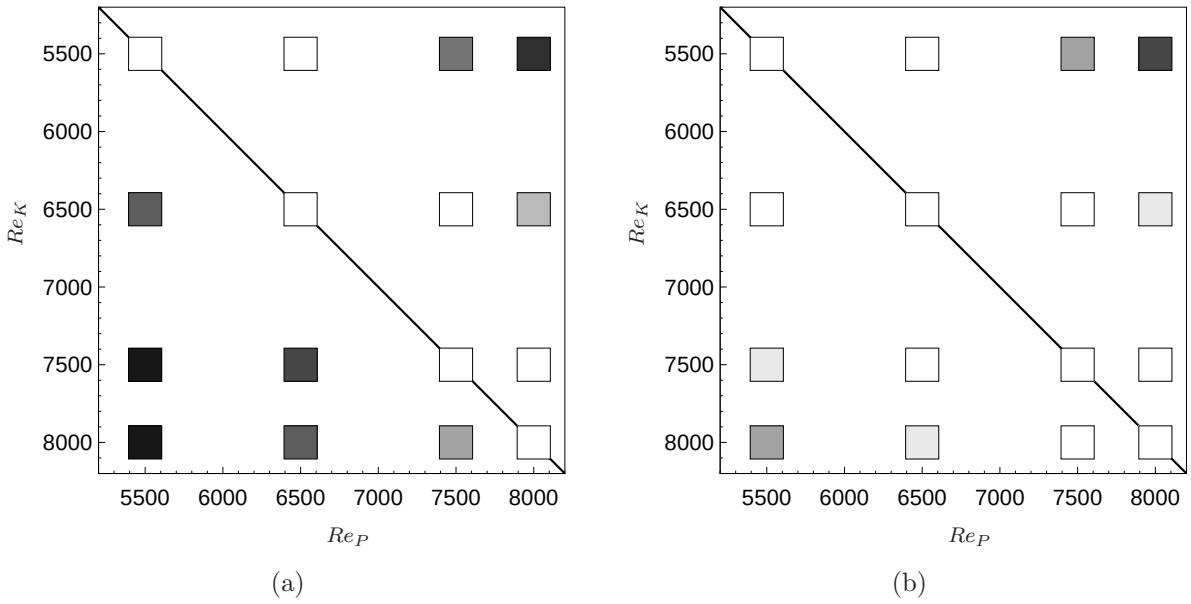

Figure 4.20: Stability behavior of $\mathcal{H}_2$ controllers, LQG/SGL (a) and LQG/LTR (b) at different Reynolds number. White squares represent maximum closed-loop poles with negative real parts (stable cases). Squares in gray scale represent maximum closed-loop poles with positive real parts (unstable). Instability intensity is represented through the color map from light gray (weak instability) to black (strong instability). Black solid line is the design locus, stable by definition since the plant $P(s)$ and the compensator $K(s)$ are obtained at the same Reynolds number (Re_P and Re_K respectively).

targets robustness to this type of uncertainty. With an iterative process the smallest γ that provides the most robust compensator in the sense of the unstructured disturbance model used has been found. This means that in the input-multiplicative model the smallest γ represents the bound for this kind of stable disturbance that guarantees to a closed-loop system to remain stable. We found out that the designed input-multiplicative compensator works well in a range of frequencies where a stable filter is applied as perturbation.

In flow control a frequent perturbation could be represented by a change of conditions, in particular a change in Reynolds number. This disturbance is evidently unstable, if considered as in input-multiplicative perturbation, and the SGT is violated. Nevertheless, some considerations on robust control could be done. In order to analyze the behavior of the studied compensator to this type of perturbation, we compare the stability analysis conducted on the SGL and the LTR and represented in Fig. 4.20(a) and 4.20(b). We can observe the improvement in robustness by using the LTR instead of the SGL. This result means that after a change in conditions, the LTR framework is more robust farther from the design point than the SGL. The white region, in fact, represents the ensemble of conditions where the closed-loop system remains stable.

The same analysis can be done on the robust control obtained with the input-multiplicative perturbation. The stability analysis represented in Fig. 4.21(a) shows a less robust behav-

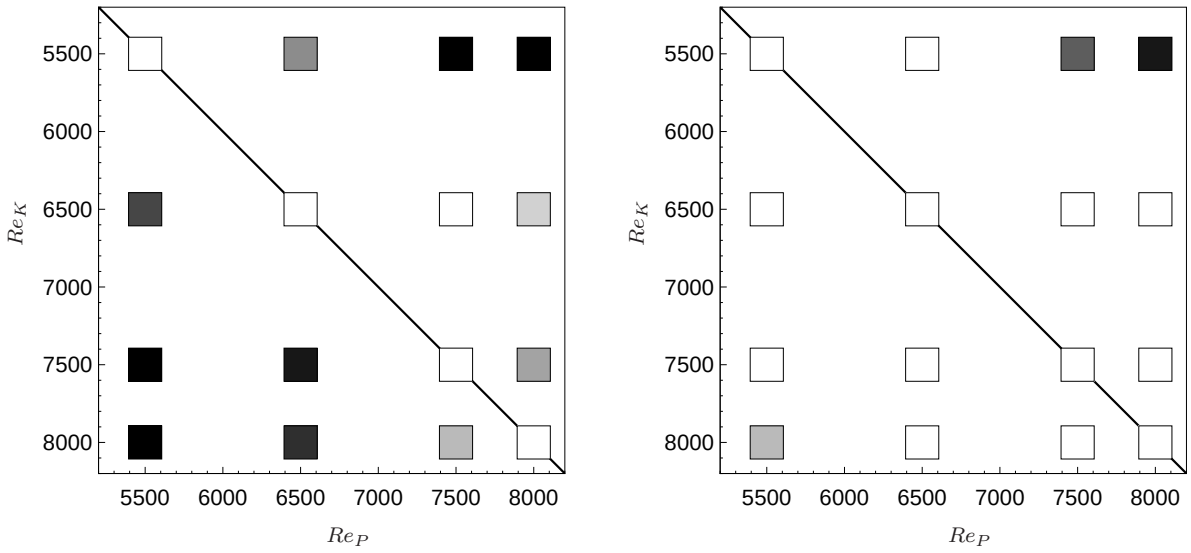

Figure 4.21: Stability behavior of $\mathcal{H}_\infty$ controllers, with the input-multiplicative model for the lowest γ (a) and for an "optimal" γ (b) at different Reynolds number. White squares represent maximum closed-loop poles with negative real parts (stable cases). Squares in gray scale represent maximum closed-loop poles with positive real parts (unstable). Instability intensity is represented through the color map from light gray (weak instability) to black (strong instability). Black solid line is the design locus, stable by definition since the plant $P(s)$ and the compensator $K(s)$ are obtained at the same Reynolds number (Re_P and Re_K respectively).

ior with respect to the LQG/LTR framework and, more surprisingly, also to the LQG in SGL hypothesis. This result does not confute robustness properties found in the previous section, since the model has been set up under the hypothesis of stable perturbations. However, robustness properties under unstable disturbances represent an interesting field of study.

The principle of the worst-case scenario, applied to the $\mathcal{H}_\infty$ control, led to an iterative procedure with the aim of finding the smallest value of γ with detriment to performances. We then tried to relax this value for the input-multiplicative case and observe the behavior of the resulting compensator under unstable perturbations. The obtained controller has properties summarized in Tab. 4.4.

The stability analysis has been conducted on the obtained compensator. The comparison between Fig. 4.21(a) and 4.21(b) shows the benefit of increasing γ in order to improve stability, suggesting a range of effectiveness. The main difference between the model used to design the compensator and the perturbation related to the different Reynolds is that the first is a stable perturbation of the closed-loop system, while the second is a perturbation acting on the plant and this perturbation is unstable. Since the SGT is valid for stable systems, the condition of application of the theorem is then no more valid and this

Re	γ	GM^+	GM^-	PM	ρ_∞^{im}	ρ_∞^{io}	Φ_2^{mg}	Φ_2^{ug}	Φ_∞^{mg}	Φ_∞^{ug}	Φ_2^{mw}	Φ_2^{uw}	Φ_∞^{mw}	Φ_∞^{uw}
5500	4.57	1.75	-2.16	12.7	0.22	1.19	8.55	0.86	4.53	0.84	3627	8.55	3623	4.53
6500	5.62	1.50	-1.75	10.6	0.18	1.85	8.59	0.84	5.47	0.54	3617	8.59	4249	5.47
7500	6.92	1.32	-1.46	9.07	0.16	4.34	9.00	0.67	6.45	0.23	3720	9.00	5370	6.45
8000	7.08	1.27	-1.41	8.74	0.15	2.08	9.57	0.90	6.65	0.48	3942	9.57	2923	6.65

Table 4.6: Robustness analysis results at different Reynolds numbers for a $\mathcal{H}_\infty$ controller with input-multiplicative disturbance at "optimal" values of γ. Gain margins are in dB and phase margin is in degrees.

explains how we cannot afford the smallest γ.

Chapter 5

Conclusions

The main purpose of this study was to develop a closed-loop technique that could be used in real applications. To achieve this objective two strategies have been analyzed: in the first part of this thesis, a non-linear reduced-order model based on system identification from TR-PIV measurements has been studied; in the second part, robustness properties of linear closed-loop control have been improved by introducing a perturbation model in the control-design phase.

The experimental activity described in Chapter 2 has been necessary to qualify the cavity flow. The all set of measurements acquired gave access to a complete characterization of the flow in terms of pressure distribution, boundary layer and turbulence level. Unsteady measurements gave the frequency information corresponding to the characteristic oscillating behavior of the cavity flow. The fundamental frequency of oscillation has been found about 125 Hz, after a modification of the cavity depth, in order to obtain a more manageable bandwidth for the actuator design.

Qualification results have been used to perform a TR-PIV campaign. The objective of this acquisition was not only to have access to mean features of the flow field, but to produce a full data set to be used in the system identification procedure. The high frequency sampling of 3 kHz gave full access to the oscillating-related structures as well as smaller fluctuating eddies. The quality of post-precessed images gave a good description of the detachment of vortex structures from the leading edge of the cavity through the shear layer until the impact onto the downstream wall.

As explained, the TR-PIV was necessary to obtain from it an identified non-linear reduced-order model, based on an energetic decomposition as POD modes. With this purpose, high-frequency related features have been filtered above 150 Hz in order to keep only dynamics related to the first oscillating harmonic. Fourier filter is not commonly applied to PIV images and results could not be compared with any precedent work. However, time filtering gave interesting results on how even through a non-linear process as the eigenvalue decomposition, some features are preserved (related to the main motion)

while others lose any physical meaning.

Time filtering eventually led to keep only the first two POD modes as basis for the reduced-order model. Model reduction has been a central part of this study, because of the key role assumed in the system identification technique. The choice of considering only the first two modes, simplified the algorithm structure, allowing a deeper analysis on the others parameters, still conserving the non-linearity of the oscillating motion. In the perspective of closed-loop control, time filtering gave good results and can be considered as a valid and innovative technique to be applied to PIV measurements and, more generally, to experimental data.

The system identification technique has been studied in Chapter 3. Non-linear dynamics have been the most challenging issues to deal with, since every other dynamic related to smaller eddies and high-frequency noise have been filtered. In order to reproduce the non-linear behavior the algorithm structure considered was the same as that obtained from a Galerkin projection of Navier-Stokes equations onto a POD basis. A third-order term has been added accordingly to the Stuart-Landau amplitude equation.

The coefficients of the algorithm have been determined through a least-square method over a learning data-set and then validate on a different set of data. Some parameters have been considered in this process, observing their influence in both phases. The experience has shown that the number of modes considered plays against the known previous time steps. On the other hand, even with a small amount of time trajectories, a long known time history can produce ill-posed problems.

In general, this technique has shown poor robustness to design parameters, since even a small change in those can produce instabilities in model prediction. Furthermore, even if the frequency content is well reproduced, long-time prediction fails in following the non-linear behavior. Although this method is promising and has previously shown good results on linear or linearized dynamics, it has not be considered in this study as an affordable choice to closed-loop control.

A different approach to achieve the purpose of a control suitable for experimental cases has been discussed in Chapter 4. A linearized cavity control problem already studied by Barbagallo et al. (2009) has been the subject of a robustness analysis. Different control design strategies have been compared on performances and robustness parameters. From a traditional LQG regulator we analyzed the increment in robustness obtained with a LTR and the direct application of the robust control theory introduced by Doyle et al. (1989), showing poor results.

A new approach has been proposed involving models of stable unstructured uncertainties, directly included in control design. The minimization of the cost function, in terms of $\mathcal{H}_\infty$-norm, carries the principle of bounded perturbation expressed in the small gain theorem. A new interpretation of such theorem has been given, since for the first time

frequency contribution has been considered.

Including a bounded perturbation model in control design has led to important results, in terms of robustness increment, especially with the input-multiplicative perturbation model, even though this increment is obtained to the detriment of a cost in performances.

5.1 Perspectives

The presented study has analyzed a detailed qualification of the experimental flow from which an identified non-linear model has been deduced as well as a numerical study on performance and robustness properties of different control design techniques. However, future works must be considered to continue a promising research field.

Installation of an actuator on the S19 facility

The experimental activity has been carried out with the purpose of performing real-time closed-loop control. This purpose can be achieved with a flap installed at the leading edge of the cavity, moving in given bandwidth of 0-150 Hz. A preliminary study has been conducted, leading to a design of an actuator moved by a motor of maximum couple 1.5 Nm. The flap is capable of perturbing the flow on a range of $\pm 4mm$, in order to act on velocity fluctuations. The study has been carried out at the ONERA Department of Fundamental and Experimental Aerodynamics.

Model reduction from experimental measurements

Time filtering is to be considering an innovation on PIV post-processing to flow control. The purpose of using TR-PIV acquisitions is not only to deduce a reduced-order model, but also to use snapshots as sensor information in the feedback procedure. With the aim of avoiding high frequency noise, time-filtering has revealed promising results, but a Fourier filter is not applicable to real-time case, since the FFT must be applied to a known series of snapshots. Preliminary studies on a Cauchy filter applied to raw snapshots have shown the only disadvantage of introducing a delay that can be easily modeled in a reduced-order model.

System identification technique has shown its weak points. However, this is a quite new field in flow control applications and many paths are still not explored or need some insight. In particular, we refer to neural networks that show great potential in statistical learning of non-linear dynamics (Dreyfus et al., 2011).

Model of unstable Reynolds perturbations

Results obtained on robustness are the greatest results achieved in this study. Even so, the two different models proposed only consider stable perturbations. In the last section of Chapter 4 some considerations about unstable perturbations as the change of Reynolds number have been considered. A possible solution to deal with these perturbations could be the introduction of a structured uncertainty in the control design that permits to model

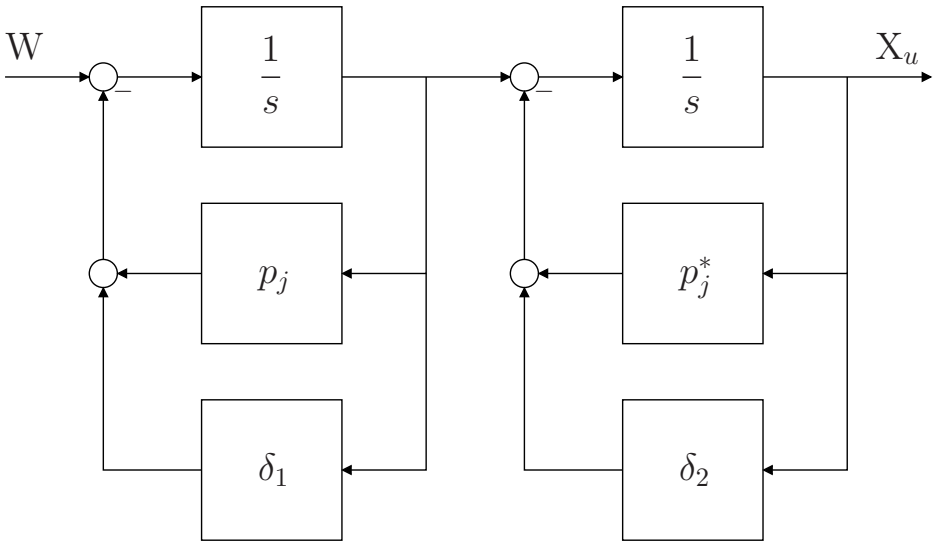

Figure 5.1: An example of modeling parameter uncertainties as feedback perturbations δ_1 and δ_2.

not only the stable part, but also unstable modes. This model is described by Burl (1998) and it considers the plant as a series of poles that can be separately perturbed by different δ, as in the scheme in Fig. 5.1. These blocks are then included in the iterative process that finds the bound for the maximum structured singular value of the resulting perturbed closed-loop system. This should be considered as a future step to improve compensator robustness in more real cases.

Bibliography

Ahuja, S. and Rowley, C. W. (2008). Low-dimensional models for feedback stabilization of unstable steady states. *AIAA Paper*, 553:2008.

Ahuja, S. and Rowley, C. W. (2010). Feedback control of unstable steady states of flow past a flat plate using reduced-order estimators. *J. Fluid Mech*, 645:447–478.

Aider, J.-L., Beaudoin, J.-F., and Wesfreid, J. E. (2010). Drag and lift reduction of a 3d bluff-body using active vortex generators. *Experiments in fluids*, 48(5):771–789.

Åkervik, E., Ehrenstein, U., Gallaire, F., and Henningson, D. S. (2008). Global two-dimensional stability measures of the flat plate boundary-layer flow. *European Journal of Mechanics-B/Fluids*, 27(5):501–513.

Alizard, F. and Robinet, J.-C. (2011). Modeling of optimal perturbations in flat plate boundary layer using global modes: benefits and limits. *Theoretical and Computational Fluid Dynamics*, 25(1-4):147–165.

Amestoy, P. R., Duff, I. S., L'Excellent, J.-Y., and Koster, J. (2001). A fully asynchronous multifrontal solver using distributed dynamic scheduling. *SIAM J. Matrix Anal. Appl.*, 23(1):15.

Bagheri, S., Brandt, L., and Henningson, D. S. (2009). Input–output analysis, model reduction and control of the flat-plate boundary layer. *Journal of Fluid Mechanics*, 620(1):263–298.

Barbagallo, A., Sipp, D., and Schmid, P. (2009). Closed-loop control of an open cavity flow using reduced order models. *J. Fluid Mech.*, 641:1.

Baron, A., Quadrio, M., and Vigevano, L. (1993). On the boundary layer/riblets interaction mechanisms and the prediction of turbulent drag reduction. *International journal of heat and fluid flow*, 14(4):324–332.

Bergmann, M., Bruneau, C.-H., and Iollo, A. (2009). Enablers for robust pod models. *Journal of Computational Physics*, 228(2):516–538.

Bergmann, M. and Cordier, L. (2008). Optimal control of the cylinder wake in the laminar regime by trust-region methods and pod reduced-order models. *Journal of Computational Physics*, 227(16):7813–7840.

Bewley, T. R. (2001). Flow control: new challenges for a new renaissance. *Progress in Aerospace sciences*, 37(1):21–58.

Bewley, T. R. and Liu, S. (1998). Optimal and robust control and estimation of linear paths to transition. *J. Fluid Mech.*, 365(1):305.

Burl, J. B. (1998). *Linear Optimal Control: H (2) and H (Infinity) Methods*. Addison-Wesley Longman Publishing Co., Inc.

Cattafesta, L., Williams, D., Rowley, C., and Alvi, F. (2003). Review of active control of flow-induced cavity resonance. *AIAA paper*, 3567:2003.

Cattafesta, L. N. and Sheplak, M. (2011). Actuators for active flow control. *Annual Review of Fluid Mechanics*, 43:247–272.

Champagnat, F., Plyer, A., Le Besnerais, G., Leclaire, B., Davoust, S., and Le Sant, Y. (2011). Fast and accurate piv computation using highly parallel iterative correlation maximization. *Experiments in fluids*, 50(4):1169–1182.

Chiuso, A. and Picci, G. (2005). Consistency analysis of some closed-loop subspace identification methods. *Automatica*, 41(3):377–391.

Colonius, T. (2001). An overview of simulation, modeling, and active control of flow/acoustic resonance in open cavities. *AIAA paper*, 76:2001.

Cordier, L., Bergmann, M., et al. (2008). Proper orthogonal decomposition: an overview. *Lecture series 2002-04, 2003-03 and 2008-01 on post-processing of experimental and numerical data, Von Karman Institute for Fluid Dynamics, 2008.*

Cortelezzi, L. and Speyer, J. (1998). Robust reduced-order controller of laminar boundary layer transitions. *Physical review E*, 58(2):1906.

Debiasi, M. and Samimy, M. (2004). Logic-based active control of subsonic cavity flow resonance. *AIAA journal*, 42(9):1901–1909.

Di Stefano, J., Stubberud, A., and Williams, I. (1990). Feedback and control systems.

Doyle, J. C., Glover, K., Khargonekar, P. P., and Francis, B. A. (1989). State-space solutions to standard $\mathcal{H}_2$ and $\mathcal{H}_\infty$ control problems. *IEEE Trans. Automat. Control*, 34(8):831.

Dreyfus, G., Martinez, J.-M., Samuelides, M., Gordon, M. B., Badran, F., and Thiria, S. (2011). *Apprentissage statistique: Réseaux de neurones-Cartes topologiques-Machines à vecteurs supports*. Editions Eyrolles.

East, L. (1966). Aerodynamically induced resonance in rectangular cavities. *J. Sound Vib.*, 3:277–287.

Ehrenstein, U. and Gallaire, F. (2005). On two-dimensional temporal modes in spatially evolving open flows: the flat-plate boundary layer. *Journal of Fluid Mechanics*, 536:209–218.

Ehrenstein, U., Passaggia, P.-Y., and Gallaire, F. (2012). Model reduction and control of a separating boundary-layer flow. In *Progress in Flight Physics*, volume 3, pages 471–482. EDP Sciences.

El-Samni, O., Chun, H., and Yoon, H. (2007). Drag reduction of turbulent flow over thin rectangular riblets. *International Journal of Engineering Science*, 45(2):436–454.

Godard, G. and Stanislas, M. (2006). Control of a decelerating boundary layer. part 1: Optimization of passive vortex generators. *Aerospace Science and Technology*, 10(3):181–191.

Henning, L. and King, R. (2007). Robust multivariable closed-loop control of a turbulent backward-facing step flow. *Journal of aircraft*, 44(1):201–208.

Hervé, A., Sipp, D., Schmid, P. J., and Samuelides, M. (2012). A physics-based approach to flow control using system identification. *Journal of Fluid Mechanics*, 702:26–58.

Huang, S.-C. and Kim, J. (2008). Control and system identification of a separated flow. *Physics of Fluids (1994-present)*, 20(10):101509.

Huerre, P. and Rossi, M. (1998). Hydrodynamic instabilities in open flows. *COLLECTION ALEA SACLAY MONOGRAPHS AND TEXTS IN STATISTICAL PHYSICS*, pages 81–294.

Ilak, M. and Rowley, C. (2006). Reduced-order modeling of channel flow using traveling pod and balanced pod. In *Proceedings of the 3rd AIAA Flow Control Conference*, volume 2, pages 1–11.

Ilak, M. and Rowley, C. W. (2008). Modeling of transitional channel flow using balanced proper orthogonal decomposition. *Physics of Fluids*, 20:034103.

Illy, H., Jacquin, L., and Geffroy, P. (2008). Observations on the passive control of flow oscillations over a cavity in a transonic regime by means of a spanwise cylinder. In *4th AIAA Flow Control Conference*, volume 3774, page 2008.

Juillet, F., Schmid, P. J., and Huerre, P. (2013). Control of amplifier flows using subspace identification techniques. *Journal of Fluid Mechanics*, 725:522–565.

Kalman, R. E. (1960). A new approach to linear filtering and prediction problems. *Journal of basic Engineering*, 82(1):35–45.

Kasagi, N., Hasegawa, Y., and Fukagata, K. (2009). Toward cost-effective control of wall turbulence for skin friction drag reduction. *Advances in turbulence XII*, pages 189–200.

Kegerise, M. A., Cabell, R. H., and Cattafesta, L. N. (2004). Real-time adaptive control of flow-induced cavity tones. *AIAA Paper*, 572:2004.

Kerstens, W., Pfeiffer, J., Williams, D., King, R., and Colonius, T. (2011). Closed-loop control of lift for longitudinal gust suppression at low reynolds numbers. *AIAA journal*, 49(8):1721–1728.

Kim, J. and Bewley, T. R. (2007). A linear systems approach to flow control. *Annu. Rev. Fluid Mech.*, 39:383.

Lall, S., Marsden, J. E., and Glavaški, S. (2002). A subspace approach to balanced truncation for model reduction of nonlinear control systems. *International journal of robust and nonlinear control*, 12(6):519–535.

Lauga, E. and Bewley, T. R. (2004). Performance of a linear robust control strategy on a nonlinear model of spatially developing flows. *J. Fluid Mech.*, 512:343.

Ljung, L. (1999). *System Identification: Theory for the User, PTR Prentice Hall Information and System Sciences Series*. Prentice Hall, New Jersey,.

Lumley, J. L. (1967). The structure of inhomogeneous turbulent flows. *Atmospheric turbulence and radio wave propagation*, pages 166–178.

McGrath, S. and Shaw, L. (1996). Active control of shallow cavity acoustic resonance. *AIAA paper*, 1949:1996.

Moore, B. (1981). Principal component analysis in linear systems: Controllability, observability, and model reduction. *Automatic Control, IEEE Transactions on*, 26(1):17–32.

Moore, J. B., Gangsaas, D., and Blight, J. D. (1981). Performance and robustness trades in lqg regulator design. In *Decision and Control including the Symposium on Adaptive Processes, 1981 20th IEEE Conference on*, volume 20, pages 1191–1200. IEEE.

Noack, B. R., Afanasiev, K., Morzynski, M., Tadmor, G., and Thiele, F. (2003). A hierarchy of low-dimensional models for the transient and post-transient cylinder wake. *Journal of Fluid Mechanics*, 497:335–363.

Pujals, G., Depardon, S., and Cossu, C. (2010). Drag reduction of a 3d bluff body using coherent streamwise streaks. *Experiments in fluids*, 49(5):1085–1094.

Qin, S. J. (2006). An overview of subspace identification. *Computers & chemical engineering*, 30(10):1502–1513.

Qin, S. J. and Ljung, L. (2003). Closed-loop subspace identification with innovation estimation. In *Proceedings of the 13th IFAC SYSID Symposium*, pages 887–892.

Quadrio, M. and Ricco, P. (2004). Critical assessment of turbulent drag reduction through spanwise wall oscillations. *Journal of Fluid Mechanics*, 521:251–271.

Rossiter, J. (1964). Wind tunnel experiments on the flow over rectangular cavities at subsonic and transonic speeds. Technical report, Royal Aircraft Establishment, TR-64037.

Rowley, C. W. (2005). Model reduction for fluids, using balanced proper orthogonal decomposition. *Int. J. Bifurcation and Chaos*, 15(03):997.

Rowley, C. W. and Batten, B. A. (2008). Dynamic and closed-loop control.

Rowley, C. W., Colonius, T., and Murray, R. M. (2004). Model reduction for compressible flows using pod and galerkin projection. *Physica D: Nonlinear Phenomena*, 189(1):115–129.

Samimy, M., Debiasi, M., Caraballo, E., Serrani, A., Yuan, X., Little, J., and Myatt, J. (2007). Feedback control of subsonic cavity flows using reduced-order models. *Journal of Fluid Mechanics*, 579:315–346.

Scarano, F. and Sciacchitano, A. (2011). Robust elimination of light reflections in piv. In *9th International Symposium on Particle Image Velocimetry*.

Scherpen, J. M. (1993). Balancing for nonlinear systems. *Systems & Control Letters*, 21(2):143–153.

Shaw, L. and Northcraft, S. (1999). Closed loop active control for cavity acoustics. *AIAA*.

Sipp, D., Barbagallo, A., Marquet, O., and Meliga, P. (2010). Dynamics and control of global instabilities in open-flows: a linearized approach. *Applied Mechanics Reviews*, 63(3):030801.

Sipp, D. and Lebedev, A. (2007). Global stability of base and mean flows: a general approach and its applications to cylinder and open cavity flows. *J. Fluid Mech.*, 593(1):333.

Sirovich, L. (1987). Turbulence and the dynamics of coherent structures. i-coherent structures. ii-symmetries and transformations. iii-dynamics and scaling. *Quarterly of applied mathematics*, 45:561–571.

Tian, Y., Song, Q., and Cattafesta, L. (2006). Adaptive feedback control of flow separation. *AIAA paper*, 3016(2006).

Ukeiley, L., Sheehan, M., Coiffet, F., Alvi, F., Arunajatesan, S., and Jansen, B. (2007). Control of pressure loads in complex cavity configurations. In *45th AIAA Aerospace Sciences Meeting and Exhibit, Reno, NV*.

Walsh, M. J. (1983). Riblets as a viscous drag reduction technique. *AIAA journal*, 21(4):485–486.

Yamouni, S., Mettot, C., Sipp, D., and Jacquin, L. (2013). Passive control of cavity flows. *system*, 5:10.

Zames, G. (1966). On the input-output stability of time-varying nonlinear feedback systems part one: Conditions derived using concepts of loop gain, conicity, and positivity. *Automatic Control, IEEE Transactions on*, 11(2):228–238.

Zhou, K., Doyle, J. C., Glover, K., et al. (1996). *Robust and optimal control*, volume 40. Prentice Hall New Jersey.

Zhou, K., Salomon, G., and Wu, E. (1999). Balanced realization and model reduction for unstable systems. *International Journal of Robust and Nonlinear Control*, 9(3):183–198.

Zhuang, N., Alvi, F. S., Alkislar, M. B., and Shih, C. (2006). Supersonic cavity flows and their control. *AIAA journal*, 44(9):2118–2128.